Karlsruhe Institute of Technology

Université Grenoble Alpes

Université franco-allemande Deutsch-Französische Hochschule

ETP-KA/2020-7

Study of the Fermi GeV excess with deconvolved data

Master Thesis of

Joanna Berteaud

At the Department of Physics
Institut für Experimentelle Teilchenphysik (ETP)

Reviewer:	Prof. Dr. Wim de Boer
Second reviewer:	Prof. Dr. Ulrich Husemann
Advisor:	Dr. Iris Gebauer

Karlsruhe, 04. March 2020

This thesis has been accepted by the first reviewer of the master thesis.

PLACE, DATE

.....

(**Prof. Dr. Wim de Boer**)

I declare that I have developed and written the enclosed thesis completely by myself, and have not used sources or means without declaration in the text.

PLACE, DATE

.....

(**Joanna Berteaud**)

Contents

1 Introduction

Back at the beginning of the twentieth century, cosmic rays were still undiscovered. At that time, some physicists had already noticed electric charges were repeatedly detected by electroscopes, no matter how well they were isolated. This phenomenon was thought to be caused by terrestrial radioactivity coming from the ground and it was therefore assumed that electroscopes should detect less and less charges if they are brought further and further from the ground. In order to test that hypothesis, Theodore Wulf went to the Eiffel Tower and measured the ionization in the atmosphere at the bottom and the top of it. His results were surprisingly not compatible with terrestrial radiations: more charges were detected at the top of the Eiffel Tower than expected. At ground level, he measured 6 ions cm^{-3} and more than 3 ions cm^{-3} at about 330 meters high. If the radiation was truly terrestrial, it should have halved after 80 meters. His results were not widely accepted but led Victor Hess to think that the ionization could in fact come from the sky. Hess was a young Austrian physicist who got his PhD in 1910 from the University of Graz. He got highly interested in atmospheric ionization while working with his tutor Franz Exner on atmospheric electricity. Between 1911 and 1912, many experiments were created by Hess and embedded in balloons for 5000 meters high flights. The physicist found that although radiations were at first decreasing with height, at some point they started increasing swiftly, largely exceeding the radiations at ground level. He concluded that *"a radiation of very high penetrating power enters our atmosphere from above"*. Hess performed his most famous experiment the day of a solar eclipse on April 17, 1912. As his electroscopes did not detect less charges than during his other flights where the Sun was not hidden by the Moon, he claimed that the radiation was not coming from the Sun but from the outer space itself. Thirteen years later, Robert Millikan, the physicist who first measured the elementary electric charge, confirmed this result and named the radiation "cosmic rays" and in 1936, Victor Hess earned the Nobel Prize for his discovery.

Domenico Pacini, an Italian physicist from the University of Bari, performed the same kind of experiments as Hess shortly before him. With electroscopes, he measured the ionization level at the surface of seas and lakes, where the impact of soil radioactivity is small. His results showed that another source of ionization than the ground should be present. He supposed that the air and the water radioactivity could also contribute to the ionization. In June 1911, Pacini placed his experiment three meters under water in an eight meter-deep water, three hundred meters away from the coast [1]. His ionization measurements were too high compared to theoretical predictions including only water,

air and soil radioactivity. He concluded that another source of ionization, not coming from the Earth, was present and affirmed that *"a sizable cause of ionization exists in the atmosphere, originating from penetrating radiation, independent of the action of radioactive substances in the soil"*. Unlike Hess, who was awarded for his discovery, Pacini remained in the shadows. Albert Gockel suffered the same fate. After getting his PhD in Heidelberg in 1885, he worked at the university of Freiburg in Switzerland as an assistant. He spent a lot of time working alone on his favorite subject, the ionization of air, with an extremely short budget. However, he measured the ion density of the air not only in Europe but also in North Africa and Turkey, and in various places such as caves, mountains, lakes and sees. Just like Hess, he also used balloon flights for his experiments. His first flight took place in December 1909 and was funded by the Swiss Aeroclub. His balloon, the *Gotthard*, reached 4500 meters and let Gockel notice that the ion density in the air was at first decreasing, and then increasing with altitude. Because of its limited budget and the circumstances of the flight, he was not sure of his results and his reports were probably not convincing. After two more flights in 1910 and 1911, he finally confirmed his results but this was not enough to bring him the same success as Hess.

After this discoveries, cosmic rays were of course highly studied for identification. Robert Millikan, who coined them, thought in the 20s that the ionization detected in the atmosphere was due to gamma ray photons produced in interstellar space interacting by Compton scattering to produce secondary electrons. However, in 1927 Jacob Clay discovered that cosmic rays were deflected by the geomagnetic field so they must be charged particles which photons are not. During the 30s and the 40s, Pierre Auger and Bruno Rossi discovered separately that outer space cosmic rays were mostly protons and while interacting in the Earth atmosphere, they were causing a cascade of secondary reactions creating a mostly protons, electrons and muons. Today, after more than a century of searches, physicists are still interested in cosmic rays. As they come from interstellar space, they help in the understanding of the galaxy. Sometimes, they undergo processes that create gamma rays which are used for indirect detection of cosmic rays. They are really convenient because they carry no charge so they are not deflected by any magnetic field and travel in straight line from their creation area to the Earth. But gamma rays are not only created by cosmic rays but also by point sources or hypothetically by dark matter. The existence of the latter is supported by many evidences and its detection is a real challenge and would help physicists in the understanding of the universe.

The Fermi Large Area Telescope is a gamma ray space observatory that was launched in June 2008. After 17 months of data collection, a paper titled *Possible evidence for dark matter annihilation in the inner Milky Way from the Fermi gamma ray space telescope* was published [2]. An excess in the diffuse gamma ray spectrum, compared to model predictions including photons created by cosmic rays through pion decay, inverse Compton scattering and Bremsstrahlung, with a shift of the maximum had been detected towards the galactic center. Since then, many groups started working on data from the Fermi telescope and many hypotheses appeared to explain this excess. One of them is the modification of the cosmic ray spectrum in molecular clouds. A depletion of low energetic cosmic ray protons in molecular clouds modifies the gamma ray spectrum produced by pion decay. Previous studies already found evidences supporting this hypothesis. However, they did not include the point spread function effect on the data: as they are observed through the Fermi Large Area Telescope, they undergo some modification on their spatial distribution. It was suspected recently that some of these modifications could create or increase the signal, so that not only physics effects in the galaxy, but also detector effects give rise to the signal. The main goal of this work is to correct the data for the point spread function and study the

remaining signal to see if the evidences for the hypothesis remain. In the second chapter, an overview of the theoretical knowledge required for the understanding of the thesis is provided. This chapter deals with the Milky Way, cosmic rays, gamma rays and the Fermi Large Area Telescope. The third chapter describes the methods used for the analysis in previous works and also in this one: the data selection, the data fitting procedure and also the main point of this thesis which is removing the point spread function effect from the data. Finally, the fourth chapter presents the results and conclusions of this work.

2 Overview

This chapter provides an overview over the knowledge required for the understanding of this thesis. First, information about the Milky Way, which is the galaxy studied in this work, and its components are provided. The next two parts deal respectively with cosmic rays and with gamma rays, the latter producing the data used in this work. Finally, the Fermi Large Area Telescope, that collects the data, is presented.

2.1 The Milky Way and its components

The Milky Way is a barred spiral galaxy whose gaseous disk has a radius of 15 kpc[1] and a scale height of about 250 pc, which makes it the second largest galaxy in the Local Group after the Andromeda galaxy. It has the shape of a disk and its bar extends into two major spiral arms. The Solar System lies approximately half way out from the galactic center in a minor arm. The galactic disk, where most of the stars lie, is surrounded by a halo with a spherical shape composed of older stars. The brightest part of the Milky Way is a cubic pc around its rotational center, also called the galactic center. It harbors about ten million stars and a supermassive black hole of 4.5 million solar masses. It is surrounded by a spherical 3 kpc bulge of old stars traveling outside the galactic plane. A small region rich in molecular gas, called the central molecular zone (CMZ[2]) is located between galactic longitude 1.7° and -0.7° and latitude $\pm 0.2^\circ$. A representation of the Milky way is given in figure 2.1.

In total, hundreds of billions of stars belong to the Milky Way. In the vicinity of the Sun, stars have a distance of about 2 pc. However, the space between them is not empty and is called the interstellar medium (ISM). It is composed of ionized, atomic and molecular gas of mostly hydrogen and helium, dust and cosmic rays. One interesting component of the ISM are molecular clouds (MCs). They form the densest component of the ISM, reaching 10^2 to 10^6 particles/cm^3 but also the coldest one, with temperatures between 10 and 20K. Their high density allows the formation of molecules such as H_2 or CO. Stars form exclusively in MCs. All the MCs in the Milky Way account for approximately 10^9

[1] The parsec (pc) is a unit of length used in astronomy. A parsec equals the distance at which one AU, which is about the distance between Earth and Sun, subtends an angle of one arcsecond, which is 1/3600th of a degree. 1 parsec also equals 3.26 light years or 3.09×10^6 meters.

[2] A glossary of all the abbreviation used in this work can be found in appendix A.

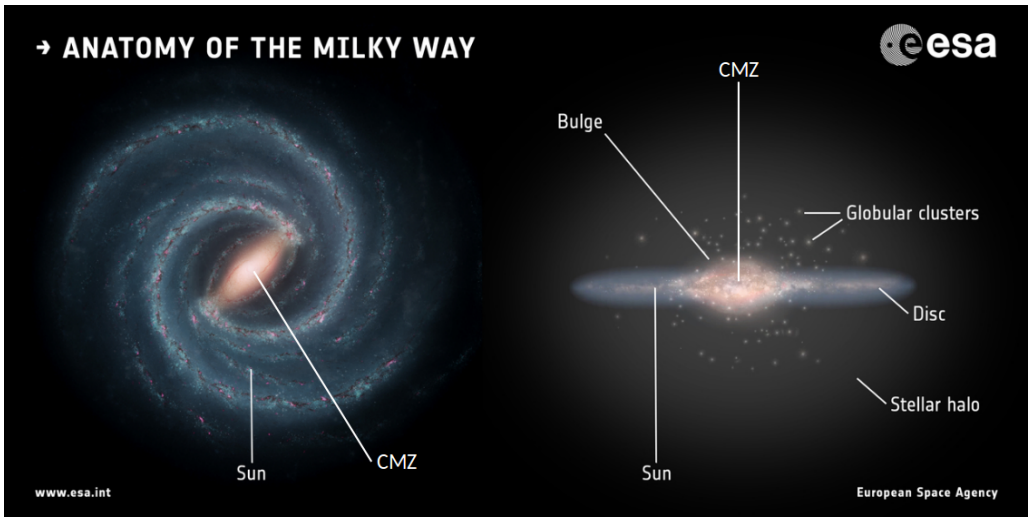

Figure 2.1: An artist's impression of the Milky Way. Adapted from [3].

solar masses which is about 40% of the total mass of the ISM but less than 1% of its volume. Another component of the galaxy is the interstellar radiation field (ISRF), which influences the physical state of the ISM, such as its thermal or chemical state. Its main contributors are:

- stars, which emit photons mostly in the infrared, visible and ultraviolet ranges. The energy density of the starlight is 1.1×10^{-12} erg cm^{-3};[3]
- dust grains, which emit infrared and far-infrared photons. The spectrum of this emission is nearly a blackbody spectrum at a temperature of 17 K. The energy density of this component is 5.0×10^{-13} erg cm^{-3};
- the cosmic microwave background (CMB), which is a blackbody radiation at a temperature of 2.73 K. Its energy density is 4.2×10^{-13} erg cm^{-3};
- ionized plasma, which has three main types of emissions: Bremsstrahlung or free-free emission, free-bound emission and bound-bound emission. Its total energy density adds up to an order of magnitude of $10^{-15} - 10^{-14}$ erg cm^{-3};
- hot plasma, produced by highly energetic events such as supernovae, cools down by emitting X-ray photons. The energy density of these thermal X ray is approximately 10^{-17} erg cm^{-3};
- relativistic electrons that interact with the ambient magnetic field, are then radially accelerated and emit synchrotron radiation, whith an energy density of 2.7×10^{-18} erg cm^{-3}.

Dark matter (DM) could also be a component of the galaxy. Its existence is hypothetical but many pieces of evidence tend to corroborate this hypothesis. For example, the observed rotation curve of many galaxies does not correspond to the one calculated from Kepler's laws: the first remains flat whereas the latter decreases as the distance from the galactic center increases. These galaxies rotate just like if there was more mass than what is optically seen. This conclusion can also be drawn from observations of the internal dynamics of galactic clusters or weak lensing effects. Together with cosmological observations, these evidences led physicists to assume that a form of matter which accounts for about 85% of all the matter in the universe is yet undetected. DM is thought to be non-baryonic and

[3]The erg is a unit of energy used in astrophysics. One erg equals 10^{-7} joules.

to interact with ordinary matter only through gravity or any other (potentially unknown) force weaker or as weak as the weak nuclear force. It is also its own antiparticle. The most commonly used model profiles for DM halos is the Navarro-Frenk-White (NFW) profile [4], in which the DM density ρ as a function of the radius r is:

$$\rho(r) = \frac{\rho_0}{\frac{r}{R}\left(1+\frac{r}{R}\right)^2} \tag{2.1}$$

where ρ_0 and R are constants specific to each galaxy. This profile shows a spherical morphology around the galactic center. For the Milky Way, $\rho_0 = 4 \times 10^7$ $M_\odot/\text{kpc}^3$ and $R = 10$ kpc [5].

2.2 Charged cosmic rays

2.2.1 Basics

Charged cosmic rays (CRs) are high-energy nuclei and electrons that travel through space at nearly the speed of light. They are mainly protons ($\sim 89\%$), helium nuclei ($\sim 9\%$) and electrons ($\sim 1\%$) but also heavier nuclei up to uranium ($\sim 1\%$). Less than 1% of cosmic rays are antimatter, mainly positrons and few antiprotons. The most energetic CR has been detected by the Fly's Eye detector in 1991 with an energy of more than 10^{20} eV [6], which is tens of million times what particle accelerators can produce. This record earned the particle a surname: the Oh-My-God particle. Nevertheless, such events are rare. Since cosmic rays are charged particles, their trajectory can be bent many times by magnetic fields before being detected on Earth, making it impossible to know where they come from. The cosmic ray sky is therefore almost completely uniform. CRs are a rare sample of matter that comes from outside our solar system.

Solar flares, which are sudden increases of the Sun's brightness, can create CRs up to 10^{10} eV. Energetic CRs are mostly created in the blast waves of supernova remnants (SNR). After a supernova explosion, which happens about twice a century in the Milky Way [7], gas clouds carrying strong magnetic fields expand during thousands of years, bound by a shock wave. Speed, pressure and temperature are different upstream and downstream of the shock. Particles cross the shock back and forth; they bounce in a magnetic bottle and some of them gain enough energy to escape as CRs. For a monoatomic gas and an isotropic particle distribution, it can be shown that:

$$P_{esc} = \frac{v_u}{c_s} \tag{2.2}$$

$$E_n = \left(\frac{v_u}{c_s} + 1\right)^n E_0 \tag{2.3}$$

where P_{esc} is the escape probability, E_n is the energy of a particle after n crossings of the shock, E_0 is its initial energy, v_u is the speed upstream and c_s is the sound velocity in gas. This phenomenon is known as first order Fermi acceleration. The spectrum of the CRs created is a power law:

$$\frac{\mathrm{d}N(E)}{\mathrm{d}E} \propto E^{-\alpha} \tag{2.4}$$

where α is called the spectral index and equals about 2. This value is consistent with observations. About 100 years in the shock of a young SNR are sufficient to reach hundreds

of TeV. However, this process only allows to reach a limited energy, around 3×10^{15} eV for typical SNR magnetic fields of about 2 nT. Moreover, the gyro-radius r_g of a relativistic particle is given by:

$$r_g = \frac{\gamma m v_\perp}{|q|B} = \frac{E v_\perp}{c^2 |q| B} \tag{2.5}$$

where c is the speed of light, B is the magnetic field and $\gamma = E/(mc^2)$ is the Lorentz factor, E the energy, m the mass, $v_\perp$ is the velocity perpendicular to the magnetic field and q the charge of the particle. For a 10^{20} eV proton or electron in a 3 μG magnetic field[4], which is about the average magnetic field strength in the Milky Way, $r_g \simeq 30$ kpc which is about the radius of the whole galaxy. The highest energetic particles are therefore assumed to come from outside the Milky Way. Potential sources are active galactic nuclei (AGN) or gamma ray bursts (GRB).

Some of the cosmic ray sources can be traced by the ^{26}Al flux. In magnesium rich sources, like supernovae, the proton capture of ^{25}Mg synthesizes this radioactive aluminum isotope ($^{25}\mathrm{Mg} + \mathrm{p} \rightarrow {}^{26}\mathrm{Al}$). The latter decays with a half-life of about 7.2×10^5 years. Figure 2.2 presents the different steps of this process. First, one proton of ^{26}Al decays into a neutron releasing also a positron and a neutrino. This turns the ^{26}Al atom into a $^{26}\mathrm{Mg}^*$ atom in an excited state. The latter retrieves its stable ground state by emitting a photon at 1809 keV, in the gamma ray range. It is this specific emission that is used to trace cosmic ray sources.

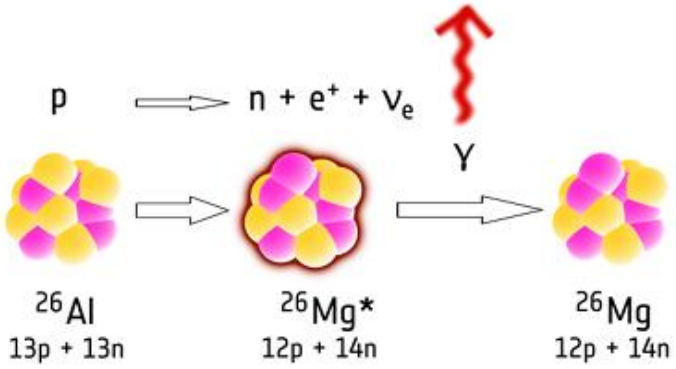

Figure 2.2: Radioactive decay of aluminium-26. Adapted from [8].

2.2.2 CR diffusion equation

After their creation, CRs propagate inside the galaxy. The main propagation process is the scattering off magnetic turbulences. The galactic magnetic field is very complex, as it is generated by many sources: stars and MCs at small scales and the galaxy itself at large scales. For CRs the dominant scattering mode is believed to be scattering of magnetohydrodynamic waves generated by the CR plasma itself. This process is called self-confinement of CRs. It bends CR trajectories. The interaction of CRs with other particles is a subdominant propagation process. CRs can also fragment or undergo radioactive decay. Only CRs with the highest energies can escape our Galaxy whereas CRs with lower energies are confined in it. GALPROP [9] and DRAGON, for Diffusion Reacceleration and Advection of Galactic cosmic rays: an Open New code [10], are two publicly available

[4]The gauss (G) is a unit of measurement of magnetic flux density. One gauss equals 10^{-4} tesla.

codes that provide numerical solutions for the CR propagation. Both solve the following CR transport equation in steady state:

$$\frac{\partial}{\partial t}n_i = q(\vec{r},t) + \vec{\nabla}\cdot[D(E,\vec{r},t)\vec{\nabla}n_i - \vec{V}n_i] + \frac{\partial}{\partial E}E^2 D_{EE}\frac{\partial}{\partial E}\frac{1}{E^2}n_i \\ - \frac{\partial}{\partial E}[-\frac{dE}{dt}n_i - \frac{E}{3}(\vec{\nabla}\cdot\vec{V})n_i] - \frac{1}{\tau_f}n_i - \frac{1}{\tau_r}n_i \quad (2.6)$$

where $n_i(E,\vec{r},t)$ is the space density of particle i at energy E, position $\vec{r}$ and time t, $q(\vec{r},t)$ is a source term, $D(E,\vec{r},t)$ is the diffusion coefficient, $\vec{V}$ is the convection velocity, τ_f is the fragmentation timescale and τ_r is the radioactive decay timescale. The first term on the right side, which is the source term, accounts for the primary CRs directly created by SNR and for the CRs created in the propagation process. The second term includes in first part a diffusion term. Lots of collisions imply a small mean free path: it takes time for a particle to escape a given region. In the galactic disk, the diffusion coefficient is expected to be smaller than in the galactic halo. The second part accounts for convection by the galactic wind. The D_{EE} term describes diffusive reacceleration, a second order Fermi acceleration process in the diffuse ISM. The fifth term are the energy losses. It accounts for interactions with the ISM, the ISRF or the galactic magnetic field which produce synchrotron radiation and gamma rays. More details about energy losses of cosmic rays are provided in part 2.3. The last two terms account respectively for fragmentation and radioactive decay that produce secondary CRs. GALPROP and DRAGON both provide the CR spectrum at each point of the galaxy for each CR species, mostly protons and electrons, for a given model of the galaxy, including and ISM and ISRF skymap. Another way of knowing the CR spectrum is by collecting data.

2.2.3 CRs seen from Earth

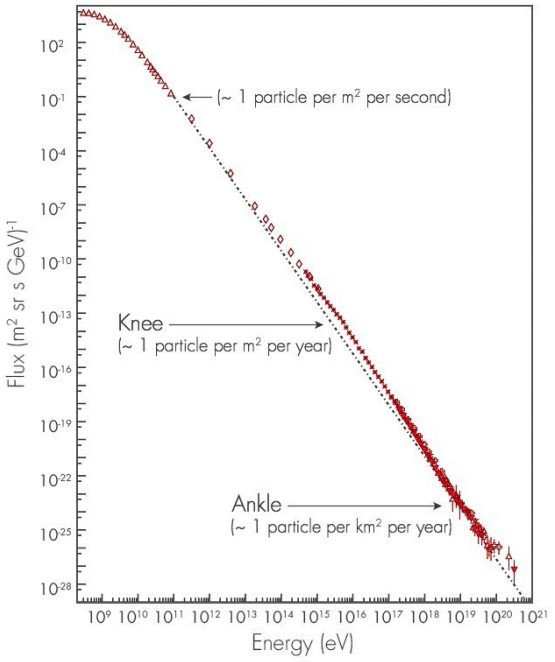

Figure 2.3: Cosmic ray spectrum seen from Earth [11].

The shape of the cosmic ray energy spectrum for all charged particles over all sky in the Earth's vicinity is shown in figure 2.3. As previously said, the spectrum is almost isotropic.

It extends from 10^8 eV to more than 10^{20} eV. It looks like a leg, with a knee at about 3×10^{15} eV and an ankle around 10^{18} eV, and it is composed of two power laws with different spectral indices (α_1, α_2). As seen earlier, SNR can only create CRs with a limited energy which is around the knee. Below the knee $\alpha_1 \simeq 2.7$. The solar magnetic field and wind impact the energy and the intensity of low energetic CRs. This is known as the solar modulation of CRs. Because of this phenomenon, the local (in the vicinity of the Sun but outside the Solar system) cosmic ray spectrum is uncertain and may differ from the data (collected inside the Solar system). Between the knee and the ankle $\alpha_2 \simeq 3$. Above the ankle the CRs spectrum starts to flatten. Neither the knee nor the ankle is completely understood. They may indicate a transition in the acceleration process, a change in composition or different energy loss processes.

The CR spectrum is known from many different experiments. Low energy data, below the knee, are collected from space by modules such as AMS-02 or PAMELA [12] which directly detect the cosmic rays. Around and above the knee, ground-based observatories such as HESS or Pierre Auger are used. They detect secondary particles created after the interaction of a CR with the atmosphere, also known as extensive air shower (EAS), thanks to the Cherenkov radiation they produce in air or in water. Finally, at the highest energies, around and above the knee, fluorescence light emitted by EAS is detected by ground-based instruments such as the Telescope Array Project. Direct detection from space is often more accurate but the CR flux decreases with energy: about one particle per square meter and per second is detected below the knee whereas only one particle per square kilometer per year is detected around the ankle. This makes necessary to have so large collecting areas that the observatories cannot be brought to space and need to be ground-based.

2.2.4 Dark matter searches in charged CRs

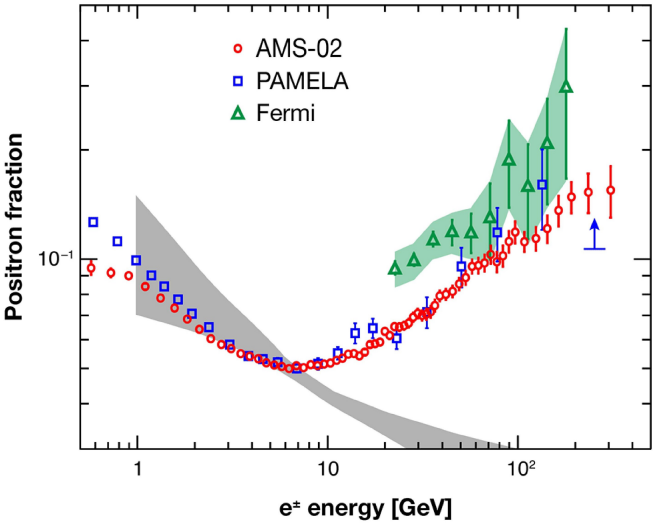

Figure 2.4: Positron fraction in cosmic rays seen by different experiments. The gray band is the expected positron abundance [13]. Image taken from [14].

Many pieces of evidence probe the existence of dark matter and a lot of them focus on its gravitational effects at cosmological and extragalactic scales, just like the rotation curves of galaxies and the weak lensing effect mentioned above. However, a probe of the particle nature of DM is missing. Two popular hypotheses are WIMPs: weakly interactive massive particles of a mass in the TeV range, and axions. Three approaches exist in order to search

the nature of DM: colliders, direct and indirect detection. The latter aims at detecting the signature of DM annihilation. This can be done in the flux of charged cosmic rays. As DM is its own antiparticle, it is expected to self-annihilate into particle-anti particle pairs. Antimatter is less abundant than matter in the Universe so the astrophysical background for antiparticles is also less strong which is favorable for analyses. Antimatter and matter are expected to be created in equal shares in the Big Bang. However, the currently observable Universe seems to be entirely composed of matter. The lack of observed antimatter is an open question. The small fraction of antimatter observed in CRs is believed to originate from CR interactions with the ISM. E.g. antiprotons and positrons can be created by the interaction of energetic protons with interstellar gas. On top of these rare interactions products a possible antimatter component from DM annihilation may be detectable. Figure 2.4 shows the observed and expected positron fraction in cosmic rays. There is an excess at high energies compared to predictions from astrophysics. This excess was explained with DM annihilation by several authors, even though astrophysical explanations exist.

2.3 From cosmic rays to gamma rays

Gamma rays are the highest energy photons, ranging from 100 keV to hundreds of TeV. They are produced by the most energetic and hottest objects and events. AGN and GRB are examples of extragalactic direct sources of gamma rays. Inside the Milky Way, direct sources are pulsars, SNR, X-ray binaries and star forming regions [15]. Gamma rays are also indirectly formed by CRs that interact with the ISM and the ISRF. This accounts for the diffuse gamma ray emission. Unlike CRs, gamma rays do not undergo any trajectory bending once created, as they are neutral particles. This means that they travel in a straight line from their emission region to the Earth, making it possible to study their distribution in the galaxy. They are produced by:

Proton cosmic rays (PCR)

CR protons that propagated to steady state react with gas of the ISM and produce π^0 particles. The latter then decay mainly into a pair of gammas with a branching ratio of 0.9882 in a characteristic time of 8.4×10^{-17} s [16]:

$$p_{CR} + X_{ISM} \rightarrow \pi^0 + Y \rightarrow \gamma + \gamma + Y \tag{2.7}$$

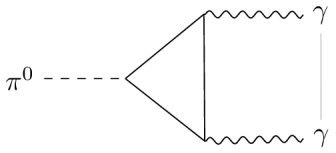

The local proton CR spectrum can be extrapolated from the data shown in figure 2.5. Previous work [17] showed that it can be approximated by an unbroken power law with a spectral index of 2.85 in the energy range relevant for this work, from 0.05 to about 500 GeV. Figure 2.5 shows the proton rigidity spectrum as measured by AMS and the approximated local proton CR spectrum used in the following. The latter differs from the first because of solar modulation and this effect only occurs inside the solar system. The rigidity of a charged particle measures its resistance to deflection from a magnetic field. The higher the rigidity of a particle, the straighter its trajectory. It is defined as:

$$R = pc/|q| \tag{2.8}$$

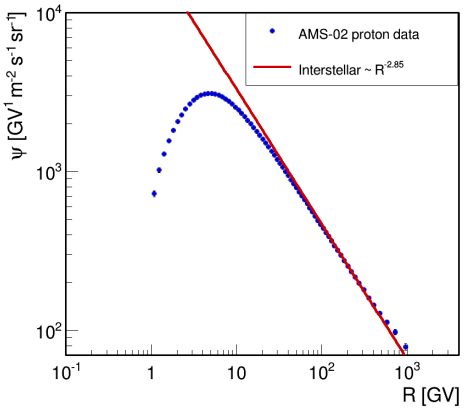

Figure 2.5: Local proton cosmic ray spectrum used in this work. It is approximated by a power law with a spectral index of 2.85. The proton spectrum seen by AMS-02 [18] is also shown. The x is the rigidity in GV which equals the energy in GeV for protons.

where p is the momentum of the particle and q its charge. For protons and electrons, $|q| = e$ so their rigidity in units of GV equals their energy in units of GeV. The y axis of the proton spectrum as well as most of the spectra shown in this thesis are in units of $GV \cdot m^{-2} \cdot s^{-1} \cdot sr^{-1}$ (or $GeV \cdot m^{-2} \cdot s^{-1} \cdot sr^{-1}$) which is not exactly a unit of flux but a unit of flux times energy square. The extrapolated proton spectrum is softer than the CRs spectrum created in SNR ($\alpha \simeq 2$), as high energetic protons had time to escape the galaxy.

Inverse Compton (IC) scattering

CR electrons interact with low energy photons of the ISRF. The electrons lose energy in favor of the photons:

$$e^-_{CR} + \gamma_{ISRF} \rightarrow e^{-'} + \gamma' \tag{2.9}$$

In the previous equation, $E(e^-_{CR}) > E(e^{-'})$ and $E(\gamma_{ISRF}) < E(\gamma')$, where E is the energy. More precisely, $E(\gamma') \sim \gamma^2_{e^-} E(\gamma_{ISRF})$ where

$$\gamma_{e^-} = \frac{1}{\sqrt{1 - \frac{v^2_{e^-}}{c^2}}} \tag{2.10}$$

is the Lorentz factor for an electron traveling at speed v_{e^-}. CR electrons are relativistic electrons so $\gamma_{e^-} \gg 1$.

Bremsstrahlung (BR)

CR electrons, while crossing the electric field of another particle in the ISM, are decelerated and emit high energy photons:

$$e^-_{CR} + X_{ISM} \rightarrow e^- + \gamma + X_{ISM} \tag{2.11}$$

The energy loss for electrons in the magnetic field of an atom is proportional to its atomic number Z.

CR protons also undergo IC scattering and BR but as they are about 1800 times heavier than electrons, these processes are negligible and protons do not create a significant amount

of gamma rays in this way.

In previous studies [17] sets of broken and unbroken power laws were tested in order to represent the electron spectrum. The best model was found to be a broken power law with two spectral indices and a break. The spectral index above the break can be deduced from the data and equals 3.21. The position of the break and the second spectral index can vary between 0.1 and 1.6 GV for the break and between 0.1 and 1.9 for the index. Figure 2.6 show different electrons spectra used in the following. Once again, solar modulation at low energies is not taken into account.

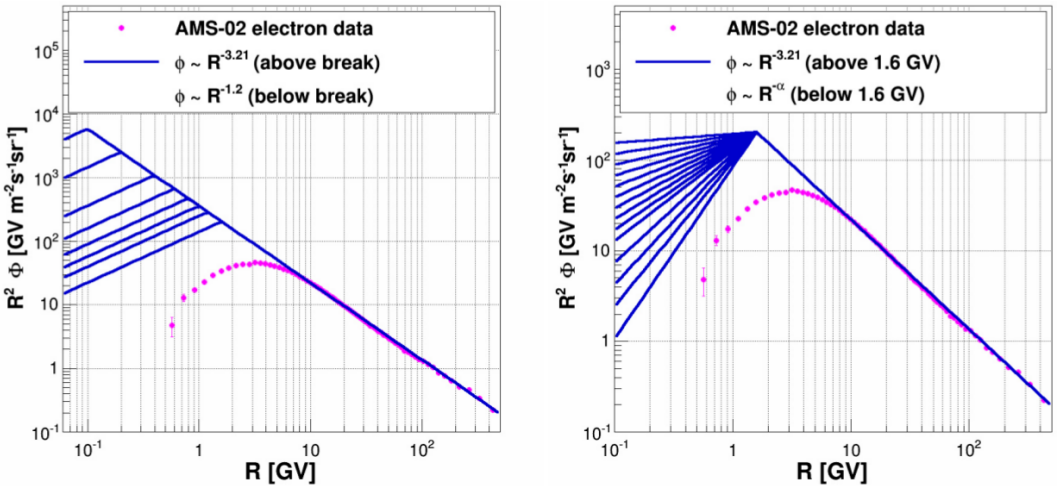

Figure 2.6: Electron cosmic ray spectra used in this work [19]. They are approximated by a broken power law with a spectral index of 3.21 above the break. The electron spectrum seen by AMS-02 [18] is also shown. Many different break positions (left) and spectral indices below the break (right) are shown.

In the three processes presented above, CRs lose energy via gamma ray emission. Further processes cause energy losses for CRs with no gamma ray emission: synchrotron radiation, Coulomb scattering and ionization. For nuclei, the two latter are the dominant energy loss modes. Figure 2.7 right shows the energy loss time for some nuclei due to these two processes. The time CRs spend in the Milky Way is smaller than the energy loss times for these nuclei, which means that their spectral shape does not vary significantly with position in the galaxy. In particular the extrapolated local CR protons spectrum of figure 2.5 can be used for the entire galaxy. Due to their low mass, electrons are also sensitive to synchrotron, inverse Compton scattering and Bremsstrahlung energy losses. Figure 2.7 left shows the energy loss time for electrons due to these five processes. As CR electrons undergo all of them, the total energy loss time is the one relevant in this work. Unlike protons, for electrons the energy loss time is smaller than the time CRs spend in the galaxy. Below 0.2 GeV, ionization and Coulomb scattering are the dominant energy loss modes just like for nuclei. At higher energies, synchrotron and inverse Compton scattering become the dominant modes. Electrons energy losses are not negligible and strongly depend on the ISM and ISRF spatial distribution, which means that the electron spectrum is assumed to vary over the galaxy: the break and the low energy index of figure 2.6 are different in each direction.

GAMMASKY is a code that calculates the spectra of the gamma rays created by PCR, IC and BR seen on Earth in each direction. It requires the CR electron or proton spectra as

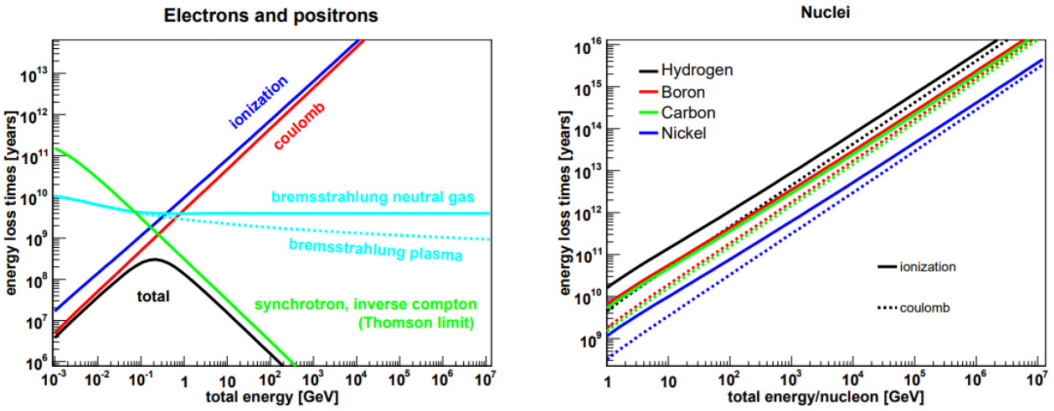

Figure 2.7: Energy loss times estimate for electrons and positrons (left) and for protons and other nuclei (right) in the Thomson limit (the energy density of photons equals the one of the magnetic field) and in gas with equal density of neutral and ionized hydrogen ($0.01/cm^3$) and no helium [20]. These energy and gas densities are about what CRs see on their way to Earth in average.

input as well as an ISM and an ISRF map. The following results only concern the energy range relevant for the rest of this work. For the isotropic power law proton spectrum, the PCR gamma ray spectra provided by the code have about the same spectral shape over the entire sky but not the same normalization. Figure 2.8a shows the superposition of all PCR gamma ray spectra normalized at a given energy. It is almost impossible to distinguish that this figure is the superposition of many templates so only one gamma ray spectra is kept for all the directions. In the following, the PCR gamma ray template is not considered as spatially dependent. The GAMMASKY normalization of all components is not relevant for the rest of this work. The same test can be performed for the BR gamma ray spectra. For one fixed electron spectrum given to GAMMASKY, which means one pair of low energy index and break, the output spectra are superimposed. Although the line in figure 2.8b is thicker than the one in figure 2.8a the BR gamma ray spectrum for a fixed CR spectrum can still be assumed not to be spatially dependent. However, at a fixed position but for different electron spectra the output gamma ray spectra vary a lot. In the end the BR gamma ray spectrum is spatially dependent through the low energy index and break of the electron spectrum in each direction. The superimposed IC gamma ray spectra, shown in figure 2.8c, present a variation of $\pm 10\%$ over the sky for a fixed electron spectrum, which means that they are spatially dependent. Nevertheless, for a fixed direction but varying electron spectrum, as shown in figure 2.8d, the IC gamma ray spectrum can be considered as constant. Unlike BR, the IC gamma ray spectrum is not spatially dependent because of a varying electron spectrum over the sky but because of position dependent fluctuations in the ISRF.

2.4 The Fermi Large Area Telescope

2.4.1 The detector

Unlike radio or visible photons, gamma rays cannot be focused through reflection or refraction. Thus, a gamma ray telescope is more similar to a particle detector than to a telescope. Moreover, the atmosphere is opaque to gamma rays so for direct detection, they need to be observed from space.

The Large Area Telescope (LAT) is a gamma ray space observatory. It is the main instrument of the Fermi spacecraft. It detects events in the energy range from few MeV

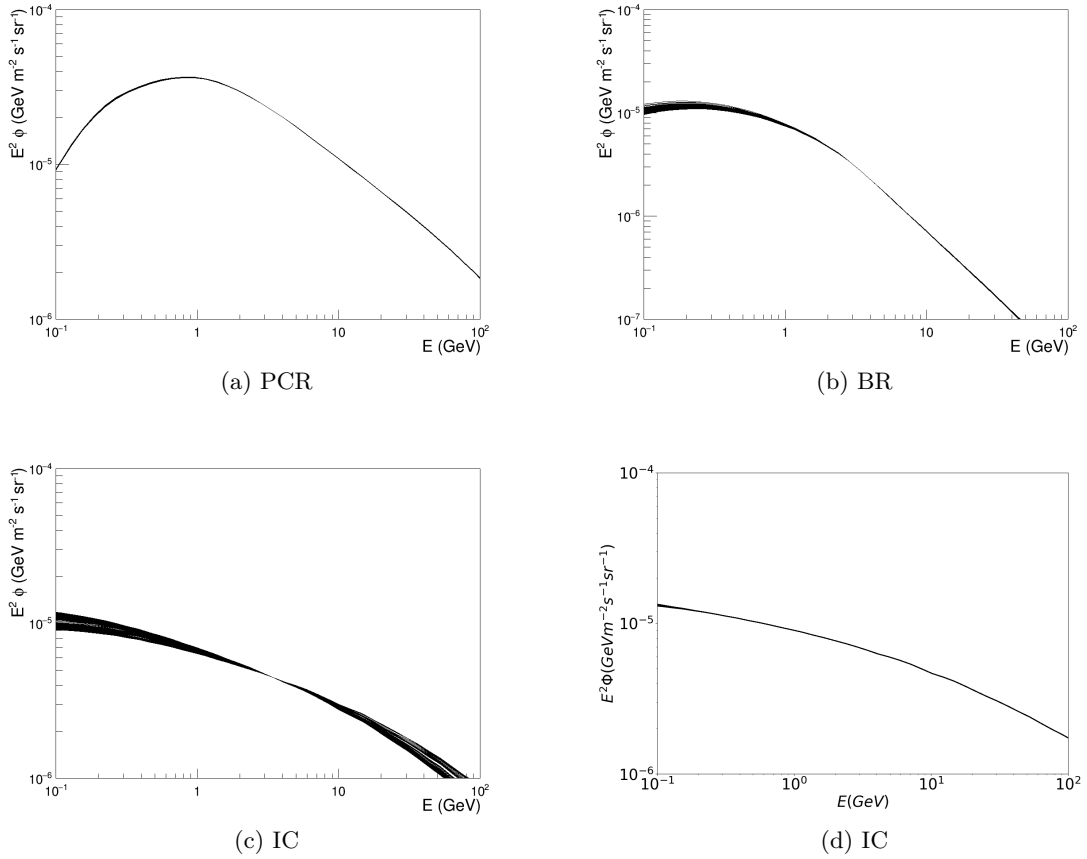

(a) PCR (b) BR

(c) IC (d) IC

Figure 2.8: Superimposed (a) PCR, (b) BR and (c) IC gamma ray spectrum for all directions and a fixed CR spectrum. The PCR and BR shapes can be considered as spatially independent. For two different electron spectra, the corresponding BR gamma ray spectra are not stackable (not shown). The IC template however is spatially dependent. Superimposed (d) IC gamma ray spectrum for all electron spectra and a fixed direction. The IC gamma ray template does not depend on the CR spectrum.

to hundreds of GeV in a large 2.4 steradians field of view [21]. EGRET, its predecessor embedded on the Compton Gamma Ray Observatory, could not detect events above 10 GeV. The LAT allows consequently to study the cosmos in the highest energy range, including events such as solar eruptions, relativistic jets, GRB or cosmic rays. The LAT circles Earth in 96 minutes at an altitude of 535 km. The Fermi spacecraft was launched on June 11, 2008 and was supposed to observe the sky during 5 to 10 years. It is still collecting data to this day.

The Fermi LAT is a pair production telescope. It is composed of a 4x4 array of detectors such as the one shown in figure 2.9a. Incoming events enter the telescope through an anticoincidence detector. This allows to reject charged particles such as CRs. Such events create a flash of light in the anticoincidence detector whereas gamma ray events do not. The detector is composed of 16 closely spaced parallel tungsten layers also called conversion foils. As their name suggests photons convert into secondary electron-positron pairs in one of these foils. The higher the energy of the incoming photon, the later it will produce an electron-positron pair. The 12 upper layers form the front or thin layer and the 4 remaining ones form the back or thick layer. Foils from the thick layer are thicker than the ones in the thin layer and favor multiple-scattering of electrons and positrons but offer a larger

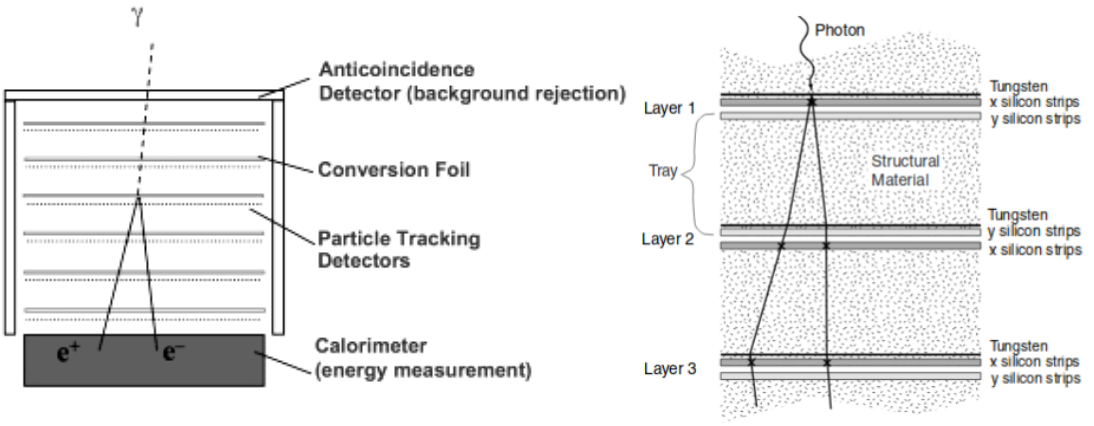

(a) (b)

Figure 2.9: The Fermi LAT detector [22].

field of view. Each tungsten layer also has an $x - y$ pair of silicon strips (see figure 2.9b) constituting a particle tracking detector in which electrons and positrons lose energy via ionization. The tracking detector allows to reconstruct the incident direction of the photon; this is called directional reconstruction. Below the 16 tungsten and silicon layers are two additional pairs of silicon strips and a calorimeter where electrons and positrons deposit their remaining energy. Together with the tracker, the calorimeter allows to calculate the total energy of the incoming photon. This is called energy reconstruction and with the directional reconstruction they form the event reconstruction.

Despite the anticoincidence plastic, some CR are detected as photons by the LAT. Together with extragalactic diffuse gamma sources and extragalactic unresolved sources, they form the isotropic background flux. As its name indicates, it is isotropic over the entire sky.

2.4.2 The LAT point spread function

The directional reconstruction of the LAT is limited by multiple scattering of electrons and positrons and by the thickness of the silicon strips. At low energies, below 10 GeV, the information on the photon direction can only be recovered thanks to the measurement points close to the conversion vertex because of multiple scattering. The further from the vertex, the longer the secondaries had to be scattered making it impossible to track back the photon incoming direction. Above 10 GeV multiple scattering does not play a role. That is why, together with the fact that high energy photons convert later than low energy photons, the tungsten foils in the back layer are thicker. Each measurement in layers below the vertex can be used. The directional reconstruction is now limited by the thickness of the silicon tracker detector. At a given energy, photons that convert in the back layer have a worse resolution than photons that convert in the front layer of about a factor two. More details about this discrepancy are provided in the following. However, thanks to the thick layer, the field of view and the effective area of the telescope increase at high energy. The reconstruction accuracy is not ideal and depends mainly on the energy of the photons and the layer where it pair-produces. The probability distribution function of the difference in direction between the true photons and the reconstructed photons at a true energy E is called the point spread function (PSF) of the instrument [23]. Figure 2.10 illustrates the PSF effects on a point source and extended sky regions.

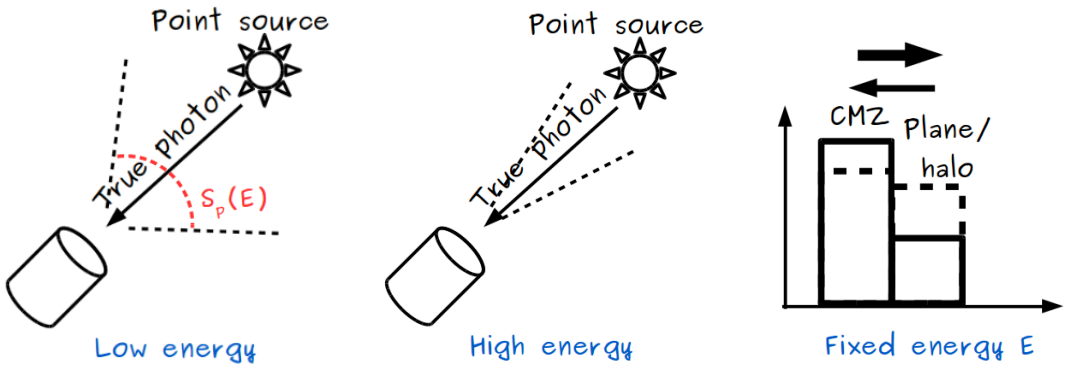

(a) (b) (c)

Figure 2.10: Illustration of the effect of the PSF. Full lines show true photons and dashed lines show reconstructed photons. (a) At low energy the PSF is wide and reconstructed photons appear to come from a large solid angle around a source. $S_P(E)$ is the 68% containment radius at energy E. (b) At high energy the PSF is small and reconstructed photons appear to come from a region close to the source. $S_P(E)$ is smaller at high energy than at low energy. (c) The CMZ is a region with high intensity next to regions of lower intensity such as the plane or the halo. Seen through a telescope more photons from the CMZ are reconstructed in the plane or the halo than vice versa. This effect become less and less important as the energy increases.

What is seen through the LAT are not true photons but reconstructed photons whose density peaks in the direction of true photons. At low energies reconstructed events by the LAT appear to come from a large solid angle around a source as shown in figure 2.10a. The PSF is said to be large or wide. At higher energies, the reconstructed photons appear much closer to the source as shown in figure 2.10b, the PSF is said to be small. The effect of the PSF almost disappears at the highest energies. The energy dependency of the 68% containment radius (or angular size) of the LAT PSF S_P is given by the following formula [23]:

$$S_P(E) = \sqrt{\left(c_0 \left(\frac{E}{100MeV}\right)^{-\beta}\right)^2 + c_1^2} \tag{2.12}$$

where the first term in the square root accounts for the multiple scattering and the second term for the thickness of the silicon strips. In the front layer, $c_0 = 3.65°$, $\beta \simeq 0.8$ and c_1 which is in fact the pitch angle uncertainty equals 0.07°. In the back layer, $c_0 = 7.05°$, $c_1 = 0.13°$ and β does not change. Figure 2.11 shows $S_P(E)$ for the front and the back layer. For a fixed energy, the angular size of the PSF is about twice larger for the back layer than for the front layer.

The PSF of the LAT blurs the real picture of the sky. For example, the gamma ray flux in the CMZ is much larger than in surrounding regions such as the plane or the halo. Because of the PSF, photons from the CMZ are reconstructed in the plane or the halo and vice versa, and as the CMZ is the brightest part of the gamma ray sky, more photons are reconstructed in the plane or the halo than in the CMZ. The difference in intensity between the two regions of the sky is flattened by the PSF, as illustrated in figure 2.10c. Data collected by the LAT are always convolved with the PSF, it is an unavoidable effect. Model predictions that are compared to the Fermi data need to undergo the same convolution

for a meaningful analysis. Alternatively, the Fermi data can be deconvolved. This last approach is discussed in part 3.3.

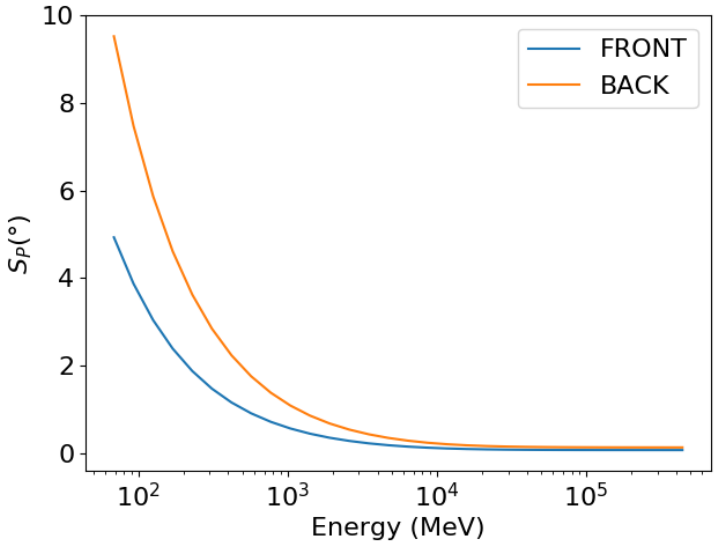

Figure 2.11: Angular size of the LAT PSF in the energy range relevant for this work calculated from equation 2.12.

2.4.3 The Fermi GeV excess

After the study of the data collected by the Fermi LAT, many groups reported the existence of an excess in the diffuse gamma ray spectrum around few GeV toward the galactic center [2] [24] [25], which is known as the Fermi GeV excess or the galactic center excess (GCE). It is particularly strong in the CMZ. The word "excess" underlines the fact that conventional models of gamma ray production including of PCR, BR and IC templates are not able to reproduce the data. Moreover, as seen in figure 2.12, the spectrum peaks at few GeV in the CMZ whereas it peaks at lower energies in the halo. The maximum of the spectrum appears shifted in the galactic center.

Many theories appeared over years in order to explain the GCE. Some groups interpreted it as a sign of dark matter annihilation [26], as its morphology was found to be almost spherically symmetric around the galactic center in their analysis, just like the NFW profile. Other authors suggested that it comes from milliseconds pulsars (MSP), which are fast rotating neutrons stars or white dwarfs and also gamma rays point sources. They may have not been resolved yet [27]. All these analyses used spatial information on the galactic gas distribution and the ISRF as an input to the analysis. These spatial templates for several gas components and the ISRF are fitted to the data for each energy bin. The spectral distribution of the emission associated to each spatial template is the output of the fit. Such an analysis does not allow to identify the physical emission components like Bremsstrahlung (from electron-gas interactions), π^0-decay (from proton-gas interactions) and inverse Compton scattering (from electron-photon interactions), but instead allows only to identify only the combined emission from electrons and protons interacting with a certain gas component and the emission from electron-photon interactions. Their fits generally return a spherical distribution of an excess signal, which lead to authors to search for signal sources that are spherically distributed. Contrary to these studies the present work does not input any spatial information to the analysis, but instead uses spectral information on the emission components from Bremsstrahlung, π^0-decay and inverse Compton scattering. This requires the assumption of electron and proton spectra which are taken from the

AMS-02 data (see section 2.3). These templates are fitted to the data for each pixel in the sky, and as a result the spatial distribution of the emission for each spectral template is derived. Such an analysis allows to identify the spatial distribution of each physical emission component. It is not able to differentiate between the emission from different gas components unless these gas components interact predominately with a CR population that has a different spectral shape. This is exactly the case for the proton population in MCs (MCR, see section 3.2) and for the freshly accelerated proton population interacting with diffuse gas in the vicinity if the sources (SCR, see section 3.2). The spatial extend of the excess, if no spatial information are inputted in the fit, seems to be correlated with the molecular clouds distribution. MCs are abundant in the CMZ where the GCE is particularly strong which leads some authors to think that MCs might be the cause of the excess.

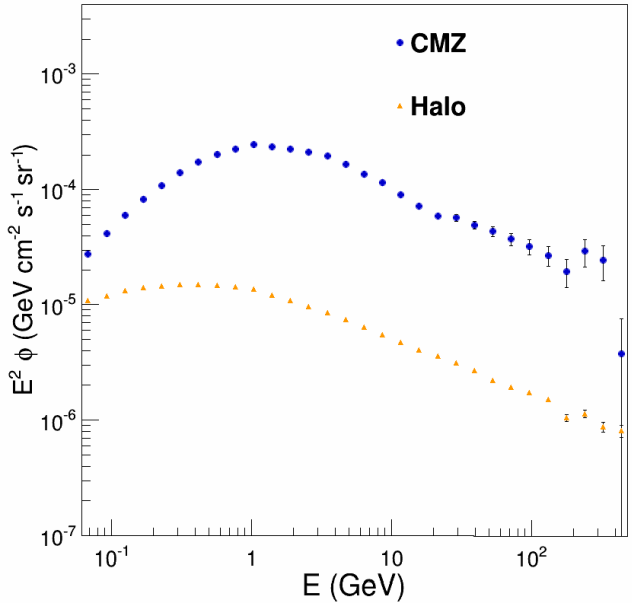

Figure 2.12: Halo and CMZ spectrum seen by the Fermi LAT. It peaks around 0.5 GeV in the halo and at about few GeV in the CMZ.

3 Method

This section presents the methods used in this work. First, it is explained how the Fermi LAT data are selected. Then, the fitting procedure already employed in previous work is detailed. The heart of this study which is the deconvolution of the data is developed in section 3.3.

3.1 Data selection

The Fermi LAT data consist of weekly files, available online [28]. Each file contains data acquired during one week. For this work, 561 weekly photons files covering a period of more than 10 years, from 4th August 2008 to 2nd May 2019, were used. At this point, data are represented in a table in which each line is an event and each column is one of its property, such as its energy, its position in the sky, its inclination θ with respect to the satellite (see figure 3.1) or its detection time. Each week, up to a few million events are detected. The first task is to reduce the data. This can be done by using the Fermi tools [29].

3.1.1 Filtering the data

Parameter	Cuts	Comment
Type	3	Front + back events
Class	256	Clean
Weeks	9 - 569	
Center (°)	RA = 266.4 DEC = -28.9	Galactic center
Radius (°)	180	Whole sky
Apparent zenith angle (°)	≤ 90	Recommendation
Time	no cuts	
Energy (MeV)	59 - 513000	

Table 3.1: First cuts on the Fermi-LAT data.

The first step is to realize cuts on the data, selecting only those events with specified properties. Thanks to the *gtselect* function, one can merge all the weekly files into one, define energy and time bounds, as well as a center and a radius inside which events should

have occurred. Every event that lies outside these cuts will not be kept thereafter. The cuts realized on the data for this work are presented in table 3.1.

The event type, which could be front, back or both, is related to the conversion layer of the incoming photon, more precisely to the tracker layer where the conversion occurred (see part 2.4.1). The event class refers to the residual background contamination from CR and should be chosen according to what one wants to study. There is one class called source, recommended for analysis of point and moderately extended sources. Another one is the ultraclean veto class, made for the study of diffuse gamma ray that require really low misidentified CR levels. The clean class used here is located between these two classes in the LAT event classes hierarchy. Finally, a maximal apparent zenith angle, named θ_z in figure 3.1, is needed to minimize contamination by photons created by CR interactions in the Earth's atmosphere. They are a strong source of background. The value of 90° is recommended by the Fermi team for event reconstruction above 100 MeV.

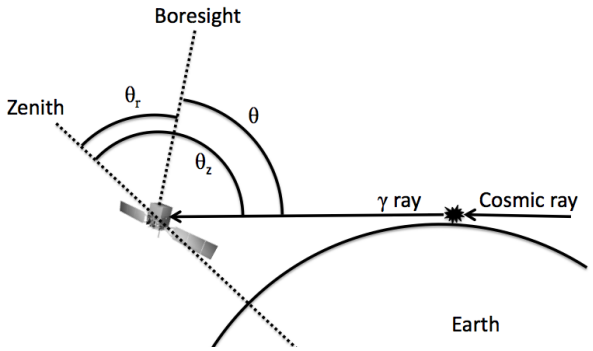

Figure 3.1: Definitions of the zenith angle θ_z, the rocking angle θ_r of the Fermi spacecraft and the incidence angle θ of an event [30].

No cut was performed on the detection time. However, even though one wants to study all the events that occurred in the selected period of time, some of them cannot be considered as valid, because of the spacecraft configuration. The function *gtmktime*, applied with the cuts recommended by the Fermi team allows to get rid of them. There are also periods during which the LAT does not collect data at all, for example when it maneuvers or when crosses the Southern Atlantic Anomaly. The latter is a region above the Earth where the Van Allen belt is closest to the surface and low energetic protons and electrons are trapped. These high radiations impact the electronics of the Fermi LAT so if data were collected at that moment, they would not be relevant.

3.1.2 Counts cubes and exposure cubes

Once the data are filtered, the idea is to plot them in a human readable way and this is what counts cubes are made for. One needs to choose a space and an energy binning. In this work, galactic coordinates are used and the whole sky is studied. All skymaps are binned in 0.5° or 1° square pixels, resulting in a set of 720×360 or 360×180 pixels respectively. The energy binning ranges from 59 MeV to 513 GeV and is composed of 30 logarithmically spaced bins, named E0 to E29. The bin borders and centers as well as the amount of counts in each bin are given in appendix B.1. The twelfth energy bin, called E11, is centered at 1.91 GeV which is about the energy of the galactic center excess, that is why many figures in the following are shown at that energy bin. With help from the properties of each event, mainly position and energy, the *gtbin* function creates one sky map for each energy bin. Each pixel of the skymap in each energy bin is filled with a whole

number of counts. An example of parameters used to create a counts cube for this work is provided in table 3.2. In a counts cube, an event is localized inside a pixel while in weekly files, the localization limited by the precision of the telescope. Counts cubes include less information but facilitate the analysis.

Parameter	Value	Comment
Coordinate system	Galactic	
Pixels in longitude	720	$x = l \in [0; 360]$ or $[-180; 180]$
Pixels in latitude	360	$y = b \in [-90, 90]$
Degrees per pixel	0.5	
Energy (MeV)	59 - 513000	
Energy bins	30	
Energy spacing	logarithmic	

Table 3.2: Parameters used for a counts or exposure cube of 30 energy slices binned into squared pixels of 0.5°.

As the satellite is orbiting around the Earth, it does not spend the exact same time looking at each part of the galaxy. Hence, a count map does not give a realistic picture of the gamma ray sky. Thanks to the history of the spacecraft, the *gtltcube* and *gtexpcube2* functions create exposure maps and exposure cubes. The latter are then used to convert counts cube into flux cube. An example of the latter is provided in figure 3.2 top.

3.1.3 Point source subtraction

The Fermi LAT collects gamma rays from diffuse sources as well as from point sources. In order to study only diffuse gamma rays, one needs to subtract a point source cube from the total cube (in flux or counts). This source cube is created thanks to the *gtsrcmaps* and *gtmodel* functions. The 4FGL catalog [15] lists the gamma ray point sources in the 0.05 GeV-1 TeV range and their spectral properties and has more than 5000 sources above 4σ significance. It is used to create a cube of the sources binned according to the *gtbin* parameters (table 3.2). In this work, only sources above 3σ significance are used. This map is then artificially convolved with the LAT PSF with the *gtmodel* function. The Fermi tools provide then a point source cube as it would be seen through the LAT that can be subtracted from the previous total cube to get a diffuse cube. A point source flux cube and a diffuse flux cube are shown in figure 3.2 middle and bottom.

The point source subtraction is not perfect. Counts can be under or over subtracted, resulting in an excess or a lack of diffuse counts. Over subtraction can produce negative counts and therefore negative flux in the diffuse cube. For example, at $(l, b) = (85, -38)$ in figure 3.2 bottom, which is a diffuse flux skymap, one can see a dark region corresponding to a negative flux. In figure 3.2 top and middle, which are respectively a full flux cube and source flux cube, there is no dark pixel at all. The negative flux therefore comes from the subtraction. In the following, these negative values are simply set to zero. A possible under subtraction cannot be detected and is therefore an unknown systematic in any analysis of diffuse gamma rays.

The three skymaps in figure 3.2 as well as all the skymaps presented in this work are in galactic coordinates. This means that the left and right borders are always connected, whereas the top and the bottom borders are not. Moreover, an equirectangular projection

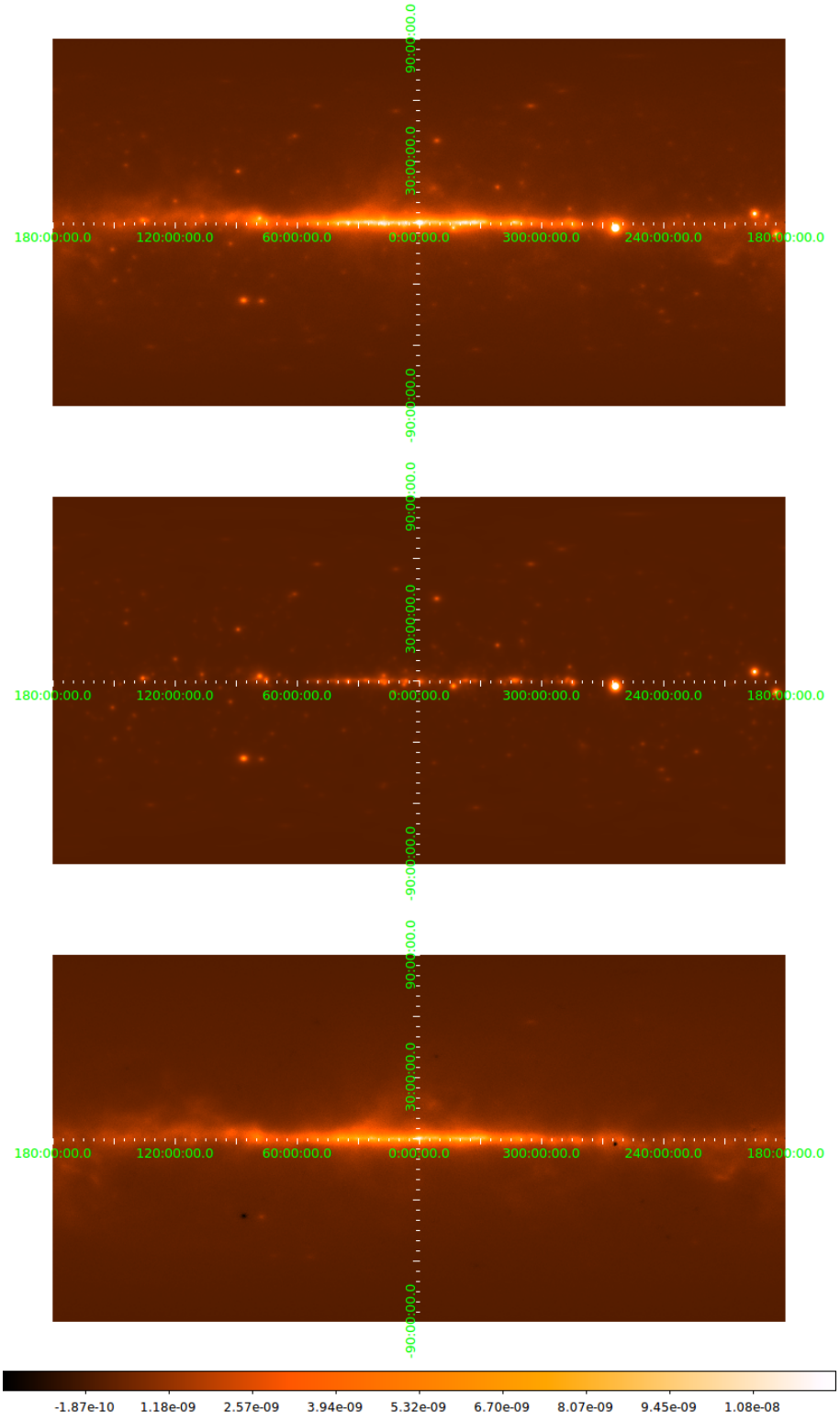

Figure 3.2: Full flux cube (top), point sources flux cube (middle) and diffuse flux cube (bottom) used in this work, shown at 230 MeV (slice 5) and binned with $0.5° \times 0.5°$ pixels. The x axis, which is longitude l, goes from 0 to 360°or from 180 to -180°. The y axis, which is latitude b, goes from -90 to 90°. The galactic center, located at $(l, b) = (0, 0)$ lies at the center of the maps. The z axis is flux in $ph/cm^2/s/MeV$. One can see some negative values (in black), for example at $(l, b) = (85, -38)$ in the diffuse cube, due to over subtraction in the point source subtraction process. These maps were created with the Fermi tools and plotted with the DS9 application [31].

is used, which implies that pixels of the same size (for example $1° \times 1°$ or $0.5° \times 0.5°$) do not subtend the same solid angle. The latter is smaller towards the poles than in the center, which means that the poles have a high spatial resolution, while the galactic plane has a lower spatial resolution. The projection is easy to understand by imagining that the surface of a globe is stretched out on a plane, with all latitudes an longitudes being parallel lines,respectively. In such a projection the North and South pole are stretched out to lines at $b = 90°$ and $b = -90°$. All the meridians, that appear parallel in equirectangular projection, actually converge at the poles.

3.2 Fitting procedure

This section is dedicated to the previous analysis of the Fermi data, partly reused in this work. For previous works, a smaller data set was used. The method presented in the following is a spectral fit that allows in the end to retrieve spatial information.

Once the 30 sliced diffuse cube is created, in which each slice is a map of the galaxy at a certain energy bin (like figure 3.2 bottom), a spectrum can be created for each pixel by plotting its flux as a function of energy. Tiny squared pixels can also be merged into bigger ones and freely shaped in order to study a whole area at once. A binning of 797 pixels of different shapes and sizes (referred to as binning A) was created in a previous work [17] in order to find a good balance between computation time, output quality and statistics. An overview of binning A is given in appendix B.2. The idea is then to fit the gamma ray PCR, BR, IC and eventually additional templates created by GAMMASKY to the Fermi LAT data for each pixel separately by minimizing the following χ^2:

$$\chi^2 = \sum_{i=1}^{n_E} \left[\frac{(D_i - \sum_{j=1}^{n} C_j T_{ij} - iso_i)^2}{\sigma_i^2} \right] \tag{3.1}$$

where $n_E = 30$ is the number of energy bins, D_i is the data flux at energy bin i, T_{ij} is the template j flux at energy bin i, C_j is the scaling factor of template j, n is the number of templates used for the fit, iso_i is the isotropic background flux[1] at energy bin i and σ_i is the error on the Fermi data at energy bin i. The error σ_i equals the quadratic sum of the systematic errors σ_i^{sys} and the statistical errors σ_i^{stat}. The systematic errors recommended by the Fermi collaboration are 10% below 100 MeV, 5% at 562 MeV and 20% above 10 GeV. For intermediate values, this error is calculated with a linear interpolation. The statistical errors are $\sigma_i^{stat} = 1/\sqrt{N_i}$ where N_i is the total number of counts in energy bin i. The minimization is performed with the Minuit package from ROOT [33]. The set of C_js that provides the lowest χ^2, is the one that fits at best the data. In other words, the fit results determine each template intensity. It is important to remember that the GAMMASKY normalization is irrelevant for this work and is not used at all. For each pixel separately, a total model spectrum is created, which is a linear combination of the templates plus the isotropic background. But best fit does not always mean good fit. To evaluate the quality of a fit, one has to calculate the ratio χ^2/dof where dof stands for degrees of freedom. Here, $dof = n_E - 1 - n$. The number of degrees of freedom is usually the number of data point (n_E) minus the number of free fit parameters (n). Is this particular case the number of data points is reduced by one due to the additional constraint that the total statistics in one pixel is fixed by the number of counts reconstructed in this pixel. This means that with $n_E - 1$ data points the entire spectrum is fixed. The closer to one the ratio, the better the fit. A $\chi^2/dof \gg 1$ usually means that the model cannot describe the data well. A $\chi 2 < 1$ usually means

[1] The isotropic background flux is taken from [32].

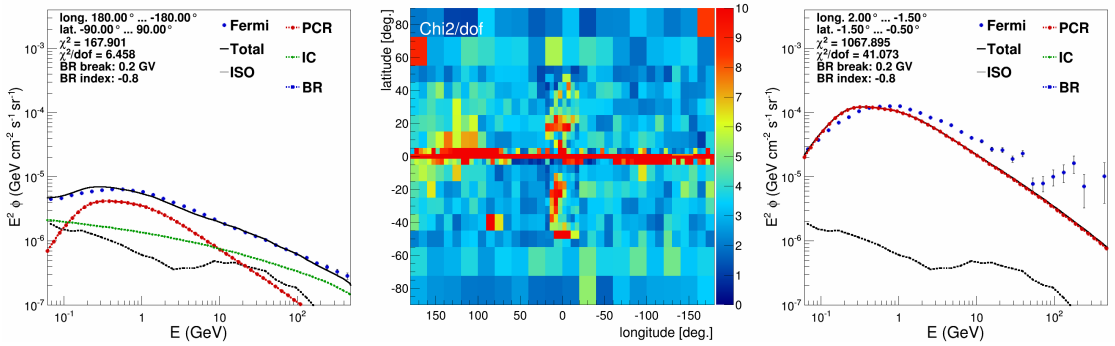

(a) Fit results for the whole sky. (b) Reduced χ^2 skymap. (c) Fit results in the CMZ pixel.

Figure 3.3: Whole sky fitted as one pixel (left) and results of a fit in binning A using only the three conventional templates and the isotropic background (middle and right). The electron spectrum was optimized independently for each pixel in this fit.

that either the model is over fitting the data or that the systematic errors are overestimated.

As previously said, many break positions and low energy spectral indices in the CR electron spectra are possible. As different CRs spectra can generate different gamma ray spectra (see figure 2.8), a whole set of BR gamma ray spectra is created by GAMMASKY, each one corresponding to a specific electron spectrum. In the fitting code, the user can decide to fix the unknown parameters to some chosen values, or to iterate over all possible values. In that latter case, all the spectra are tested one after another in the model and one χ^2 is minimized for each of them. The values that provide the best fit are kept.

If only the three conventional PCR, BR and IC gamma ray templates shown in figure 2.8, which means $n = 3$ in equation 3.1, and the isotropic background are used the fit returns bad results. Figure 3.3a shows the fit results for the whole sky taken as one single pixel. The reduced χ^2 value is higher than 6. For a fit performed in binning A, the reduced χ^2 values are particularly high in the galactic plane and towards the galactic center, as shown in the reduced χ^2 skymap[2] of figure 3.3b. In the CMZ pixel of binning A (figure 3.3c) the BR and IC contribution are so small that they do not even show up in the spectrum. The maximum of the PCR template does not coincide with the maximum of the data. One can also see that the total model would require a harder spectrum towards the highest energies. It was found previously that the data can be reproduced by introducing two additional templates.

Source cosmic rays (SCR)

Freshly accelerated CR protons in the expanding shock waves of point sources react in the vicinity of the later and produce π^0 particles that decay into photons. It is the same phenomenon as PCR but with a harder proton spectrum which is also an unbroken spatially independent power law with a spectral index $\alpha = 2.1$ shown in figure 3.4 left. This index is expected from diffuse shock wave acceleration [34]. Just as the PCR gamma

[2] A reduced χ^2 skymap is a way of showing all the χ^2/dof, that are calculated independently for each pixel, at once on a map of the sky in galactic coordinates. Each pixel is filled with the χ^2/dof value retrieved from the fit. All the reduced χ^2 skymaps shown in this work are truncated at $\chi^2/dof = 10$, which means that higher values are plotted as 10s.

ray template, the SCR gamma ray spectrum provided by GAMMASKY has the same shape in the entire galaxy. It is shown in figure 3.4 right. It has a hard energy tail and it is able to account for the observed spectral hardening of the gamma ray spectrum [35] [36].

Molecular cloud cosmic rays (MCR)

About 40% of the mass but only 1% of the volume of the ISM are composed of molecular clouds. MCs are complex, clumpy, filamentary systems that collapse to produce stars. If CRs were to penetrate MCs unmodified, the expected gamma-ray emission from interactions with the molecular gas would be identical to the PCR component discussed previously. Earlier one has seen that this assumption does not provide a good fit to the Fermi-LAT data. In fact, the χ^2/dof distribution in this fit (see figure 3.3b) achieves the highest values in the galactic plane, the region with the highest gas density, where also MCs form. MCs are dense objects which are accompanied by strong magnetic fields with energies comparable to their gravitational binding energy [37]. Their profile strongly peaks towards the center, meaning that most of the mass is encompassed in a relatively small and dense central core, surrounded by a magnetic dipole field. CRs entering this dense magnetic environment are are expected to be deflected by the magnetic field. This deflection will be stronger the lower the particle's rigidity is. This effect is observed in the Earth's magnetic field and called geomagnetic cutoff. The geomagnetic cutoff can be observed by CR detectors in the Earth's obrit, see e.g. the measurement of downward going primary particles with AMS-01 in figures 2 and 3 in [38]. At the same time the diffusion coefficient is expected to change inside molecular clouds due to wave damping below the ion-neutral mean free path. Throughout the ISM hydromagnetic waves in the cosmic ray plasma are damped by neutral particles carrying away energy from the waves. For a typical MC the ion-neutral mean free path is about 10^{-1} the size of the cloud [37]. Below this length scale there is no wave pressure support leading to a strong increase in the diffusion coefficient for CRs below a certain rigidity and low energy CRs freely (i.e. non-diffusively) propagate through MCs. This means that the free-streaming low energy CRs spend only little time in the dense environment of MCs, while the diffusive high energy CRs undergo multiple scatterings and spend more time in MCs. The interaction probability for low energy CRs is therefore significantly decreased compared to other regions of the ISM.

Both cases discussed above (magnetic cutoff and ion-neutral damping) are expected to occur in MCs. Their relative impact on the CR interaction rate is unknown and may strongly depend on the specific astrophysical conditions inside certain molecular cloud complexes. However, both processes lead to the same qualitative result: for magnetic mirroring the low rigidity CRs will be deflected from MCs, meaning the below a certain cutoff rigidity only few CRs are expected to enter the dense cores, which leads to a decreased density of low energy CRs inside MCs compared to the ISM. For ion-neutral damping the sudden absence of scattering centers for low rigidity particles will lead to free-streaming of low energy CRs. This, again, decreases the density of low energy cosmic rays inside MCs, simply because these particles leave the clouds much faster than other regions of the ISM. In both cases one expects a strong depletion of the CR flux in MCs below a certain cutoff- rigidity, which is either associated to the magnetic cutoff or to the mean free path of ion-neutral damping. This feature is characterized by a break in the CR proton spectrum, with two different slopes. Above the break, the spectral index is supposed to be the same as regular CR protons spectrum. The break position varies between 4 and 14 GV whereas the low energy index is fixed to 1.0. An example of a MCR protons spectrum with a break at 14 GV is provided in figure 3.4 left. The MCR shape was found in previous studies from the data [17]. The spectrum of gamma rays produced by MCR protons is shown in figure 3.4

right. Its maximum is around 2 GeV and is shifted in comparison to the PCR gamma ray spectrum.

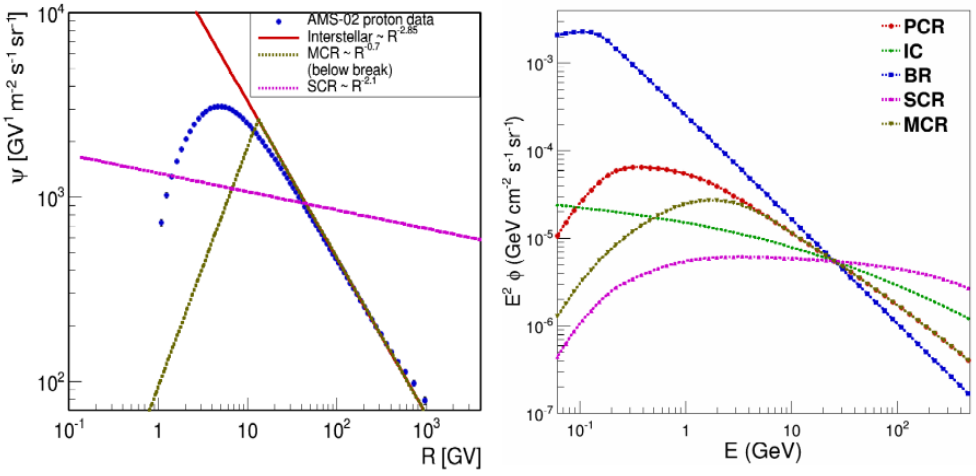

Figure 3.4: CR proton spectrum (left) for the PCR, SCR and one possible MCR component. The AMS-02 proton data are also provided for comparison. Example of possible gamma ray spectra provided by GAMMASKY (right) for the five processes presented earlier.

As the CR electron spectrum, the exact MCR proton spectrum is also unknown. It depends on the environment and might be different in each pixel. Many different MCR gamma ray spectra are created by GAMMASKY and are tested in the fitting code. Finally, one χ^2 value is calculated and minimized for each set of electron break, electron index and MCR index and only the best run is kept. Characteristics of the CR templates used to create the gamma ray templates are summed up in table 3.3.

Template	Break position (GV)	α_1	α_2
BR and IC electrons	0.1 to 1.6	0.1 to 1.9	3.21
PCR protons	/	/	2.85
MCR protons	4 to 14	1.0	2.85
SCR protons	/	/	2.1

Table 3.3: Spectral indices and breaks for the CRs templates used in this work. α_1 is the index below the break (broken power laws) and α_2 is the index above the break (broken power laws) or the global index (unbroken power laws).

Fitting the data with five gamma ray templates, PCR, IC, BR, SCR and MCR which implies $n = 5$ in equation 3.1, allows to well reproduce the data and its excess: the reduced χ^2 skymap (reproduced in chapter 4) is rather flat and close to one. Moreover, on the one hand, the resulting SCR morphology seen in the flux skymaps[3] of figure 3.5a reveals the Fermi Bubbles, two large structures discovered in 2010 located below and above the galactic center. They are thought to be the release of high energy jets emitted from the supermassive black hole at the center of the Milky Way. They are therefore rich in high energetic particles. Their spectrum has indeed a hard energy tail just like the SCR

[3] A flux skymap of component j at energy i is a way of showing the flux, that is calculated independently for each pixel, on a single map of the sky in galactic coordinates. Each pixel is filled with the $C_j T_{ij}$ retrieved from the fit. All the flux skymaps presented in this work have a truncated color scale: uncolored pixels are below the minimum and dark red pixels are above the maximum.

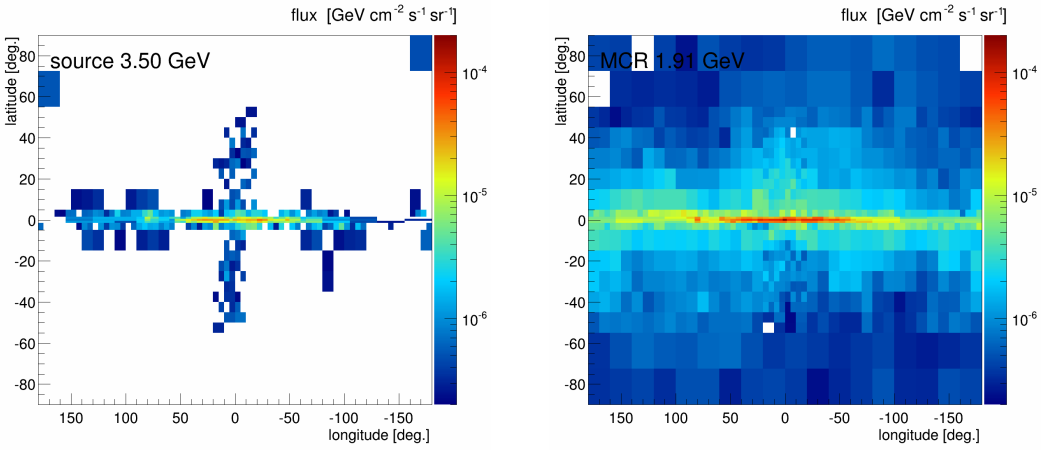

(a) Flux at E13. (b) Flux at E11.

Figure 3.5: Previous SCR (left) and MCR (right) flux skymaps in binning A.

template. All this corroborate the introduction of the SCR template. On the other hand, the resulting MCR morphology shown in figure 3.5b is correlated with the molecular clouds distribution [39], which support the idea of a different CR protons spectrum in MCs and the introduction of the MCR template. MCs are located in the galactic disk and are abundant in the CMZ, where the excess is particularly strong. All this means that the GeV excess could in fact be caused by molecular clouds. However, in previous works the PSF effect on the data has been neglected or assumed to be absorbed by the various break positions and spectral indices of the different templates. One aim of this work is to verify that getting rid of this effect does not affect the physics results.

3.3 Deconvolution

This section is dedicated to the deconvolution of the Fermi data. As seen earlier, data collected by the LAT undergo convolution with the PSF, which blurs the image of the true gamma ray sky (see part 2.4.2) and true photons from the CMZ are reconstructed in the halo and vice versa (figure 2.10c). This flattens the flux around the plane. One question arises: is there still an excess if the data are corrected for the PSF effect? And if so, will it lead to the same signal shape and signal distribution as previously found? Studies performing spatial fit have applied a PSF correction in the following way: prior to the fit, all spatial maps entering the fit were convolved with the instrument's PSF. Since the physical effect behind the PSF is a misassignemt of a single photon, the operation is linear, which means all spatial maps entering the fit can be convolved individually and then fitted to the data. In a spectral decomposition as applied in this analysis, a convolution before the fit is not possible. The reason for this is that the PSF can only be applied to a spatial map, since the gradient in the number of counts between neighboring pixels defines the flux from or to this bin. In a spectral analysis the spatial maps are unknown prior to the fit. They are only known once the fit is performed. To convolve the model prediction with the PSF in a spectral fit, the convolution would have to be applied at each iteration in the fit, prior to evaluating the χ^2. This procedure is computationally unfeasible. Instead, the data were deconvolved, i.e. the impact of the PSF was corrected for in the data and then compared to the unconvolved model. In the following, the first deconvolution method for the Fermi data is implemented and tested. Part 3.3.1 describes the method. The results of the deconvolution are presented in part 3.3.2. Finally, part 3.3.3 presents tests performed in order to check the quality, the stability and the limits of the method.

3.3.1 Deconvolution method

This subsection presents the first deconvolution method implemented for the Fermi LAT data. Its first part explains how the Fermi software is used to create a convolution and a deconvolution matrix for a base binning ($0.5° \times 0.5°$ or $1° \times 1°$) while the second part shows how to jump from these matrices to the ones in the fit binning, like binning A.

Base binning

The LAT PSF is complex and depends mainly on the energy and the conversion layer of the events. The Fermi tools offer a function called *gtmodel* that calculates and applies the PSF to a skymap. This function was used to create figures 3.6 and 3.7, that show the effect of the LAT PSF on a point source located respectively in the plane and towards the poles. The outputs of this function are in units of counts. This can be easily understood from part 2.4.2: the PSF makes the reconstructed photons jump away from their true pixel, so the PSF has a direct impact on photons which account for counts and not for flux. Indeed, in galactic coordinates the solid angle subtended by two pixels of the same size is not necessary the same and the exposure is not uniform over the sky so flux is not proportional to counts. One can notice that towards the galactic plane, the PSF appears relatively spherical whereas towards the poles, it seems to spread more in longitude and to flatten in latitude, due to equirectangular projection.

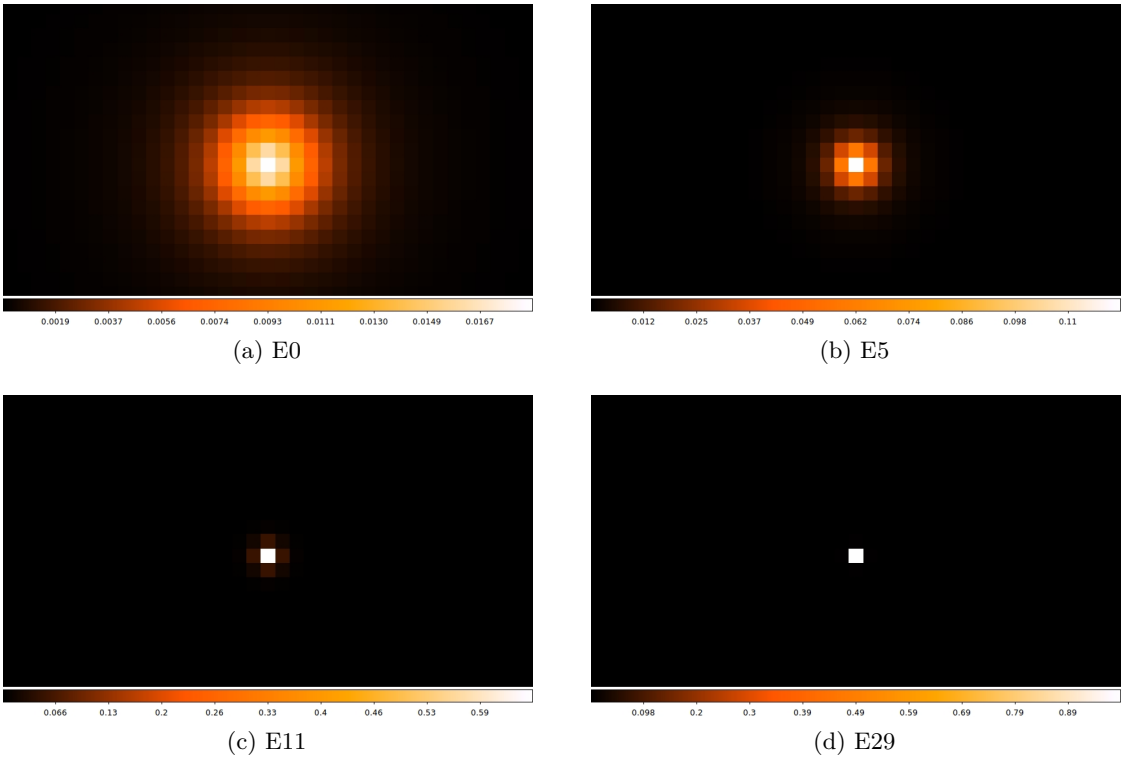

(a) E0 (b) E5

(c) E11 (d) E29

Figure 3.6: A test point source located at $(l, b) = (-0.5°, -0.5°)$ as it would be seen through the Fermi LAT at different energies for a sky binned in 1° squared pixels. These skymaps go from 18 to $-19°$ in longitude and from -9.5 to 10.5° in latitude. The z axes are normalized counts.

The first deconvolution method of the Fermi data, implemented in this work, is based on matrix multiplications. The idea is the following: skymaps are linearized as shown in figure 3.8a and treated as vectors. As data are collected by the LAT, they undergo

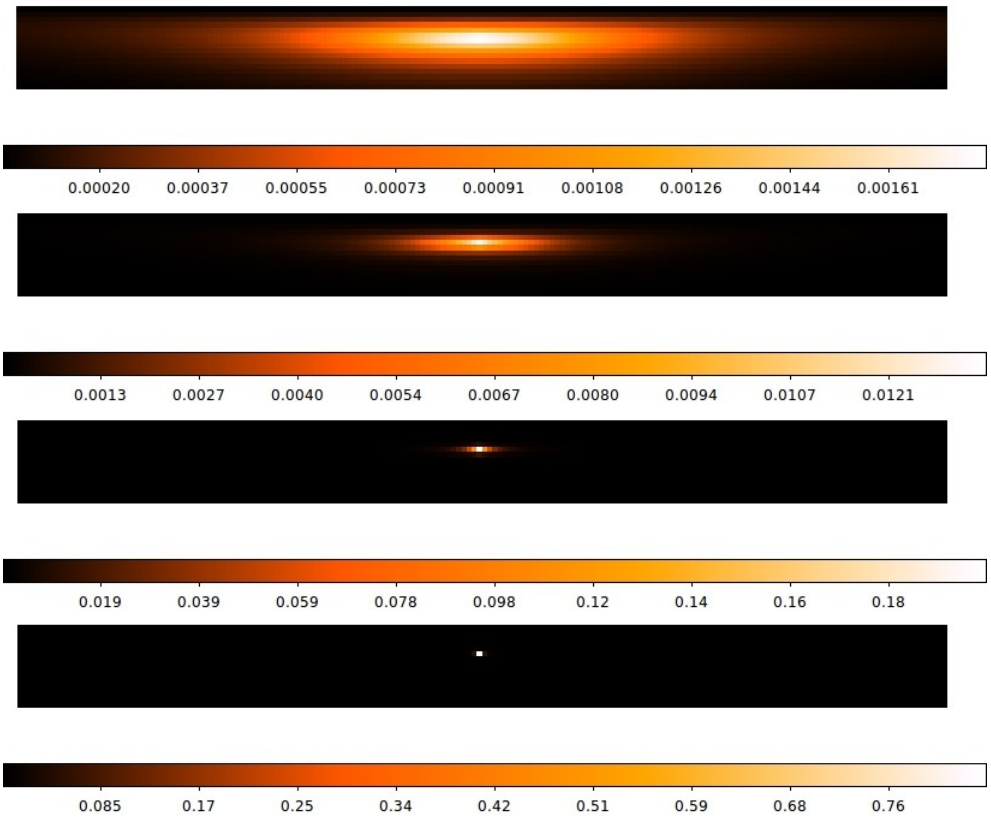

Figure 3.7: A test point source located around $(l, b) = (84.5°, -0.5°)$ as it would be seen through the Fermi LAT at different energies for a sky binned in 1° squared pixels. These skymaps go from 77 to $-77°$ in longitude and from 73 to 90° in latitude. From top to bottom: at E0, E5, E11 and E29. The z axes are normalized counts.

some modifications, they are convolved with the PSF and this can be mathematically represented by a multiplication of the data vector by a matrix, called the convolution matrix C_e. As the PSF is energy dependent, there is one convolution matrix per energy bin. This multiplication creates a new vector, which is yet convolved. The latter is the only one accessible with the LAT. To deconvolve the data, one needs to find the deconvolution matrix D_e, which is the inverse of the convolution matrix, and multiply it with the convolved data vector. In the following, "convolved data" refers to data seen through the LAT and with PSF applied, "real" data refers to data seen through an ideal detector which PSF has no effect and "deconvolved" refers to data seen through the LAT after deconvolution. For an ideal deconvolution, real data and deconvolved data are identical.

To create the convolution matrix, one needs to know the effect of the PSF on each pixel of a counts cube for each energy. To do so, a test point source is placed on a pixel called pixel a in the following while the rest of the sky remains empty as in figure 3.8.b. The value of the point source pixel is set to one so that the vector is normalized. The test skymap is then given to *gtmodel* which convolves it with the LAT PSF and returns a convolved skymap as it would be seen through the LAT; this is figure 3.8.c. One knows now on which pixels reconstructed photons are detected or in other words, what is the probability of a true photon from pixel a to be reconstructed in the other pixels. It was tested that *gtmodel* indeed preserves particle counts, i.e. the sum over all counts in the convolved skymap is again 1. The convolved skymap is linearized and the resulting vector forms the first column of the convolution matrix (figure 3.8.f). This operation needs to be repeated for each pixel

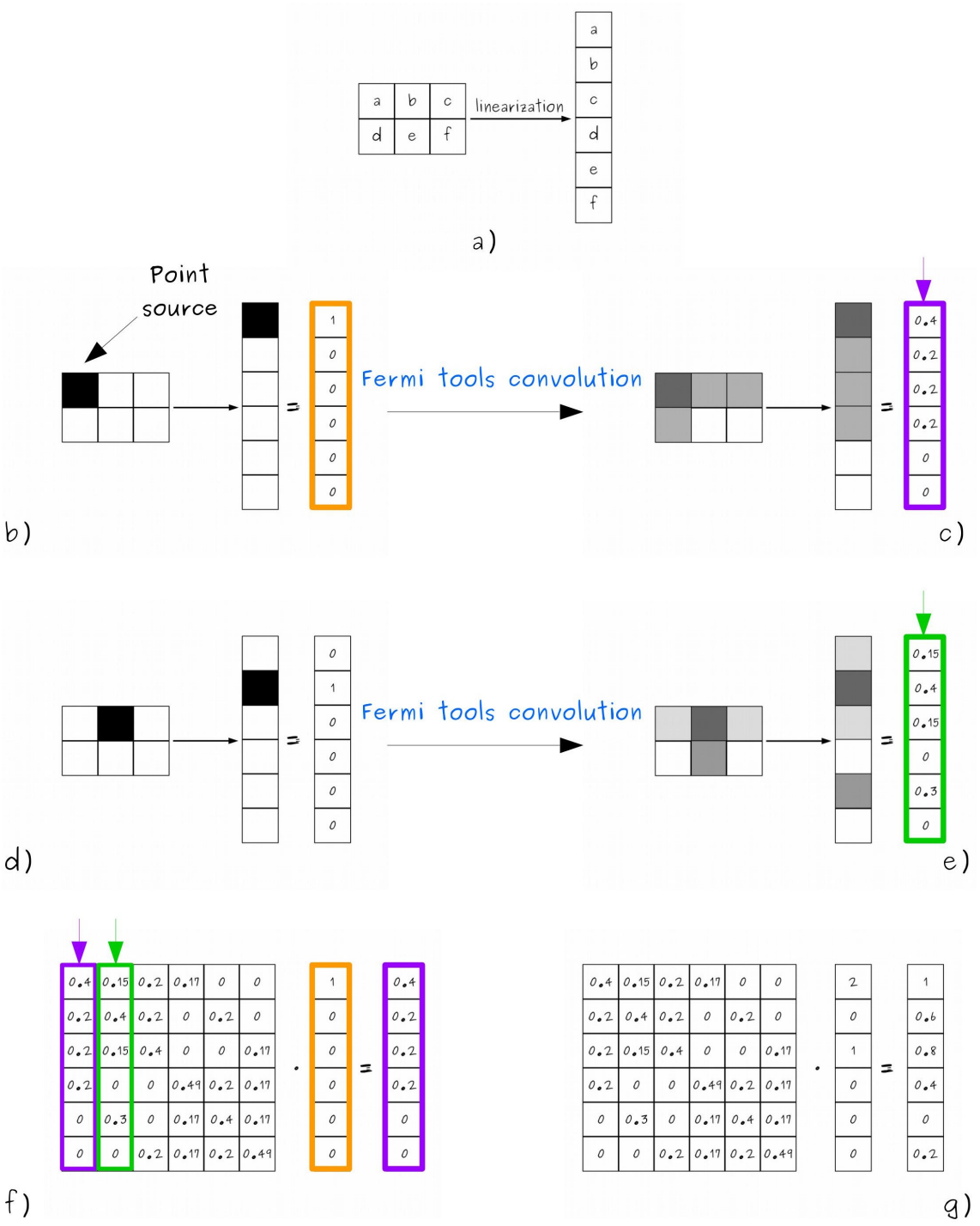

Figure 3.8: How to create a convolution matrix? Illustration on a toy skymap. a) Linearize all skymaps into vectors. The ordering of the pixels is arbitrary but has to be the same for all skymaps. b) Place a point source in the first pixel. The corresponding vector is filled with 0s except for the first element which is 1 for normalization purposes. c) Apply the PSF at a given energy to the skymap with the Fermi tools. The neighboring pixels are now filled. Pixels a and c do not appear to be neighbors on the skymap but they are in reality. The PSF conserves counts so the sum of all the elements of the vector equals 1. d) and e) Apply the same two steps to the next pixels. The effect of the PSF can change from a pixel to another. f) Column k of the convolution matrix is the convolved vector for which a point source was placed in pixel k. Multiplying the matrix with a linearized one-point source skymap generates the linearized convolved version of this skymap. g) The convolution matrix can be multiplied by any linearized skymap.

of the counts cube (figures 3.8.d and e). If the skymaps has n pixels then the size of the data vector is n and the size of the convolution matrix is $n \times n$. Each convolution matrix C_e can be written as:

$$C_e = \begin{bmatrix} p_{11,e} & p_{21,e} & \cdots & p_{n1,e} \\ p_{12,e} & p_{22,e} & \cdots & p_{n2,e} \\ \vdots & \vdots & \ddots & \vdots \\ p_{1n,e} & p_{2n,e} & \cdots & p_{nn,e} \end{bmatrix} \tag{3.2}$$

where $p_{ij,e}$ corresponds to the probability of an event that belongs to energy bin e truly located in pixel i to be detected in pixel j. Beware the order of the indices: the first index i is the column number and not the line number as in standard notation and the second index j is therefore the line number instead of the column number. In the example of figure 3.8, the vector $(p_{11,e}, p_{12,e}, \cdots p_{1n,e})$ would be the same vector as in figure c. The application of the PSF conserves counts, so that:

$$\sum_j p_{ij,e} = 1 \quad \forall i, e \tag{3.3}$$

which is also necessary for the $p_{ij,e}$s to be probabilities. This property explains why counts in figures 3.6 and 3.7 are not integers and smaller than one: the point source skymaps were normalized to one before convolution. For the data no normalization is performed on the skymaps and counts cube are always filled with integers. Another property related to probabilities is the following:

$$p_{ij,e} \geq 0 \quad \forall e, i, j \tag{3.4}$$

which is also a physics property: all counts detected are positive. If $p_{ij,e} = 0$ then pixels i and j are not linked by the PSF so that:

$$p_{ij,e} = 0 \iff p_{ji,e} = 0. \tag{3.5}$$

Moreover, for pixels not too close to the poles ($|b| < 80°$), most of the photons are reconstructed by the Fermi software in the true direction and therefore in the true pixel than in other pixels:

$$p_{ii,e} > p_{ij,e} \quad \forall e, j \neq i. \tag{3.6}$$

This inequality is expected for all latitudes: the photons should be mostly reconstructed in the true pixel. This unexpected behavior of the Fermi software was studied in detail and is believed to be a bug in the software, which might be caused by a wrong treatment of the boundary conditions towards the galactic North and South pole. Since the publicly available Fermi software is the analysis tool recommended by the Fermi-collaboration and should not be changed for reasons of reproducibility for a single analysis and since the polar regions are of minor interest for this study, the bug was left unfixed. At high latitudes ($|b| > 80°$), photons are reconstructed one or two degrees closer to the plane. As the width of the PSF is limited and with a large enough number of pixels, C_e contains many zeros located mainly far from the diagonal. As the energy increases, the PSF gets smaller, so that:

$$p_{ij,e1} = 0 \implies p_{ij,e2} = 0 \quad \forall i, j, e2 \geq e1. \tag{3.7}$$

At the highest energies C_e resembles an identity matrix. Once C_e is created, one needs to invert it to create the deconvolution matrix $D_e = C_e^{-1}$. If F_e is the vector of the convolved data seen through the LAT and N_e the vector of the deconvolved data at energy bin e, then:

$$N_e = C_e^{-1} F_e = D_e F_e. \tag{3.8}$$

If V_e is the vector of the real data at energy bin e and if the deconvolution is ideal, then:

$$N_e = V_e. \tag{3.9}$$

The counts conservation property of equation 3.3 implies there are as many photons in the Fermi convolved data than in the deconvolved data:

$$\sum_i N_e[i] = \sum_i F_e[i]. \tag{3.10}$$

It was checked that relations 3.3 to 3.7, as well as 3.10 hold. If D_e is written as:

$$D_e = \begin{bmatrix} q_{11,e} & q_{21,e} & \cdots & q_{n1,e} \\ q_{12,e} & q_{22,e} & \cdots & q_{n2,e} \\ \vdots & \vdots & \ddots & \vdots \\ q_{1n,e} & q_{2n,e} & \cdots & q_{nn,e} \end{bmatrix} \tag{3.11}$$

then equations 3.3 is also true for the $q_{ij,e}$s whereas equation 3.4 is not. Unlike the $p_{ij,e}$s the $q_{ij,e}$s are therefore not probabilities. They can be seen as contribution coefficients. If $q_{ij,e} > 0$ the contribution from pixel j to pixel i is positive which means that pixel i receives counts from pixel j in the deconvolution process. On the contrary if $q_{ij,e} < 0$ the contribution is negative and pixel i gives counts to pixel j. As the $q_{ij,e}$s are a long sum of products of $p_{ij,e}$ they rarely equal zero. Finally, by construction:

$$C_e D_e = D_e C_e = I_n \tag{3.12}$$

where I_n is the identity matrix of size n. Applying the LAT PSF and then deconvolving the data, both in the base binning, is like applying an identity function.

Fit binning

If data are binned as in the example of part 3.1.2, they are composed of $720 \times 360 = 259200$ pixels. Then, C_e must be of size 259200×259200. Not only it is hard to handle such a large matrix, but also it is memory intensive to invert it. Even with 1° squared pixels, there are still 64800 pixels in total. Moreover, it is sometimes not interesting to work with such small pixels. For example, statistics are small towards the poles ($|b| \geq 55^\circ$) so it is relevant to increase pixels size there. A binning most suitable for the analysis would have a high resolution in high statistics regions in the plane and a lower resolution towards the poles. The only requirement is that the new binning is based on the base binning in which data are binned. For example, the binning A mentioned earlier is based on a base binning of $0.5^\circ \times 0.5^\circ$. Indeed, the innermost pixels in latitude goes from -0.5 to 0.5° and with a

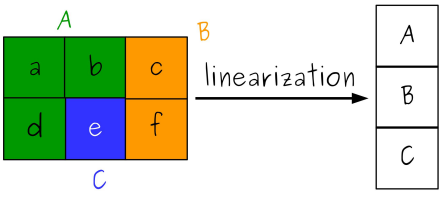

	A	B	C
a	1	0	0
b	1	0	0
c	0	1	0
d	1	0	0
e	0	0	1
f	0	1	0

Figure 3.9: A new binning of three pixels A, B and C can be created from a base binning of 3×2 pixels (left). The rebinning matrix R (right) allows to jump from the base binning to the new binning. $R[l,k] = 1$ means that old pixel l belongs to new pixel k. For example, new pixel A is composed of old pixels a,b and d. In the rebinning matrix, $R[a,A]$, $R[b,A]$ and $R[d,A]$ are filled with ones whereas $R[c,A]$, $R[e,A]$ and $R[f,A]$ are filled with zeros.

$1° \times 1°$ base binning, all pixel borders are whole degrees. An example of a rebinning of a skymap of 3×2 pixels into 3 pixels in given in figure 3.9 left.

Then, a rebinning matrix R that will allow to jump from a fine old binning including n pixels (with $n = 259200$ or 64800 for example) to a rougher new one, with only $m \leq n$ pixels is needed. R is of size $n \times m$ and is only filled with 0 or 1. $R[l,k] = 1$ means old pixel l belongs to new pixel k. Otherwise, $R[l,k] = 0$. This time l is the line number and k the column number. One old pixel can only belong to a single new pixel, so that:

$$\sum_k R[l,k] = 1 \quad \forall l. \tag{3.13}$$

Figure 3.9 right provides an example of a rebinning matrix from a base binning of 3×2 to 3 pixels. The data vector F_e^{nb} and the convolution matrix C_e^{nb} in the new binning are then:

$$F_e^{nb} = R^T F_e, \tag{3.14}$$

$$C_e^{nb} = nrm(R^T C_e R). \tag{3.15}$$

The function nrm normalizes the convolution matrix so that the sum of each column equals one. Indeed even in a new binning the $P_{ij,e}$ (here the capital letters stand for the new binning) are still interpreted as probabilities and equation 3.3 must hold in any binning, not only in the base binning. From a mathematical point of view, this sums up as:

$$\begin{aligned} B = nrm(A) &\iff B(l,k) = \frac{A(l,k)}{\sum_r A(r,k)} \\ &\implies \sum_l B(l,k) = 1 \quad \forall k. \end{aligned}$$

Equation 3.4 is therefore also true in the new binning. However, equation 3.6 is not necessarily true anymore and this depends on the morphology of the new binning. For example if the new binning is based on a $1^\circ \times 1^\circ$ binning and composed of two pixels, the first pixel being a single $1^\circ \times 1^\circ$ old pixel and the second pixel being the rest of the sky, then $P_{11,e}$ will probably be smaller than $P_{12,e}$ at low energies. In figure 3.6, the first and small pixel could be the one where the point source was placed: the brighter one. At E0 and E5, it is respectively filled with 0.0185 and 0.122 so the second big pixel is filled with 0.9815 and 0.878. So $P_{11,0} < P_{12,0}$ and $P_{11,5} < P_{12,5}$. However, if the probabilities are normalized by the solid angle, the maximum is located where the point source was placed. The solid angle of the small pixel is 0.01745 sr. Therefore:

$$\frac{P_{11,0}}{0.01745} = \frac{0.0185}{0.01745} = 1.060sr^-1 > \frac{P_{12,0}}{4\pi - 0.01745} = \frac{0.122}{12.5489} = 0.009722sr^{-1}. \quad (3.16)$$

If $sa(i)$ is the solid angle subtended by pixel i, then:

$$\frac{P_{ii,e}}{sa(i)} > \frac{P_{ij,e}}{sa(j)} \quad \forall e, j \neq i. \quad (3.17)$$

Equation 3.17 is also true for the $p_{ij,e}$s but for $|b| < 80^\circ$ the solid angle subtended by neighboring pixels is smooth enough to have no impact on the ordering of the probabilities. For the $Q_{ij,e}$, the matrix elements of the deconvolution matrix in the new binning, only equation 3.3 remains true.

Finally, the deconvolution matrix in the new binning is $D_e^{nb} = (C_e^{nb})^{-1}$. The order of the operations is important. $(C_e^{nb})^{-1}$ is different from $(C_e^{-1})^{nb}$ because of the nonlinearity of operator *nrm()*. The matrix inversion in a new binning of about 1000 pixels is visibly not as memory intensive as in a base binning and all matrix inversions in this work have been performed using the NumPy library of Python [40]. Equation 3.12 remains true in the new binning if n is replaced by m.

For the example from figure 3.9, new pixel A is filled with the sum of the values of old pixels a, b and d. For such a small example, obtaining the data and the convolution matrix in the new binning might seem obvious but to handle base binnings of tens of thousands of pixels, the rebinning matrix is handy. It is also important to note that the Fermi tools only allow smooth binnings with regular pixel size. An arbitrary binning such as binning A cannot be implemented in the Fermi software and therefore its deconvolution matrix cannot be created the same way as a base binning matrix. Moreover, the method presented here allows to jump quite easily from the base binning to any other one.

Figure 3.10 shows the convolution and the deconvolution matrices for binning A at E11. One can see a bright diagonal in each matrix and some geometrical structures impacted by the ordering of the pixels. The 72 first pixels are pixels located at high latitudes, towards the poles, where the angular size of the PSF is wide, due to the small area covered in these pixels. North pixels have all the same parity and all the South pixel share the other parity. It is important to remember here that East and West pixels on a skymap are adjacent in reality but North and South pixels are not. At low energies, all the North (South) pixels are connected via the PSF. That is why the first 72×72 sub-convolution matrix present a checked pattern. In binning A, the pixels in the plane cover the smallest region on the sky (see appendix B.2) due to high resolution and have the largest pixel numbers.

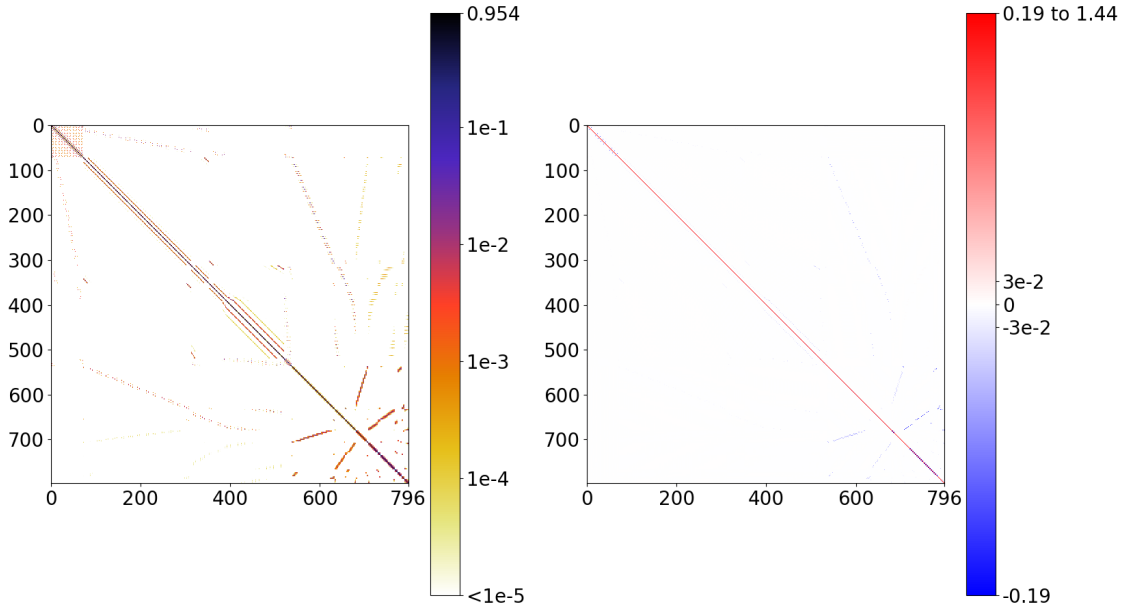

Figure 3.10: Convolution (left) and deconvolution (right) matrices for binning A at E11 centered at 1.91 GeV which is about the energy of the excess. The x and y axes are pixel numbers. The z scale is logarithmic for both matrices except between -0.03 and 0.03 where the scale is linear for the deconvolution matrix.

If one of these pixels is filled and the PSF is applied, the neighboring pixels get nearly as much counts as the filled pixel. Therefore, the width of the convolution matrix diagonal appears to increase at its end. At lower energies, both matrices resemble less the identity matrix whereas at higher energies they resemble more. The convolution and deconvolution matrices for energy bin 0 and 29 in binning A are given in appendix B.3.

Equation 3.12 which is theoretical must be verified in practice. Figure 3.11 shows the multiplication of the convolution matrix by the deconvolution matrix for energy bin 11 in binning A. For a readability purpose, the absolute value has been plotted. One can see a diagonal of ones surrounded by the same geometrical structures as in figure 3.10. Apart from the diagonal elements the largest values do not exceed 10^{-13} and are probably due to numerical instabilities. These values are small enough so that the result of the multiplication can be considered as the identity matrix of size 797. Similar results have been found for the 29 other energy bins. This means that applying the convolution matrix in this binning and then applying the deconvolution matrix also in this binning does not affect the data. All the results presented above are for binning A but similar results are found for the different fit binnings presented and used later in this work.

Systematics from binning

Binning the data tends to link together pixels that are not connected via the PSF in the base binning. In figure 3.8 pixels a and e are not connected via the PSF because it is too small. The matrix elements $p_{ae,E}$ and $p_{ea,E}$ in subfigure f equal zero for the corresponding energy bin E (and the ones above, not shown). On the contrary pixels b and e are connected via the PSF so $p_{be,E}$ and $p_{eb,E}$ are strictly positive. They might become zero at larger energies. After the rebinning of figure 3.9 pixels a and b now belong to pixel A and pixel e to pixel C. Pixels A and C are now connected via the PSF so pixels a and e are also connected.

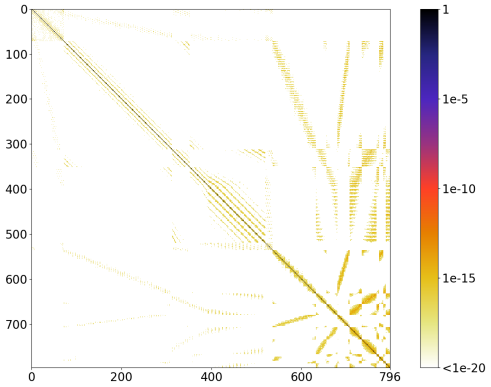

Figure 3.11: Matrix $C_{11}D_{11}$ in binning A. The minimal matrix element is -3.55×10^{-14}. For a readability purpose, the absolute value has been plotted. Matrix $D_{11}C_{11}$ provides similar results.

For example, the toy skymap of figure 3.9 can be filled with arbitrary numbers of counts. The corresponding linearized vector and the one rebinned thanks to equation 3.14 could be the following:

$$N_E = \begin{bmatrix} a \\ b \\ c \\ d \\ e \\ f \end{bmatrix} = \begin{bmatrix} 5 \\ 10 \\ 3 \\ 4 \\ 10 \\ 7 \end{bmatrix} \rightarrow N_E^{nb} = \begin{bmatrix} A \\ B \\ C \end{bmatrix} = \begin{bmatrix} 1 & 1 & 0 & 1 & 0 & 0 \\ 0 & 0 & 1 & 0 & 0 & 1 \\ 0 & 0 & 0 & 0 & 1 & 0 \end{bmatrix} \cdot \begin{bmatrix} a \\ b \\ c \\ d \\ e \\ f \end{bmatrix} = \begin{bmatrix} 19 \\ 10 \\ 10 \end{bmatrix} \tag{3.18}$$

The convolution matrix in the new binning can be calculated from equation 3.15 and the PSF can be applied in both binnings with a simple matrix multiplication:

$$F_E = C_E \cdot N_E = \begin{bmatrix} 0.4 & 0.15 & 0.2 & 0.17 & 0 & 0 \\ 0.2 & 0.4 & 0.2 & 0 & 0.2 & 0 \\ 0.2 & 0.15 & 0.4 & 0 & 0 & 0.17 \\ 0.2 & 0 & 0 & 0.49 & 0.2 & 0.17 \\ 0 & 0.3 & 0 & 0.17 & 0.4 & 0.17 \\ 0 & 0 & 0.2 & 0.17 & 0.2 & 0.49 \end{bmatrix} \cdot \begin{bmatrix} a \\ b \\ c \\ d \\ e \\ f \end{bmatrix} = \begin{bmatrix} 4.78 \\ 7.6 \\ 4.89 \\ 6.15 \\ 8.87 \\ 6.71 \end{bmatrix} \tag{3.19}$$

$$F_E^{nb} = C_E^{nb} \cdot N_E^{nb} = \begin{bmatrix} 0.67 & 0.285 & 0.4 \\ 0.173 & 0.63 & 0.2 \\ 0.157 & 0.085 & 0.4 \end{bmatrix} \cdot \begin{bmatrix} 19 \\ 10 \\ 10 \end{bmatrix} = \begin{bmatrix} 19.58 \\ 11.587 \\ 7.833 \end{bmatrix} \tag{3.20}$$

As one can see in figure 3.9, pixels e and C are exactly equals. However, after the convolution in two different binnings, they are not filled with the same value: 8.87 in the base binning and 7.83 in the rougher binning. As these values are also counts, they should be integers so they are always rounded and this is always done in the following after deconvolution. This gives respectively 9 and 8 counts. The contribution of pixel A to pixel C is an average of contributions from pixels a, b and d to pixel e but some of the old pixels do not communicate together in reality. Convolution in the base binning can provide different results as convolution in the fit binning and this is also true for deconvolution. Rebinning the data can therefore induce systematics. The choice of the fit binning is crucial

to limit this effect.

Rebinning the data before or after (de)convolution does not provide similar results. One can use the result of equation 3.19 and the rebinning matrix to obtain a vector of three elements:

$$R^T \cdot F_E = \begin{bmatrix} 1 & 1 & 0 & 1 & 0 & 0 \\ 0 & 0 & 1 & 0 & 0 & 1 \\ 0 & 0 & 0 & 0 & 1 & 0 \end{bmatrix} \cdot \begin{bmatrix} 4.78 \\ 7.6 \\ 4.89 \\ 6.15 \\ 8.87 \\ 6.71 \end{bmatrix} = \begin{bmatrix} 18.53 \\ 11.6 \\ 8.87 \end{bmatrix} \tag{3.21}$$

which is different from the result of equation 3.20. The impact of this will be studied in subsection 3.3.3.

Same for the deconvolution matrix: rebinning the convolution matrix before and after inverting it produces different results. Here is an example on the same matrices as above:

$$(C_E^{-1})^{nb} = \begin{bmatrix} 17.87 & -3.8 & -47.3 \\ 0.87 & 1.7 & -4.3 \\ -17.74 & 3.1 & 52.6 \end{bmatrix} \neq (C_E^{nb})^{-1} = \begin{bmatrix} 2.08 & -0.71 & -1.73 \\ -0.33 & 1.82 & -0.57 \\ -0.75 & -0.11 & 3.30 \end{bmatrix} \tag{3.22}$$

3.3.2 Deconvolution of the Fermi LAT data

Once the deconvolution matrix is created, one only needs to multiply it with the linearized skymap vector to obtain deconvolved data. However, it is important to keep in mind that when the data are reconstructed by the detector there is no binning included in the process. The convolution of the data by the LAT is not performed in any binning, not even in the base binning which is only the binning in which the user choses to bin the data in the Fermi software. The only limit is the precision of the detector, which is different from the accuracy of the detector that is responsible for the width of the PSF. Even if equation 3.12 has been verified numerically it does not apply here because the data are not convolved using the matrix multiplication. The deconvolved data might therefore differ from the real data. Moreover, the fit binning can connect pixels via the PSF that are not connected in the base binning and this is a second source of errors (see part 3.3.1 **Systematics from binning**).

The first binning in which the Fermi LAT data were deconvolved was the binning A, which is based on a $0.5° \times 0.5°$ base binning. It has very large pixels towards the poles (20° in longitude $\times 17.5°$ in latitude), smaller ones in the halo and very fine ones in the galactic disk, down to 1° in latitude. The two regions located just below and above the galactic center were binned with pixels size that allows to study the Fermi bubbles. As previously said, this binning was created in a preceding work in order to be the best fit binning possible and its number of pixels (797) is small enough to allow a reasonable memory intensive matrix inversion.

Deconvolution worked for the 28 highest energy bins, from E2 to E29 and acted as explained in figure 2.10c. The innermost part of the disk, between -1.5 and $1.5°$ in latitude, is the brightest part of the galaxy and therefore is surrounded by a less bright part. After

deconvolution, counts should move mostly towards the inner disk that ends up even brighter, whereas the surrounding part loses counts. In the halo, the flux is almost isotropic so deconvolution should have nearly no impact. This is what is observed in figure 3.12b that shows the data before and after deconvolution in the third energy bin (E2). This bin is the lowest bin in which deconvolution worked and therefore also the one out of the 28 working energy bins that is the most impacted by the PSF. For higher energies, as the angular size of the PSF is much smaller, deconvolved data look more and more like the raw data.

The deconvolved skymaps at the two lowest energy bins showed negative counts in some pixels in the plane, which are not physical since event numbers can only be positive. As the angular size of the PSF gets smaller as the energy increases, it makes sense that the problem occurs only at E0 and E1, the lowest energy bins. At E0 (E1), 56 (15) pixels got negative counts after deconvolution adding up to -2306757 (-116902) counts. The extreme values are -292 (-256) and -168844 (-24168). Negative counts mean that the deconvolution over subtracted some counts from a pixel. More counts left this pixel for another one than arrived or stayed. This problem can be caused by the two sources of errors mentioned earlier (limited precision of the PSF and pixel connection via binnings) or by a strong gradient in counts in neighboring data pixels which induce strong exchanges of counts between pixels and potentially over subtraction. Moreover, the Fermi software is assumed to provide the true point spread function with limited precision but there could be a discrepancy between the software and the LAT convolution. Figure 3.12a shows data before and after deconvolution for the first energy bin (E0). Each white pixel is a pixel that contains negative counts. Most of them are located in the plane. Each of these white pixels in the plane is surrounded by two pixels with a large number of counts above and below it or surrounds, with another white pixel, one pixel with a large number of counts. The counts distribution in the three rows of pixels in the plane seems to be wrong: some of the pixels are too bright and some others are not bright enough, sometimes even filled with negative counts. For example, at $l = 170°$ in the plane, the innermost pixel became extremely bright after deconvolution and by comparison with the data this does not seem physically possible. Only one white pixel is not located in the plane but in the lower part of the halo. One can notice that it is located around $(l, b) = (85, -38)$ which is a region where point sources were over subtracted (see figure 3.2), creating a negative fluxes and counts. Replacing all negative counts by zero in this region does not seem to be a sufficient correction. The quality of the point source subtraction also impacts the results of the deconvolution. This negative count issue shows the limits of the matrix deconvolution method.

In order to get rid of the negative counts, the pixels in the plane were merged before deconvolution. In binning A, the plane extends from $b = -1.5°$ to $b = 1.5°$ and is composed of three slices of 39 pixels of $1°$ in latitude. These three slices were merged into one to create a new binning of 719 pixels called binning B. This new binning requires its own 719×719 convolution matrix that is then inverted and used to deconvolve the data. To obtain this new matrix, one can consider binning A as a base binning and binning B as a fit binning and create a rebinning matrix that jumps from the first binning to the second just like explained in part **Fit binning** of part 3.3.1. Relevant characteristics of binning A and B are summed up in table 3.4. After deconvolution, on the one hand, at the first two energy bins, there is only one remaining pixel with negative counts, located at $(l, b) = (256, -3)$. It is not in the plane anymore but just below. On the other hand, this pixel also got negative counts up to the sixth energy bin. This demonstrates that deconvolution can be highly sensitive to small changes. Merging the pixels in the plane decrease the definition in the most interesting part of the sky. Having $3°$ in latitude pixels in the plane is too rough to

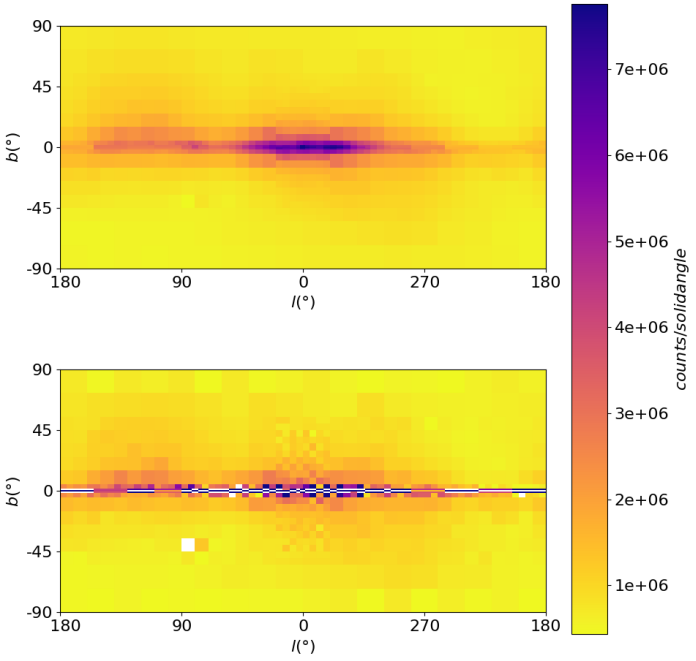

(a) E0

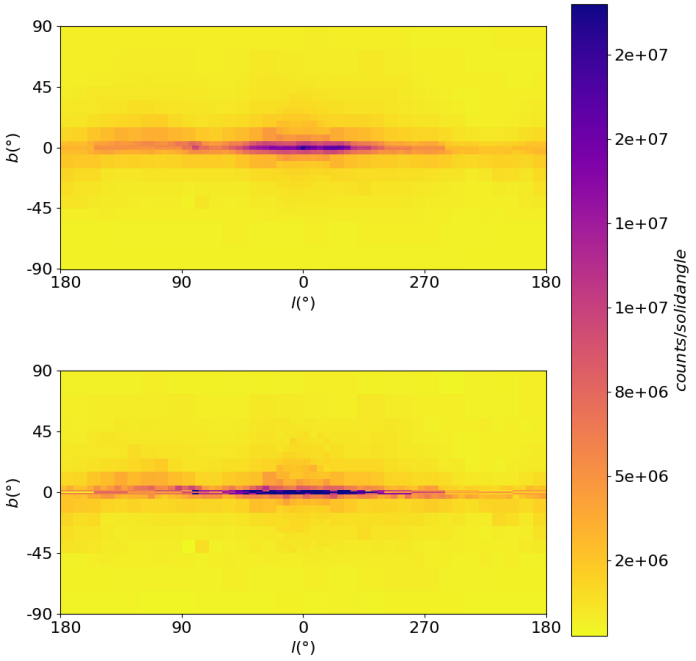

(b) E2

Figure 3.12: Data (a and b top) and deconvolution (a and b bottom) in the binning A for E0 and E2. Each uncolored pixel contains negative counts. The z axis is in units of $counts/sr$ for a readability purpose, but deconvolution is performed with counts.

detail all the structures.

Binning	Number of pixels	Plane	CMZ pixel
A	797	$-1.5° < b < 1.5°$	$-0.5° < b < 0.5°$, $-1.5° < l < 2°$
B	719	$-1.5° < b < 1.5°$	$-1.5° < b < 1.5°$, $-1.5° < l < 2°$
J1	719	$-2° < b < 2°$	$-2° < b < 2°$, $-2° < l < 3°$
J2	861	$-3° < b < 3°$	$-1° < b < 1°$, $-2° < l < 3°$
$J2_{up}$	861	$-2° < b < 4°$	$0° < b < 2°$, $-2° < l < 3°$
$J2_{down}$	861	$-4° < b < 2°$	$-2° < b < 0°$, $-2° < l < 3°$
$J2_{left}$	861	$-3° < b < 3°$	$-1° < b < 1°$, $-1° < l < 4°$
$J2_{right}$	861	$-3° < b < 3°$	$-1° < b < 1°$, $-3° < l < 2°$

Table 3.4: Main characteristics of different binnings used in this work.

The challenge was then to find a good balance between a deconvolution without negative counts and a fine binning. Negative counts were an unexpected problem. As all the previous works were realized in binning A, there was no need at first to deconvolve the data in a different binning. Thus, the 797×797 convolution matrices were created using a different method than the one presented above. No native $0.5° \times 0.5°$ pixels matrices were available at that point. A question therefore arose: start again from scratch with $0.5° \times 0.5°$ pixels or $1° \times 1°$ pixels? Both have advantages and drawbacks. The second option was finally chosen because it was the least time and storage consuming solution. Unlike binnings A and B, all new binnings will be based on a $1° \times 1°$ binning.

Applying the PSF with the Fermi tools to each of the 64800 pixels took more than a week. The matrices were saved in 30 text files, one for each energy bin, each one weighting 28 GB. In total, this adds up to 840 GB. If the finer resolution had been chosen, this would have taken even more time and more than 3TB of storage space.

The first new binning, referred to as binning J1, is a regular binning in longitude (at a given latitude, all the pixels have the same size in longitude) and decreasing binning in latitude from the poles to the galactic plane. Its pixels longitude size was inspired by the one in binning A but the Fermi Bubble fine pixels where dropped out because this structure is not specifically studied in this work. The galactic plane of binning J1 is composed of only one slice of pixels of 4° in latitude. Each pixel is 5° in longitude, except towards $l = 180°$ where one pixel has 7° and the other 8° in order to have a pixel approximately centered in zero to contain the CMZ. This binning did not produce any negative counts at all. However, having a plane of 4° in latitude is too much to have access to the interesting structures. The plane could have been split in two or four slices but a pixel centered in zero in longitude is also needed. Moreover, it is not possible with the Fermi software to have a pixel start at a non-integer latitude or longitude if the base binning is $1° \times 1°$. The best binning created, referred to as binning J2, has a plane of three slices of 2° in

longitude pixels and is highly inspired by binning J1. It only produced negative counts for the first energy bin. In total, -27 777 counts were distributed in 11 pixels, from -200 to -6162 counts per pixel. The amount of negative counts is only 0.12% of the amount of positive counts, here 15.9 million. Deconvolution results for E0 and E2 are shown in figure 3.13. The main characteristics of binning J1, J2 and all other binnings used in this work are presented in table 3.4 and an overview of binning J2 is given in appendix B.4.

As deconvolution in binning J2 created negative counts in the first energy bin, the latter should be removed from the fit, which means that in equation 3.1, i starts at 2 instead of 1. All the following analyses were performed in the binning J2 with E0 excluded unless mentioned otherwise. It has been verified on raw data that removing the first energy bin from the fit does not impact the general morphology of the components, which are the major physic results of this work. E0 does not significantly constrain the fit. Some plots are provided in figure 3.14.

3.3.3 Quality and limits

The negative counts issue and the changes in the deconvolution results produced by the merging of the plane pixel in binning A show the limits of the matrix deconvolution method, which seems to be highly impacted by the binning. In the following the stability of the binning J2 is tested. Then the convolution and deconvolution quality in this binning are evaluated.

Binning quality

In order to check the quality of the binning J2, one needs to see the impact of a slight change of the binning on the deconvolution and fit results and the divergences between the convolution in binning J2 and its base binning.

The binning J2 was shifted successively one degree up, down, left and right. This created four additional binnings, presented in table 3.4, in which data were also deconvolved. As for the binning J2, negative counts only occurred in the first energy bin for all the four new binnings. One can conclude that a slight change in the binning does not impact significantly the deconvolution results so that this binning is adapted for the deconvolution. Then the same fit was performed in each of these five binnings. As the pixels are not the same anymore, it is not meaningful to compare the spectra but one can compare the general morphology of the components. The latter does not appear to be impacted by a one-degree shift of the binning, which demonstrates that the binning J2 is adjusted for the fit.

Another essential thing to check is how different is the convolution in the base $1° \times 1°$ binning and in the binning J2. An overview of such a discrepancy between a rough and a fine binning was provided in part **Systematics from binning** of part 3.3.1: the convolution results are not the same in the two binnings. Even if the convolution results in the base binning are not exactly the same as the convolution of unbinned data by the LAT PSF, it is assumed here that they are both not so different. The convolution in the base binning is the closest approximation of the Fermi LAT convolution available. To gauge how convolution in J2 is different from the Fermi LAT convolution, it is relevant to compare some convolution results in J2 with some convolution results in the base binning rebinned to J2. The first is binned to J2 before convolution while the second is also binned to J2 but after convolution. For this test, a skymap not convolved with the PSF is required. The data collected by the LAT are always convolved so the *glliem* diffuse model from

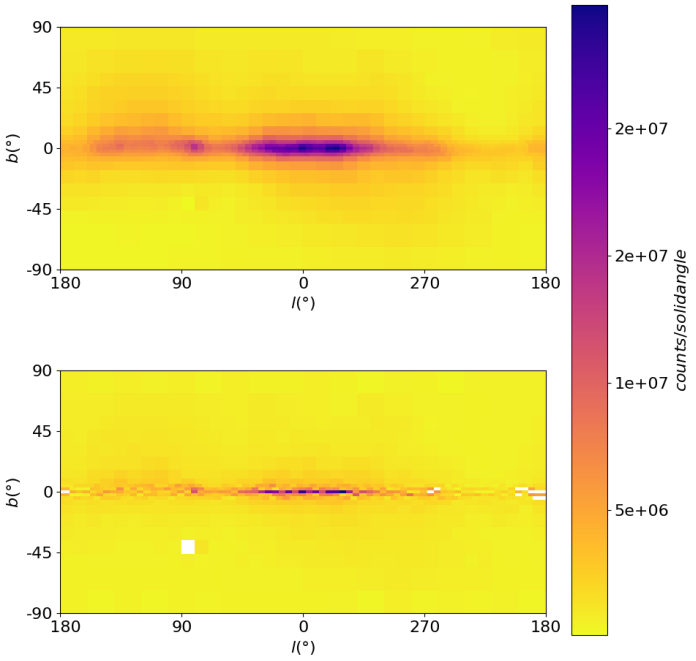

(a) E0

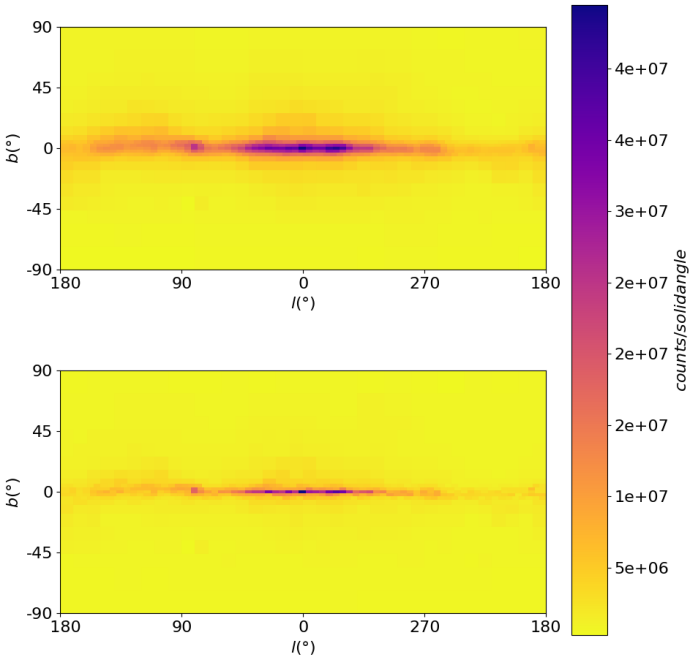

(b) E2

Figure 3.13: Data (a and b up) and deconvolution (a and b low) in the binning J2 for E0 and E2. Each uncolored pixel contains negative counts. The z axis is in units of $counts/sr$ for a readability purpose, but deconvolution is performed with counts.

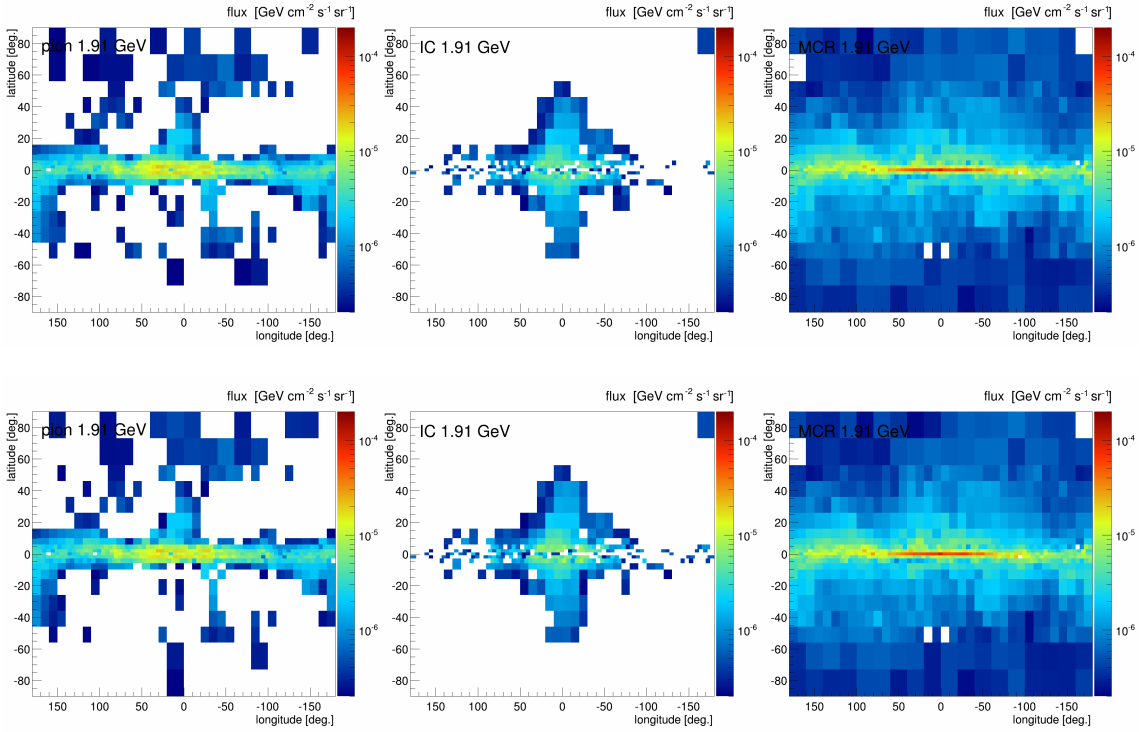

Figure 3.14: Morphology of the PCR (left), IC (middle) and MCR (right) components for a fit to convolved data with E0 included (top) and excluded (bottom).

Fermi [41] was used. It is a galactic interstellar diffuse emission model and it is therefore not convolved with the PSF and fairly resembles the real data. This last point is essential as the convolution results also depend on the data so the more the tested data look like the real data, the more reliable the results will be. The model was first convolved thanks to the $1° \times 1°$ convolution matrix and then rebinned to J2 and second, rebinned to J2 and then convolved thanks to the J2 convolution matrix. Both final models are binned in J2 and can therefore be compared. Figure 3.15 shows the absolute errors between the two convolved models at E0 and E11. The averaged relative errors are respectively 2.7% and 0.5%. One can notice that the largest errors occur towards the poles for $73 \leq |b| \leq 90$. At these latitudes the PSF is wide (see figure 3.7) leading to large uncertainties. These two pixels bands are far from the plane so one can assume that they do not impact the CGE and are not relevant for this work. If they are removed from the calculation, the average errors drop respectively to 0.72% and 0.33%.

The ideal test would be a similar test but using the deconvolution matrix instead of the convolution matrix. However, there is no deconvolution matrix in the $1° \times 1°$ binning. The inversion code crashed during the run because of memory issues. As the deconvolution matrix is simply the inverse of the convolution matrix, one can assume that the test would produce similar results. In conclusion, the binning J2 seems to be sufficient for the proposed studies and was adapted for this work. Now, the convolution and deconvolution quality in this binning need to be tested.

Convolution and deconvolution quality

In order to test the quality of the matrix method, a data set with no PSF included is needed so the Fermi diffuse model was once again used. Its convolved version can be obtained in two ways: first with the Fermi tools and second with the convolution matrix. The idea is

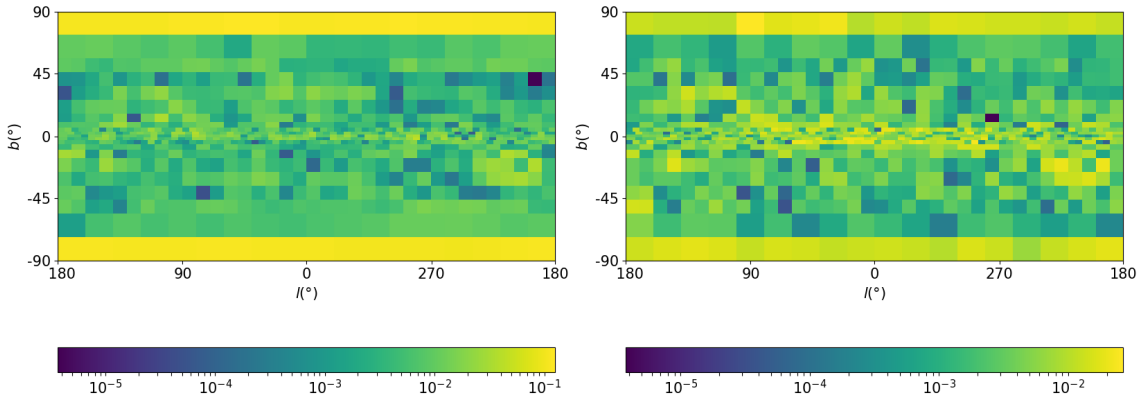

(a) 92.9 MeV (E1)

(b) 1.91 GeV (E11)

Figure 3.15: Relative error (abs(cr-rc)/cr) between the data that were convolved and then rebin (cr) and the data that were rebin and then convolved (rc) at different energies.

then to compare the outputs of the two methods to gauge the quality of the convolution matrix for each energy bin. This has to be done in a $1° \times 1°$ binning because the binning J2 (or any fit binning) cannot be implemented in the Fermi tools. The results of the test stay valid for the binning J2 because, as seen in the previous part, the agreement of the convolution in both binnings is better than 1% at all energies in the region of interest. Figure 3.16 shows the relative error between the two convolution methods at E1. One can see that the major problems occur at the borders. For $|b| \simeq 90°$, this could be the same effect as in figure 3.15: the PSF is so wide here that the uncertainties are large. However, for $l = 180°$ this effect remains puzzling.

Nonetheless, the agreement between the two convolution methods is good with an averaged relative error of 3.9% for the whole sky and of 0.92% if five degrees are dropped at each border (truncated sky). As expected, the agreement gets better with increasing energy: the errors are respectively 0.68% and 0.26% at E11 and drop down to 0.074% and 0.041% in the last energy bin. For more details, figure 3.16 in logarithmic scale is given in the appendix B.5.

Figure 3.17 shows the counts after the convolution of the *glliem* model with the Fermi tools and with the matrix as a function of longitude for many different fixed latitudes at E1. The same effect is visible as in the previous figure. In the galactic plane ($b = 0°$), the agreement between the two curves is good everywhere except towards $l = 180°$, where the Fermi tools-convolved model counts drop drastically. The mean relative error between these two curves is 1.9% and drops down to 0.96% if five degrees are dropped at each border. The drop at $l = 180°$ in the blue curves occurs for each latitude and on top of this effect, for $|b| \simeq 90°$, a discrepancy arises at all longitudes and the relative error jumps up to 81%.

A problem seems to occur at the map borders. However, this has no real impact for this work because the Fermi GeV excess occurs at lower latitudes and mostly toward the galactic center. Moreover for $l = 180°$ such a high drop in counts in the model convolved thanks to the Fermi tools does not seem physical and this indicates that the problem might come from the Fermi tools. True photons located close to the left (right) border are supposed to be reconstructed also close to the right (left) border as it is the same longitude ($l = 180°$)

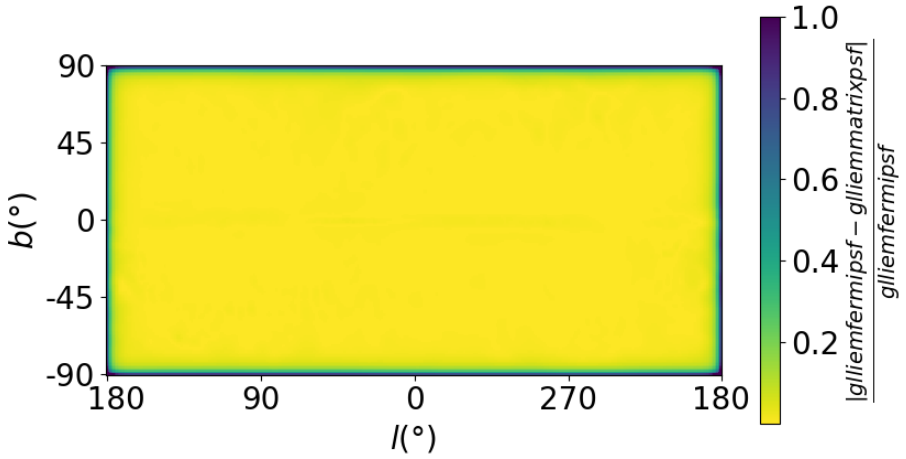

Figure 3.16: Relative error between the Fermi tools and the $1° \times 1°$ matrix convolution at E1 for the *glliem* model. The z axis is truncated at 1 for a readability purpose, the maximum value of the map is 2.29. The mean value of this skymap is 3.9% and 0.92% if the borders are dropped.

and this effect has been checked on point sources. Figure 3.18 provides an example of a point source centered at $l = 179.5°$, close to the left border of the map, whose counts spread to the right border once the PSF is applied. There is no drop in counts at $l = 180°$ with a test point source, and this was expected because the convolution matrices were created with help from such test point sources, and there is no drop in counts at the borders with the matrix convolution. The drop in counts was suspected to occur only when a complete skymap is given to the Fermi software and in order to demonstrate it, another test was made. The isotropic background map was convolved with the PSF in the Fermi software and the raw version was divided by the latter. As the background is isotropic, it should not be impacted by convolution, so the ratio between the two maps should be 1. However, the same border effect as in figure 3.16 was found. A plot of the ratio is provided in appendix B.6. This test knows nothing about the convolution matrix so the problem suspected indeed comes from the Fermi software. Back to figure 3.17, apart from the borders, the agreement is good and increases with energy: at E11, the mean relative error in the (truncated) disk is 0.78% (0.69%) and towards the poles is 26%. In the last bin, these values are respectively 0.074% (0.072%) and 0.69%.

Nonetheless, what needs to be tested above all is the quality of the deconvolution method. This can neither be done in a $1° \times 1°$ binning nor in a $0.5° \times 0.5°$ binning as there is no deconvolution matrix for them, so the test was this time performed in the binning J2. If the deconvolution is ideal, ideal data (with no PSF effect at all) and deconvolved data (convolved in the telescope and forward deconvolved) should be equal. The *glliem* model is rebinned into 861 pixels as required, once with no PSF (model A) and once after the PSF is applied with the Fermi tools in a $1° \times 1°$ binning (model B). Model B is then deconvolved using the deconvolution matrix (model C). Finally, model C is compared to model A via their relative error. The results for E1 are shown in the top part of figure 3.19.

As for the convolution, the major problems occur at the borders but for the rest of the map the agreement is good. Averaged over the entire sky, the relative error between the two maps is 5.6% but sinks to 4.4% if five degrees are dropped at the borders. At E11 these values respectively plunge down to 0.66% and 0.58% and finally in the last energy bin they reach 0.059% and 0.51%. All the relevant errors are written in table 3.5. One can

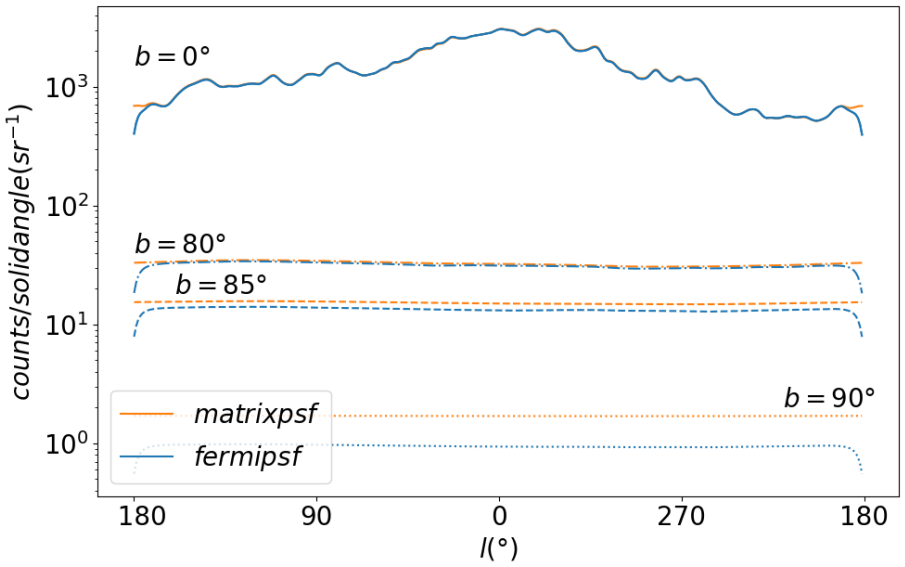

Figure 3.17: Counts after the convolution of the *glliem* model in the $1° \times 1°$ binning with the Fermi tools and with the matrix method as a function a longitude for many different fixed latitudes at E1. The relative error between the two top (respectively bottom) curves is 1.9% (respectively 81%).

notice that at low energies, the convolution is better than the deconvolution quality but at E11, both are equivalent. However, results are hardly comparable because the two tests were not performed in the same binning.

As seen earlier, there is an issue with the Fermi convolution at the map borders. The deconvolution quality test has been performed once using the Fermi tools convolution and once more using the convolution matrix to free the test from the border effects. This created a model D that can also be compared to model A and the results are provided in the bottom part of figure 3.19. The averaged relative errors are smaller: 3.7% for the whole sky and 3.1% without the borders. At about 2 GeV, these values reach respectively 0.56% and 0.51% and finally at they end up at 0.045% and 0.039% in the last energy bin.

Figure 3.20 shows the counts in model A and in model C as a function of longitude for many different fixed latitudes at E1. Once again, the agreement is good except towards the borders. In the galactic disk, the relative error between the two curves is 4.9% and 4.4% if the borders are removed from the calculation while at the poles, the total error is 17.5%. At 2 GeV these values become respectively 0.66%, 0.62% and 1.6% and in the last energy bin 0.081%, 0.081% and 0.16%. As usual increasing the energy reduces the errors.

	C (%)	D_F (%)	D_M (%)
Sky	$3.9 - 0.68$	$5.6 - 0.66$	3.7-0.56
WB	$0.92 - 0.26$	$4.4 - 0.58$	3.1-0.51

Table 3.5: Relative errors at E1-E11 on the convolution (C) and the deconvolution (D) matrices. Indices F and M refers to the "Fermi" and the "matrix" convolution. WB stands for "without borders" which means that 5° were dropped at each border.

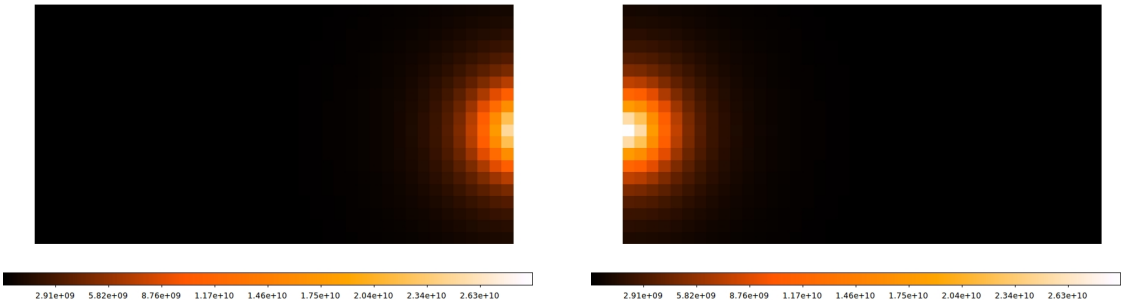

(a) (b)

Figure 3.18: A test point source located at $(l, b) = (179.5, -0.5)$ as it would be seen through the Fermi LAT at E0 for a sky binned in 1° square pixels. Figure b shows the skymap from $l = 140°$ to $l = 180°$ and between $b = \pm 10°$ so it is in fact on the left of the skymap. Figure a shows the skymap from from $l = 180°$ to $l = 240°$ and between $b = \pm 10°$ so it is in fact on the right of the skymap. The z axis is counts.

In conclusion, these tests show that neither the convolution nor the deconvolution are perfect but the errors calculated are small enough in the region of interest (see table 3.5). Moreover, the deconvolution test performed with the Fermi convolution provided a correction factor $cf = deconv/raw$ which is the ratio between the deconvolved model and the raw model in each pixel. Figure 3.21a shows this ratio as a function of energy bin number for four pixels: the CMZ, a halo pixel, a pole pixel and an anticenter pixel (located in the plane at around $l = 180°$). In the halo pixel, the correction factor is close to one from the beginning. The flux in this region in the *glliem* diffuse model and the data is rather isotropic so convolution and deconvolution do not have much impact. This is not only true for the LAT PSF but for all PSFs. The PSF embedded in the Fermi software is an estimate of the true PSF and might deviate from that true PSF. However, for regions of isotropic flux, like the halo, both PSFs will yield the same prediction. Therefore, it makes sense to have almost no correction. Although larger than in the halo pixel, the correction in the CMZ pixel is also small, with a mean value of 1.0178. In the pole and the anticenter pixels, the correction factor at low energies are far from one because of border effects. However, as they rapidly reach one thanks to the quick improvement of the PSF, their mean values are also close to 1 with respectively 0.9620 and 0.9652. This correction factor can be used as an estimate of the error made when deconvolving the Fermi data and be used to correct the deconvolved data. After deconvolution, counts in each pixel of the binning are divided by the corresponding correction factor. The fit can now be performed on the two data sets in order to see if the correction has a real impact on the fit results. Figure 3.21b shows the ratio between the two χ^2 skymap. Almost all pixels have values between 0.95 and 1.05 which means that there is no significant change brought by the correction factor. Thus, the correction is not used in the rest of the work.

Just like the correction factor, the errors calculated in this part are only estimates of the error made on convolution and deconvolution. To know this error and not only estimate it, one should realize the same tests with other models than *glliem*, and here lies the complexity. One needs a convolved map of the sky and its real version. The Fermi LAT cannot collect data without convolving them with its PSF and unconvolved models as *glliem* are not numerous and can only be convolved with the Fermi software which is the best approximation of the Fermi LAT convolution but is also not perfect as it has a border effect. The latter was detectable in the tests but further discrepancies perhaps remain.

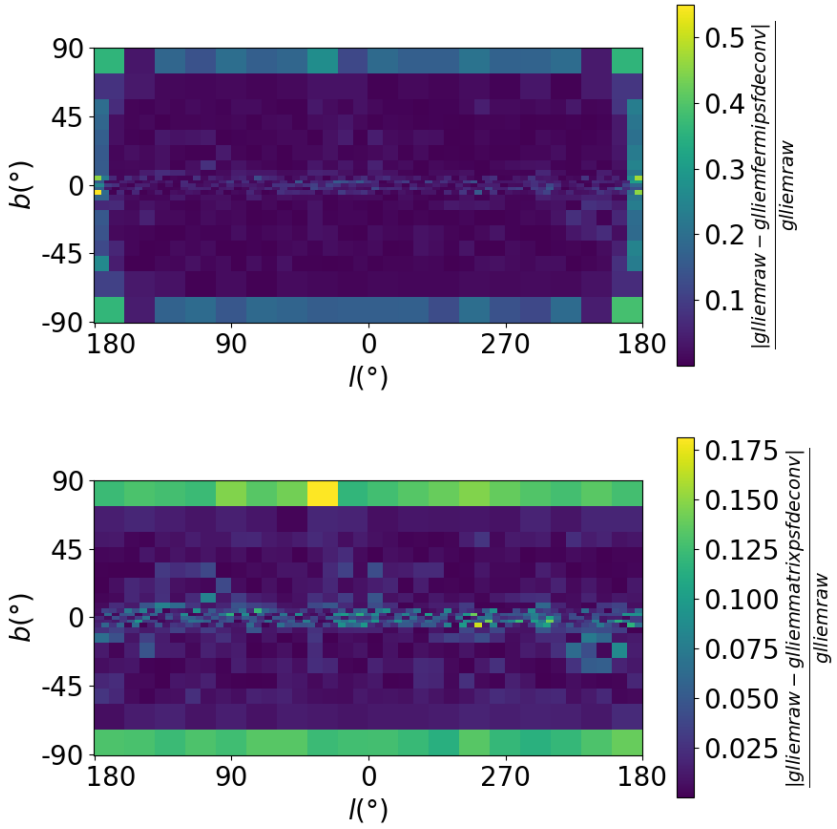

Figure 3.19: Relative error between the *glliem* model and the same model convolved then deconvolved at E1. The convolution was performed with the Fermi tools (top) and with the convolution matrix (bottom). Convolution was performed in a $1° \times 1°$ binning and deconvolution in the binning J2 for both figures. Please note the different scales on the z axes in the two plots.

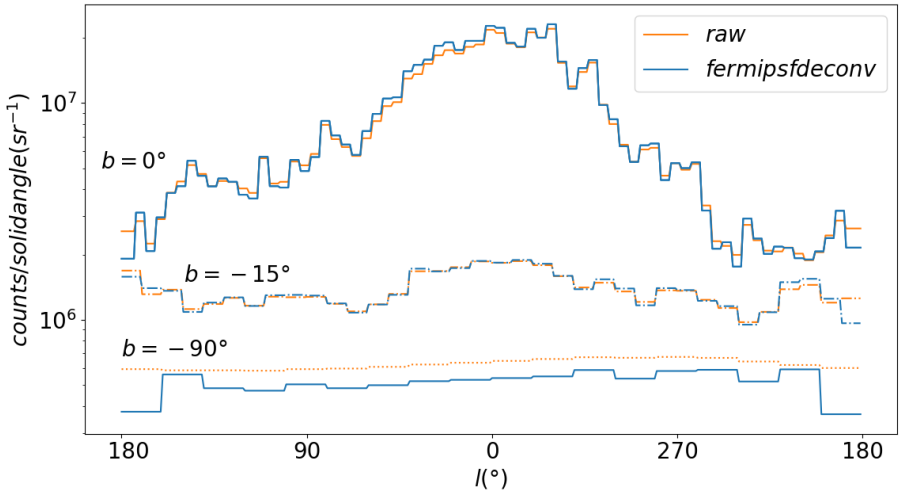

Figure 3.20: Counts in the raw model and after convolution with the Fermi tools followed by deconvolution with the matrix method in the J2 binning of the *glliem* model as a function a longitude for many different fixed latitudes at E1.

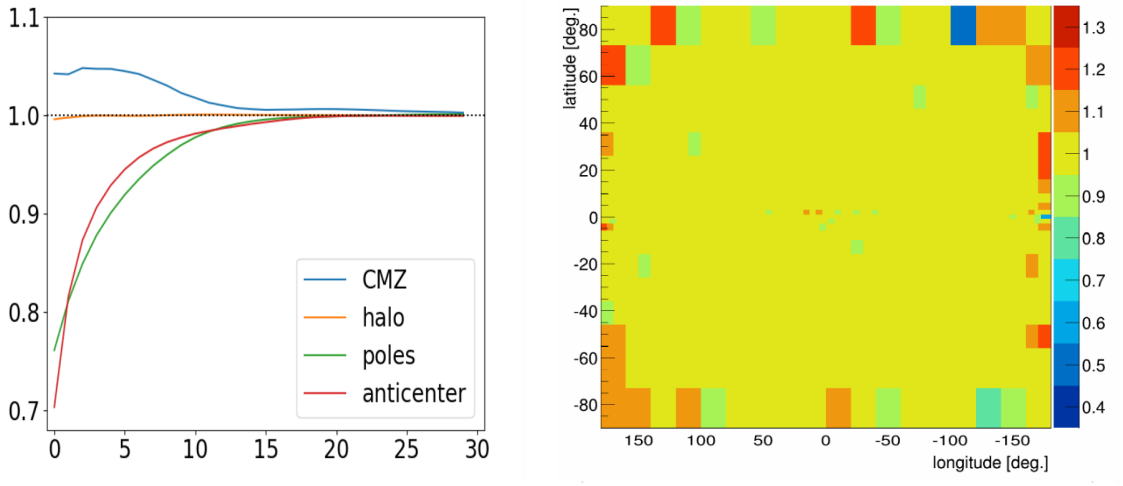

(a) (b)

Figure 3.21: Correction factor $cf = deconv/raw$ as a function of energy bin number for four different pixels (left), and ratio of the χ^2 skymap for a fit with correction over the one for a fit without correction (right).

3.3.4 Fitting data and deconvolved data

In previous works the convolved Fermi data were fitted with the templates presented earlier in this work, that do not include any LAT PSF effect as they come from theoretical hypothesis or from AMS data. This is not an inconsistency of the method if the PSF effect is assumed to be small enough to be neglected and therefore to have no impact on the results. Now that the PSF effect is known and removed from the data, one can perform a new fit to the deconvolved data with the same templates. The top of figure 3.22 illustrate this dual way of fitting. In the previous method, data are fitted and this creates a model A while in the new method, implemented in this work, data are first deconvolved and then fitted to create a model B. Both convolved and deconvolved data can be fitted with the same templates. A fit to convolved data is correct under some hypothesis and a fit to deconvolved data is always correct. It is essential to note that the templates cannot be convolved with the LAT PSF before the fit because the morphology of the components is required, which is retrieved only from the fit. For example, the PCR template is isotropic in shape over the entire sky. This shape is given to the fitting code which calculates the best intensity of this template in each pixel: this is the scaling factor C_j of equation 3.1. This creates the total (shape + intensity) morphology of the PCR component. A complete isotropic map convolved with the PSF would return the same isotropic map so it is completely meaningless (and wrong) to try to convolve the PCR template before the fit. Even if the shape of some other components such as IC is spatially dependent, the normalization of each component is not known before the fit and is crucial in the convolution process. All this is also true for deconvolution.

Applying or removing the PSF effect from the templates can be done after the fit. Model A and B can be deconvolved and convolved and this creates a model A' and a model B' respectively. This procedure is shown in the bottom of figure 3.22. Model A' does not include any PSF effect so it should be compared to deconvolved data. This can be done with the same χ^2 that helps fitting the templates, except that there is no fitting for this model. The same procedure can be done for model B' and convolved data. This dual way

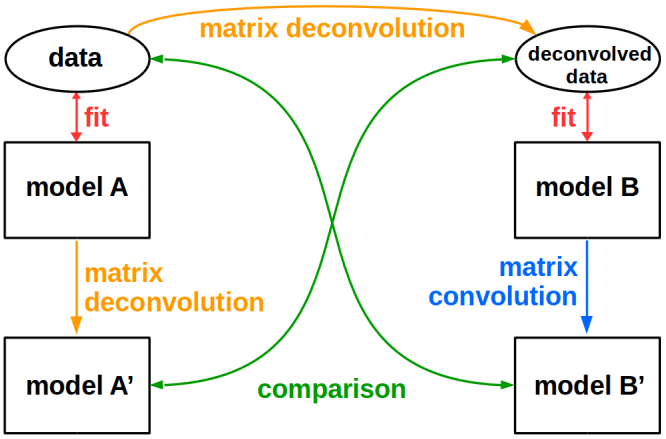

Figure 3.22: Schematic of the different models created and compared in this work. Model A is the kind of model created in previous works with a fit to the convolved Fermi data. Model A' is the deconvolved version of model A. Model B is a model created with a fit to deconvolved data. This model can be convolved to create model B'. Model A' and B' can be compared respectively to the deconvolved data and the data with help from a χ^2.

of fitting allows to observe the impact of the PSF on the fit results.

Figure 3.23a shows the results in the CMZ pixel of the binning J2 for a fit to deconvolved data (model B). The blue data points are the deconvolved data provided by the matrix method. The orange data points are the convolved Fermi data used in the literature. The templates were optimized for the blue deconvolved data points. The total model line, which is the sum of the isotropic, PCR, IC, BR, SCR and MCR templates matches well the data points and the χ^2 value is good with $\chi^2/dof = 0.383$. This plot also shows the effect of the PSF on the data as shown in figure 2.10c. As the CMZ is the brightest pixel, more counts leave the pixel than arrive in it once the PSF is applied. This means that the deconvolved flux should be greater than the raw flux, and this is what the figure shows. Moreover, one can see that as the energy increases, the difference between the deconvolved flux and the raw flux disappear, confirming that the PSF gets better with the energy and that C_e resembles the identity matrix in the highest energy bins.

Figure 3.23b shows the same spectrum but forward convolved (model B'). Once the fit is done for every pixel, a skymap of each process at each energy bin can be created and convolved thanks to the matrix method. Then, new spectra can be created in each pixel. Convolution and deconvolution are global processes and they cannot be applied to a single pixel. As only results for the CMZ pixel are presented here, it is important to have this in mind. In this plot, the total line now matches the convolved Fermi data points (orange dots). This is an important cross-check. It means that the entire method is self-consistent: an excellent fit to deconvolved data, which is then convolved, describes the convolved data excellently. The result is shown here for the CMZ pixel, but it was checked that it holds for a huge majority of pixels. The χ^2 value shown in figure 3.23b is calculated from a comparison of the convolved spectra to the Fermi data. No additional minimization was performed. The reduced χ^2/dof obtained this way is 0.375. It should be noted that E0 was dropped both from the fit and the χ^2 evaluation for consistency. The break positions and index are the same in figures 3.23a and 3.23b as they correspond to the one fit that was performed to obtain model B. The forward convolution of the results allows to see

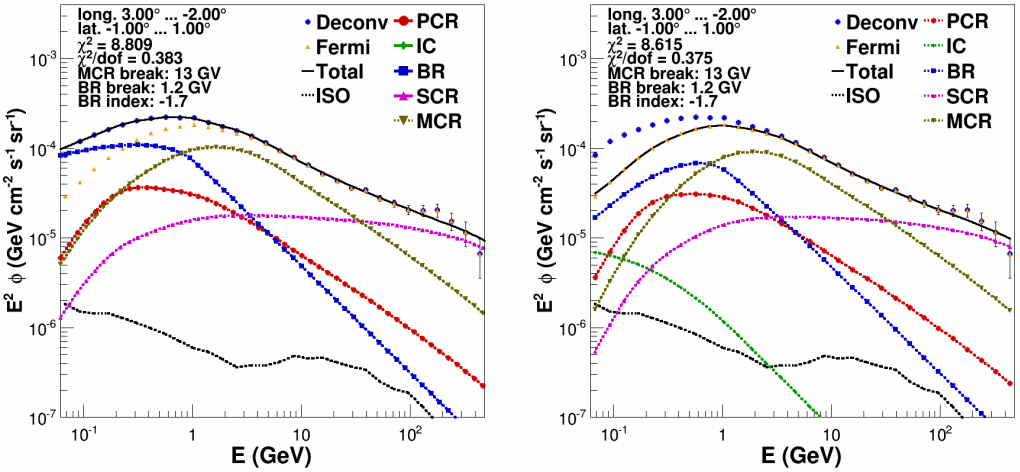

(a) (b)

Figure 3.23: CMZ spectrum for the fit to deconvolved data in binning J2 (left). The spectrum on the right-hand side is not a fit to convolved Fermi data but the forward convolution of the spectrum on the left-hand side. Orange dots are convolved Fermi data, as used in the literature, and blue dots are deconvolved data, provided by the deconvolution implemented in this work.

how each component separately would be seen through the LAT. One can notice that the isotropic template keeps the same shape before and after convolution, which is expected for an isotropic flux (in shape and scaling) and demonstrates that the matrix method works properly. The impact of the convolution can be observed in the form of a depletion at low energies for all other spectra. It should be noted that the IC component, which was too low to be visible on the scale in figure 3.23a, shows up at a visible level after convolution in figure 3.23b. This is due to fluctuations in the fitted IC skymap. During convolution pixels with a stronger IC component leak into pixels with a weaker IC component, thus smoothening the IC skymap.

A similar test can be made for a fit to raw data (model A) with forward deconvolution (model A'). The results are presented in figure 3.24. The fitted spectrum shows good results with $\chi^2/dof = 0.373$. For this fit, the first energy bin was included. As there is no deconvolution in play at this point, there is no reason to remove E0 from the fit. One should always use as much data as possible. However, in the χ^2 calculation after deconvolution, this bin is excluded, because deconvolution is known to be unstable at this energy. Figure 3.24b shows the deconvolved spectrum obtained from the fit to raw data. Here, only the total line is shown (black line). The separate deconvolved components show large fluctuations, as can be seen from appendix B.7. This is due to the fact that the fit to convolved data does not return a smooth distribution of the separate components. These fluctuations are expected, as some templates are very similar in certain energy ranges and may be interchanged by the fit, leading to fluctuations on small scales, but still a robust prediction of the general morphology of a skymap. During deconvolution, however, these fluctuations are boosted. The deconvolution will move counts from regions of low intensity to regions of higher intensity, thus increasing the level of fluctuations in a skymap. The resulting skymap and the resulting spectra cannot be considered to be a physical prediction, but are instead scaled-up fluctuations from the original fit to the raw data. The templates corresponding to the total deconvolved flux shown in figure

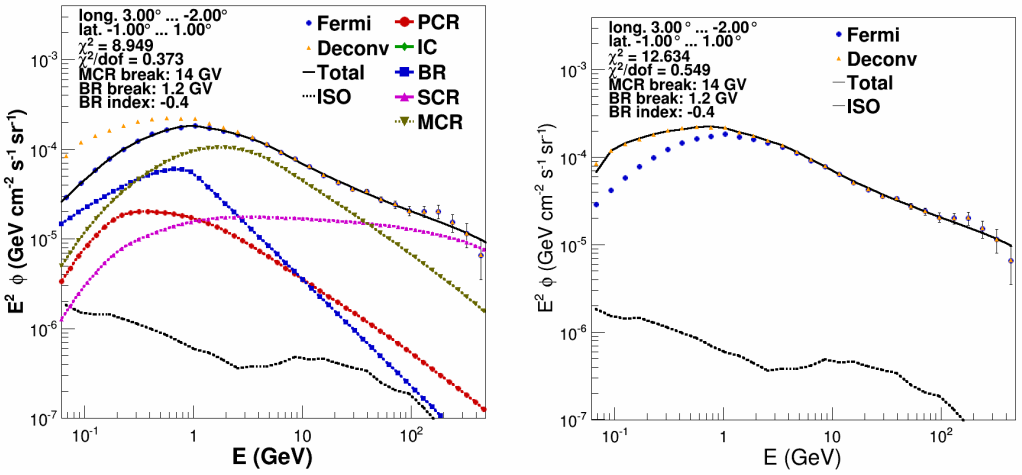

Figure 3.24: CMZ spectrum (left) and CMZ forward deconvolved spectrum (right) for the fit to the data in binning J2.

3.24b can be found in appendix B.8. The total skymap returned from the fit to raw data will not include such fluctuations. It describes the data well, and therefore its morphology will resemble the morphology of the data. This total skymap can be deconvolved and the resulting spectrum is shown in figure 3.24b for the CMZ. Except for the first energy bin (which is known to be not a robust prediction), the deconvolved data are well-described. The χ^2/dof calculated from E1 to E29 is 0.549. The χ^2 skymaps for forward deconvolution (model A') and forward convolution (model B') are provided in appendix B.9.

In this chapter a novel method to deconvolve the Fermi data was described and tested. Systematics of the method were discussed and the deconvolution was applied to the Fermi data. It was found that the method is self-consistent, in that a model prediction derived from a fit to the deconvolved data is consistent with the convolved data and vice-versa. It was found that the impact of deconvolution is non-neglible at low energies. Earlier it was discussed that the convolution of the model components is not feasible in a fit using energy templates. Instead, the data either need to be deconvolved or the model needs to be fitted to convolved data and the deconvolved to retrieve the physics information on the true distribution of the components and their true template shape. It was found in this chapter that the latter is impossible due to the boosting of fluctuations in the fit in the process of deconvolution. In the following the deconvolved Fermi will therefore be used for the fit. Besides being the only possible approach, this approach is also the most physical way to approach the problem: the spectral templates used in the fit are derived from the AMS-02 data, which do not know about the Fermi detector. It is therefore more meaningful to fit these templates to the deconvolved data, than to convolved data. In the following the GeV excess is studied in deconvolved Fermi data. The most important question that arise are: is the excess present or as significant as in convolved data? Is the spatial and spectral morphology of the signal similar to what was derived from convolved data? The answer is yes. Details are discussed in chapter 4.

4 Results

This chapter presents the results of this work. Part 4.1 demonstrates the need of the MCR component in the deconvolved data. Part 4.2 compares old and new results and methods and discusses the origin of the MCR template.

4.1 Need of an MCR component with deconvolved data

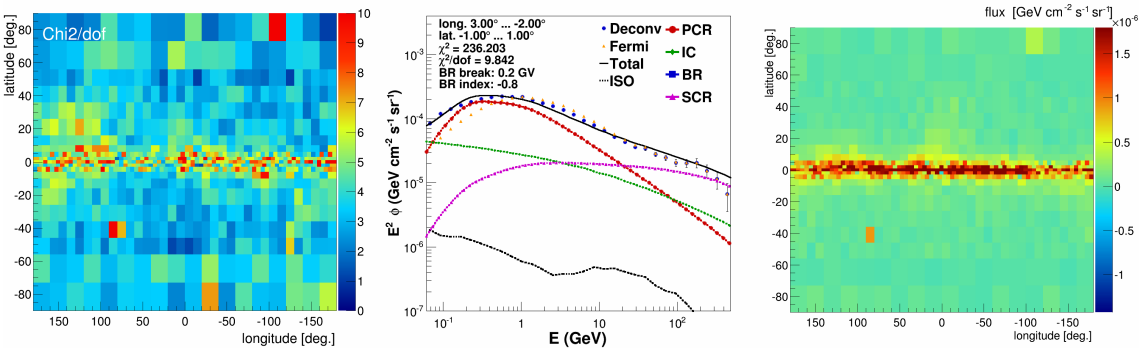

(a) (b) (c)

Figure 4.1: Reduced χ^2 skymap (left), CMZ spectrum (middle) and data minus fitted flux at E8 (right) for a fit to deconvolved data with only four components: PCR, IC, BR and SCR.

In fits to Fermi convolved data, the need of an MCR component was clear. Otherwise, the data and model spectra could not peak at the same energy (see figure 3.3). With deconvolved data one can legitimately ask the question: do the data still require an additional MCR template or did the PSF mimic a false signal? To answer this question, a fit to deconvolved data was performed with only four templates: PCR, IC, BR and SCR. The SCR template is also an additional component to the three conventional processes. However, the SCR template mostly takes care of the hard energy tail of the spectrum which is almost not impacted by the LAT PSF. If the SCR template is required in fits to Fermi convolved data, it will also be needed in fits to deconvolved data. Figure 4.1a shows the reduced χ^2 skymap for the fit with only four templates. The highest χ^2/dof

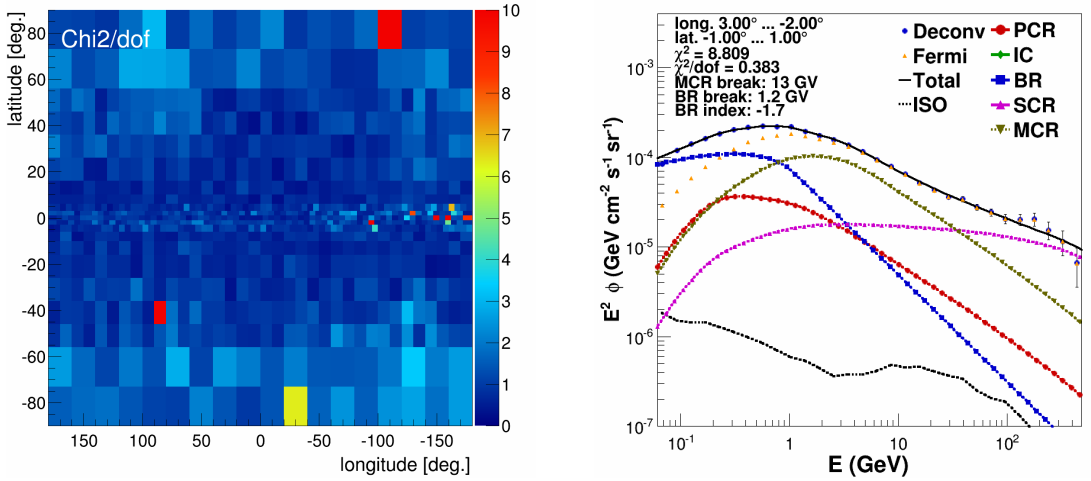

(a) (b)

Figure 4.2: Reduced χ^2 skymap (left) and CMZ spectrum (right) for a fit to deconvolved data with five components: PCR, IC, BR, SCR and MCR.

are located close to the galactic plane, between $b = -6°$ and $b = 6°$ and almost all values are larger than 2. The galactic plane is a region rich in MCs, but the latter also cross the line of sight of each sky pixel as the Earth sits in the galactic disc. This can explain why the reduced χ^2 are high in all the sky and especially at low latitudes. In the CMZ spectrum, shown in figure 4.1b, one can see that the deconvolved data spectrum peaks around E8 while the model peaks at E5 due to the PCR component. At high energies, SCR is dominant and the model flux is larger than the data flux, probably because of the PCR scaling factor. The latter needs to be large enough to fit at best the low energy points, but this causes an excess of the model at high energies. Finally, figure 4.1c shows the excess (data minus fitted flux) at E8. In the galactic plane, between $b = -3°$ and $b = 3°$, the data flux is mostly larger than the model flux. This is a clear demonstration of the Fermi GeV excess. Unlike fits with spatial templates, the excess retrieved here does not have spherical distribution around the galactic center. Otherwise it could be a hint in favor of the DM hypothesis because of the also spherical distribution of the NFW profile (see part 2.1). On the contrary, the excess distribution retrieved from a spectral fit follows the galactic plane at first sight. Outside the disc, the data flux is about 10 times (or more) lower than in the disc which make is hard to see the missing flux from this plot.

All this leads to the following conclusion: an additional component is also needed for deconvolved data. A new fit with MCR included was therefore performed. The reduced χ^2 skymap is shown in figure 4.2a. It has eight pixels with values larger than 7. Two are located at the poles which is far from the region of interest, two close to regions where counts were over subtracted in the point source subtraction process and one at about $l = -150°$ in the galactic plane. Apart from these few pixels, the χ^2 skymap is rather flat and the χ^2/dof values are low. With four templates, the fit is able to well reproduce the data. In conclusion, not only an additional component is needed for deconvolved data, but also its spectral shape can be the one chosen for MCR and presented in part 3.2. Figure 4.2b shows the CMZ spectrum. One can see that the PCR scaling factor or the PCR intensity is yet less important than in figure 4.1b. The model flux at high energies is therefore less high than with only four templates. The introduction of the MCR component reduces the constraints on the PCR template and makes the reduced χ^2 drop from almost 10 to 0.383. One can notice that

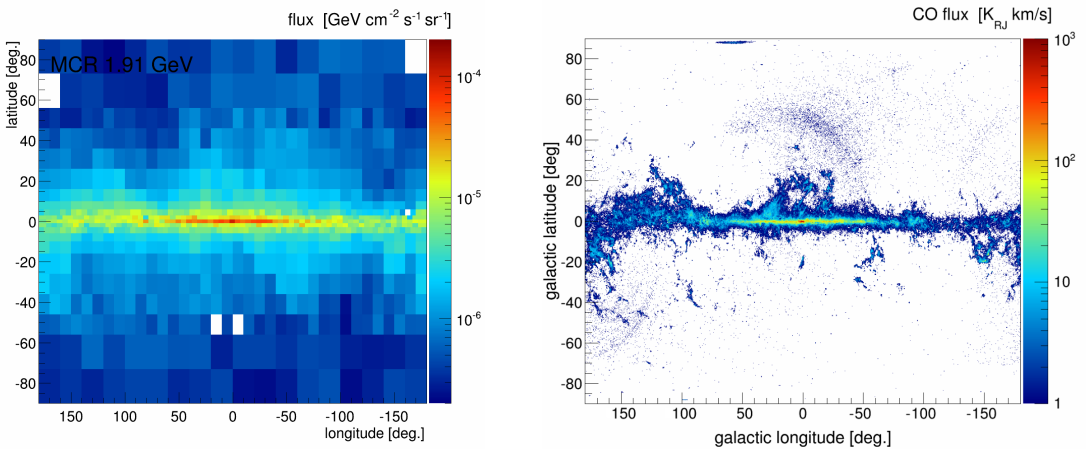

(a) (b)

Figure 4.3: MCR flux skymap at E11 (left) for a fit to deconvolved data including five templates and CO rotation line (right) as measured by the Planck satellite [42].

there is no IC flux in the spectrum, which is rather unexpected. This component was found to be quite unstable in the analyses and further details about it are provided in the following.

As for the MCR spatial shape retrieved from the fit (its flux skymap), it is correlated with the CO distribution, which is a tracer of molecular clouds. As their name indicates, MCs are mostly made of molecules, the most abundant one being molecular hydrogen H_2. However, this molecule is hard to detect so the second most abundant molecule, carbon monoxide CO, is used as a tracer of H_2. The relative abundance of CO compared to H_2 is 10^{-5}. CO has a rotational transition that emits at 230 GHz, in the radio range, that can be detected by radio telescopes. The CO[1] and MCR fluxes are shown in figure 4.3. Both fluxes are high in the galactic center and the galactic plane and some additional structures are visible in the halo with the naked eye. Furthermore, on figure 4.3b, the CMZ is clearly visible: it is the red spot located around $(l, b) = (0, 0)$. As previously said, this region is extremely rich in MCs and presents one of the highest excess.

A graphical way of showing the correlation between the MCR and the CO fluxes is with a scatter plot. In figure 4.4a, the x axis is the CO flux and the y axis is the MCR flux at E11. Each red point corresponds to a pixel of binning J2. The same figure in linear scale is provided in appendix C.1. One can easily see a privileged tendency, which indicates a correlation between the two fluxes. From a mathematical point of view, Pearson's correlation coefficient $\rho_{X,Y}$ measures the linear correlation between a pair of random variables (X, Y)[2]. It has a value between -1 and 1. $\rho_{X,Y} = -1$ or 1 means that it is possible to find a straight line that passes through all the points. In the first case, one variable decreases as the other increases and in the latter, both increase together. $\rho_{X,Y} = 0$ means that the variables are not linearly correlated and that there is no privileged direction in the scatterplot. If one performs a linear regression and if ϵ_i is the distance between the fitted straight line and the data point i, then the larger the ϵ_is, the closer to 0 $\rho_{X,Y}$ will be. The formula for $\rho_{X,Y}$ is:

[1]The CO flux units include K_{RJ} or Kelvin Rayleigh-Jeans, which is a unit of brightness temperature.
[2]The scatterplots are sometimes plotted in logarithmic scale for readability purposes but Pearson's coefficient really evaluates a linear correlation.

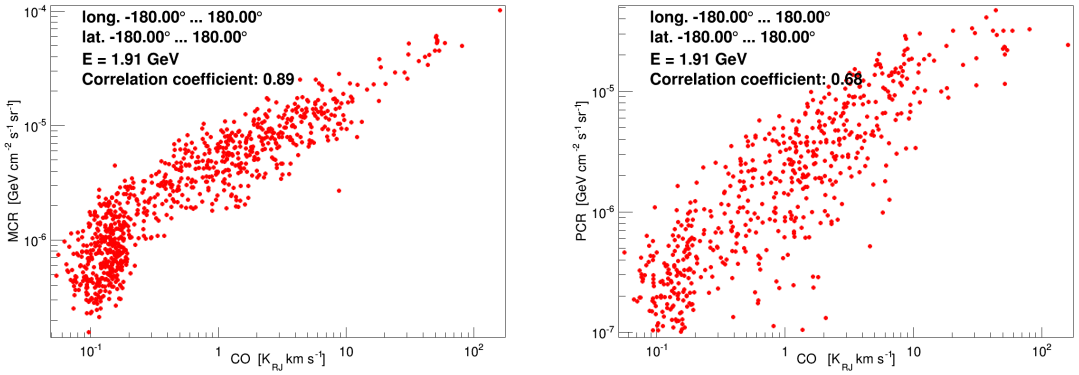

(a) (b)

Figure 4.4: Scatterplot of CO flux versus MCR flux (left) and scatterplot of CO flux versus PCR flux (right), in logarithmic scale for a readability purpose.

$$\rho_{X,Y} = \frac{cov(X,Y)}{\sigma_X \sigma_Y} \tag{4.1}$$

where *cov* is the covariance and σ the standard deviation. As the covariance is symmetric, $\rho_{X,Y} = \rho_{Y,X}$. This correlation neither reflects the slope of the eventual straight line that could fit the points nor nonlinear relationship but only the existence of a privileged direction in the scatterplot and its strength. Here, the correlation coefficient is $\rho_{CO,MCR} = 0.89$, which means that the CO and MCR fluxes are indeed highly correlated and that they increase together towards regions with high MC density. In the galactic plane, for $|b| < 1°$, this correlation is even stronger with $\rho_{CO,MCR} = 0.94$.

Another important correlation to check is the correlation between the PCR flux and the CO flux. It should not be larger than the CO-MCR correlation. Otherwise this would mean that the PCR template is more strongly linked to molecular clouds than the MCR template is and therefore, that the molecular clouds hypothesis is wrong: the CR proton spectrum could still be modified in some regions of the galaxy but not because of molecular clouds. Figure 4.4b shows the scatterplot for CO versus PCR for a fit to deconvolved data in binning J2. The same plot in linear scale is provided in appendix C.1. The correlation between the two fluxes is $\rho_{CO,PCR} = 0.68$, which means that there is a correlation between them but less strong than the one between CO and MCR. As the two fluxes comes from the same galaxy, it is normal that they are correlated. Most of the emissions come from the galactic plane so there is a high probability for two fluxes to at least be slightly correlated. The conclusion is the following: in order to be able to reproduced deconvolved data, the fit needs an additional template on top of PCR, IC, BR and SCR, and this template can be MCR, which morphology is correlated to the molecular clouds distribution.

Further results, spectra and flux skymaps of the five components (retrieved from the fit and convolved), are provided in figure 4.5 and 4.6. On the spectra, one can see that the PSF effect on the data is stronger close to galactic center (top row) than is other sky pixels. When the PSF seems to have no impact on the data, its effect is sometimes more visible on the templates. This is the case in a pixel located at the anticenter (middle row): there is no IC flux in the fitted model but there is some in the convolved model. This new flux comes from neighboring pixels that had IC flux before convolution, which was smeared out during

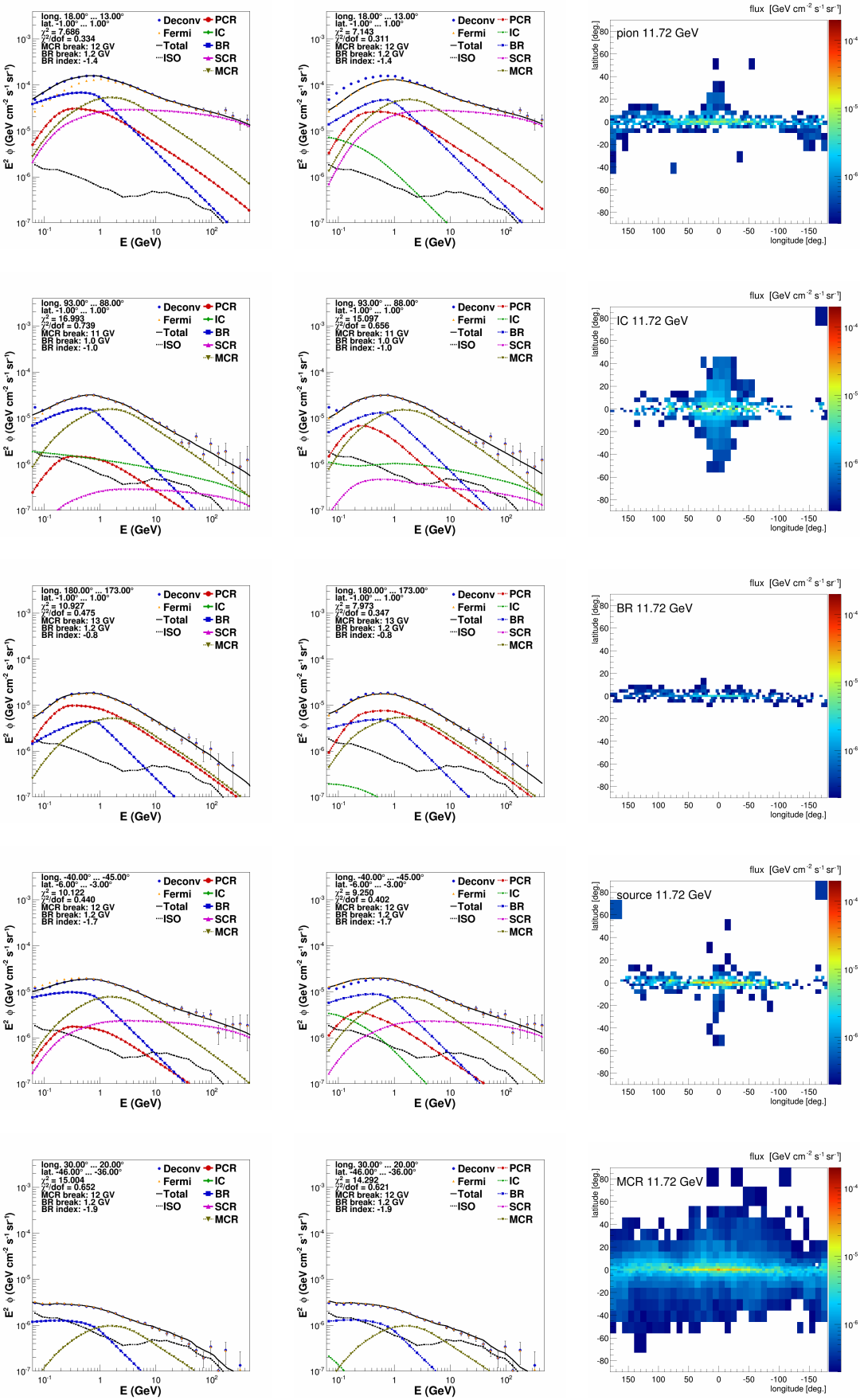

Figure 4.5: Spectra for a fit to deconvolved data (left) and corresponding forward convolved spectra that model convolved data (middle) for five pixels and skymap fluxes of PCR, IC, BR, SCR and MCR (top to bottom) at E17 (right) for a fit to deconvolved data.

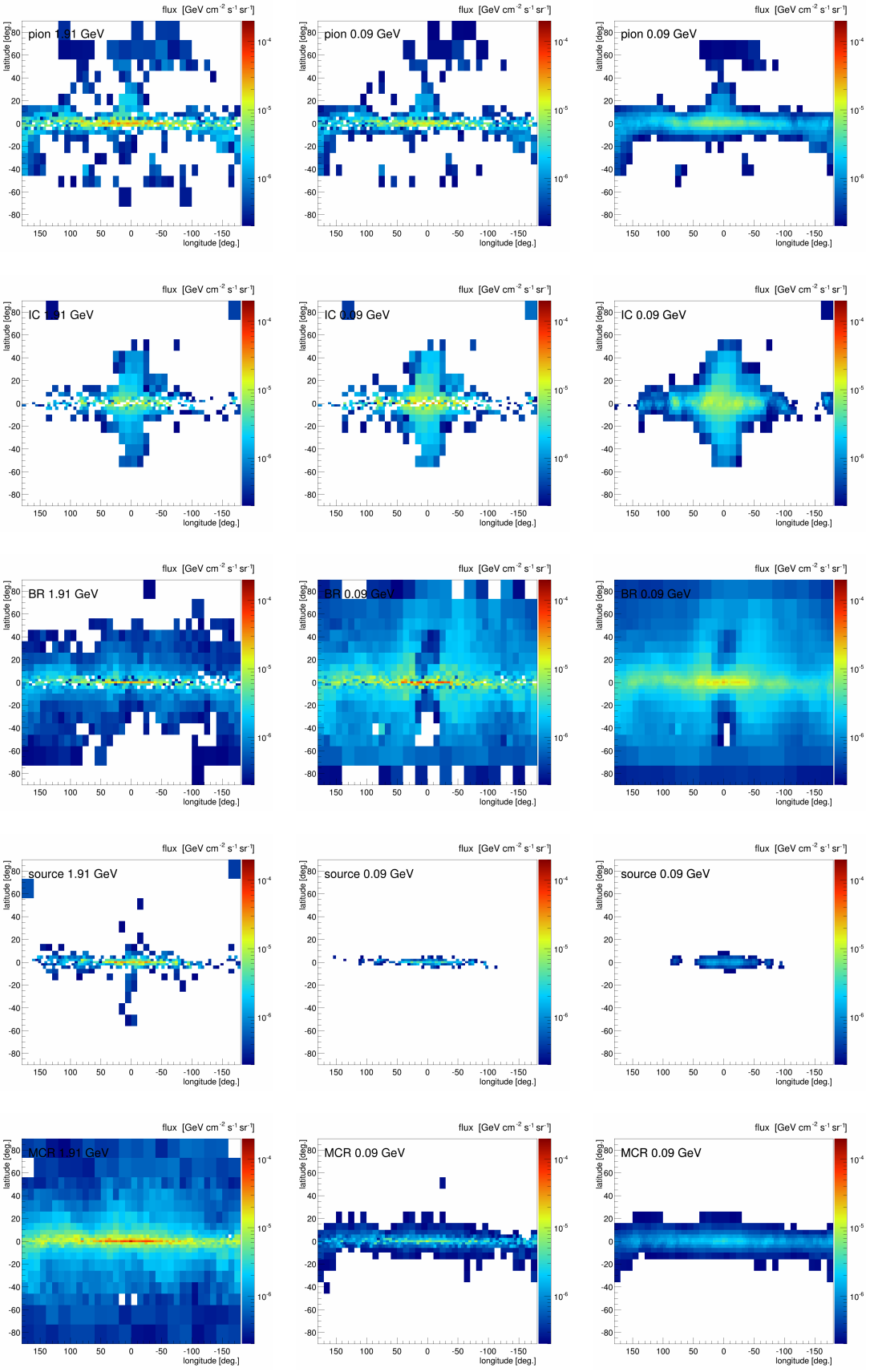

Figure 4.6: Skymap fluxes of PCR, IC, BR, SCR and MCR (top to bottom) at E11 (left), E1 (middle) and corresponding forward convolved at E1 (right) for a fit to deconvolved data.

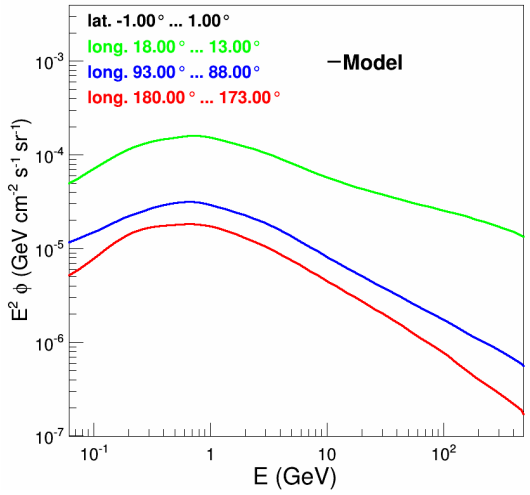

Figure 4.7: Illustration of the hardening of the model towards the galactic center. The decomposition of the three models can be found in the first three rows of figure 4.5.

convolution. This flux smearing can be observed in figure 4.6 middle and right. The first is the skymap retrieved from the fit at E1 and the latter is the convolved version, the same flux as it would be seen through the LAT. Some comments can be made on the component morphology. PCR, BR and MCR fluxes are particularly strong in the galactic plane. The IC and the SCR fluxes, which both have a hard energy tails, are rather concentrated around the galactic center and in the Fermi bubbles. One can notice that there is a lack of IC flux in the galactic plane, which does not seem physical. This component was found to be highly unstable in the analyses. This might be caused by an overestimation of the Fermi systematic errors. A test was performed and details are provided in part 4.2.2. Back to the spectra, one can notice a hardening of the model and the data in the galactic plane towards the galactic center. Figure 4.7 shows this hardening by plotting the models from the three to rows of figure 4.5 on top of each other. This hardening reflects the increasing contribution of SCR from the anticenter to the galactic center and the transition between gamma rays from propagated to freshly accelerated protons. Finally, some spectra including the error bars from the Minuit minimization are provided in appendix C.2.

Finally, the whole sky can be fitted as one pixel and results are shown in figure 4.8a. The fit is good, especially compared to figure 3.3a but there is no IC contribution visible. However, this fit is only a rough approximation of the reality and a more relevant all-sky fit is for example an average of the 861 spectra retrieved from the fit in binning J2, as shown in figure 4.8b. The χ^2 provided here is not minimized and is only used as a quality index. In this averaged spectrum, IC is now present. At about 1 GeV, the BR, MCR and PCR fluxes are more or less equivalent, larger than the isotropic background flux while the IC and SCR fluxes are below. In figures 4.8a and 4.8b, data and deconvolved data are exactly equal which is indeed expected for the whole sky. Convolution and deconvolution conserve the total amount of counts so the total amount of flux also.

4.2 Discussion

4.2.1 Comparison to previous results

Previous works [17], using Fermi convolved data in binning A, already showed that the gamma ray sky is well reproduced if an MCR and an SCR template are included in the fit.

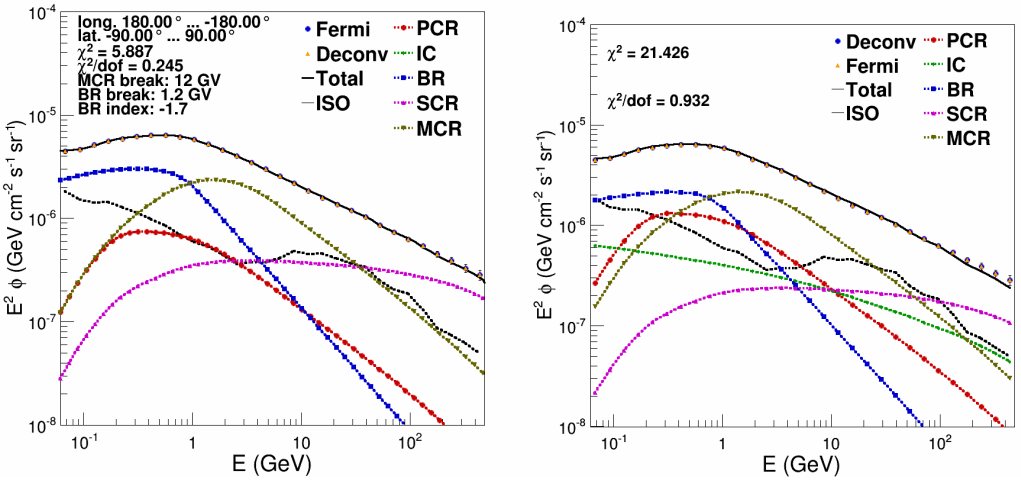

(a) (b)

Figure 4.8: Fit results for the whole sky considered as one pixel (left) and averaged spectrum of the 861 pixels of binning J2 for a fit to deconvolved data (right).

However, the fit was performed on convolved data. This exact same fit has been reproduced with the larger data set used in this work and the reduced χ^2 skymap is shown in figure 4.9a. As convolved data are fitted, all the energy bins are included. The DM hypothesis was also tested in [17] and provided acceptable results but the MC hypothesis was preferred because the fits were significantly better and the morphology of the MCR component, shown in figure 4.9b, follows the morphology of the CO component, shown in figure 4.3b. The scatterplot in figure 4.9c provides a mathematical vision of this correlation. The correlation factor between the two fluxes is 0.83. The same plot in linear scale is shown in appendix C.1. Another aim of this work was to check, once the need of an MCR component is established, the impact of the PSF on the CO-MCR correlation. In both cases, with Fermi data or deconvolved data, the two fluxes are correlated, but it is hard to draw a conclusion as the two fits were not performed in the same binning. Here, $\rho_{CO,MCR} = 0.83$ for Fermi data in binning A and $\rho_{CO,MCR} = 0.89$ for deconvolved data in binning J2. One could conclude that the correlation is slightly stronger with deconvolved data, but this could be a binning effect. For a relevant comparison, the old fit was performed in binning J2. This provided a correlation factor $\rho_{CO,MCR} = 0.92$. The corresponding scatterplot is shown in appendix C.1. This leads to two conclusions. First, there is no significative improvement or decline of the correlation between convolved and deconvolved data and second, the correlation factor is binning dependent. The correlation between CO and MCR seems to be more visible in binning J2 than in binning A. It is important to remember that it is not possible to fake a correlation, on the contrary it is only possible to hide the correlation.

Previous works also showed that the SCR morphology, retrieved from the fit, is correlated with the ^{26}Al flux. Such a correlation was expected because, as explained in part 2.2.1, the ^{26}Al flux is a tracer of magnesium rich cosmic ray sources and SCR gamma rays are created by π^0 decay in the vicinity of these same sources. This correlation holds with deconvolved data. The vertical arrows in figure 4.10 emphasizes the correlation between the ^{26}Al and the SCR fluxes. One can notice a strong contribution in the galactic bar and a lack of flux in the opposite direction. This increase of flux towards the galactic center was already observed with the hardening of the spectrum in figure 4.7. The SCR flux in the Fermi Bubbles is thought to come from point sources providing advective outflows of gas in the Galactic center, not from point sources directly present in the Bubbles. That is why these

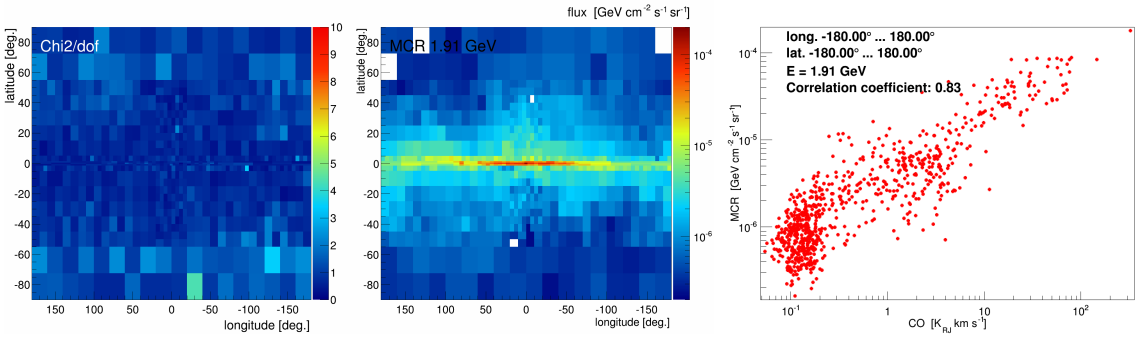

(a) (b) (c)

Figure 4.9: Reduced χ^2 skymap (left), flux skymap of the MCR component at E11 (middle) and scatterplot of CO flux versus MCR flux in the galactic plane for a fit to convolved data in binning A, with E0 included. The axes of the scatterplot are plotted in logarithmic scale for a readability purpose.

two structures are not observed in the ^{26}Al flux. And for this reason also, it is hard see the correlation between the two fluxes with a scatterplot. The ^{26}Al flux traces only cosmic ray sources that are magnesium rich and the SCR flux traces all cosmic ray sources and the Fermi Bubbles. In the galactic plane, for $|b| \leq 1°$, $\rho_{Al,SCR} = 0.61$, which indicates a slight correlation between the two fluxes. However, $\rho_{Al,PCR} = 0.61$. It was therefore decided to remove two points from the scatterplot that looked out of range for both PCR and SCR. The two correlation factors jumped to $\rho_{Al,SCR} = 0.80$ and $\rho_{Al,PCR} = 0.68$. The scatterplots are provided in appendix C.1. Although less strong than the CO-MCR correlation, the correlation between ^{26}Al and SCR truly exists.

4.2.2 Overestimation of the systematic errors

One can see in figure 4.5 that the χ^2/dof values are around 0.5. When the reduced χ^2 is below 1, it might be an indication that the errors where overestimated. One might suspect that the systematic errors provided by the Fermi collaboration are over estimated. In principle, one might test this by applying a scaling factor to the systematic errors, such that χ^2/dof values close to one are obtained. However, the energy dependence of such a scaling factor is *a priori* unknown. For his reason, a test with an energy independent scaling factor was performed. With a factor of 0.5, a χ^2/dof close to 1 was obtained. Despite generally yielding similar fit results as compared with the case with no scaling, some minor deviations were observed in the IC skymap. These deviations are probably due to the assumption of an energy independent scaling factor, which changed the χ^2 distribution in parameter space. Since the true energy dependence of the scaling factor is unknown, no scaling of the systematic errors was applied in the analysis and keep in mind that the reduced χ^2 values quoted here probably underestimate the true χ^2 values due to an unknown over estimation of the Fermi systematic errors.

Furthermore, some additional sources of errors were not included in the fit. The templates created by GAMMASKY have an uncertainty and deconvolution is not ideal. This latter point is further discussed in part 4.2.4.

4.2.3 Interpretation of the MCR template

The molecular clouds template was given this name because of its correlation with CO, which is a tracer of MCs. However, this does not necessarily mean that the proton spectrum

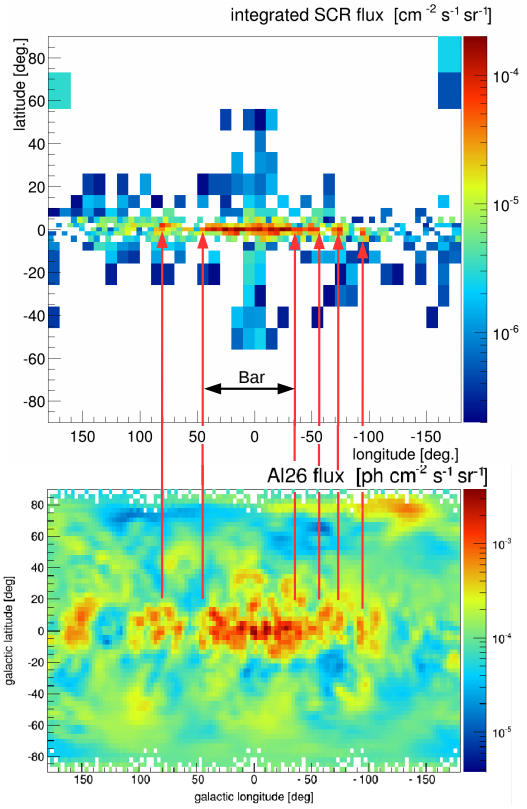

Figure 4.10: SCR flux integrated over all energy bins (top) and ^{26}Al flux (bottom) traced by the 1089 keV gamma line studied by the Integral/Spi satellite [43]. The longitude distributions of the fluxes are correlated, as indicated by the vertical arrows. This correlation is expected as both fluxes are tracers of magnesium rich cosmic ray sources. The SCR flux also traces the Fermi Bubbles whereas the ^{26}Al flux does not.

is modified by molecular clouds themselves. It could be anything that is correlated to CO. For example, MCs are the only regions in the galaxy where stars form. The modification of the proton cosmic ray spectrum could be caused by the stars, by unresolved point sources located in MCs. But if protons are really depleted in MCs because of collisions, energy losses, ionization or their magnetic field, one would expect the same effect for electrons. In that case, the electron spectrum would be modified inside MCs and there would be an MBR component for Bremsstrahlung in molecular clouds. The CR electron spectrum inside MCs would have the same break (4 to 14 GV) and low energy index ($\alpha_1 = 1.0$) as the CR proton spectrum inside MCs because the depletion is caused by the same phenomenon in both cases, and the same high energy index ($\alpha = 3.21$) as the regular CR electron spectrum, because high energy electrons are not impacted by molecular clouds. Such a fit with now 6 templates was performed and showed no improvement in the region of interest. The reduced χ^2 skymap and the CMZ spectrum are provided in figure 4.11a and 4.11b respectively. The same eight pixels still have values higher than 7 as in figure 4.2b. In the CMZ, the break in the CR electron spectrum in MCs is located at 8 GV, just like the MCR break. Finally, the MBR flux skymap at E11 is provided in figure 4.11c. If the fit was significantly better with an MBR component than without it, it would be clear that the correlation with CO was a correlation with molecular clouds. Here, it is not possible to draw any conclusion.

However, some authors [44] independently calculated the spectrum of cosmic rays penetrating molecular clouds. According to their conclusions, in the CMZ, there should be a break in the CR proton spectrum at around 10 GV, resulting in a depletion of the gamma ray flux below 2 GeV, which is coherent with the results presented above (with MBR included or not). Figure 4.11d shows the proton spectra calculated in [44] and derived from the data in this thesis and a skymap of the MCR breaks can be found in appendix C.3. This result is a strong evidence in favor of the molecular cloud hypothesis.

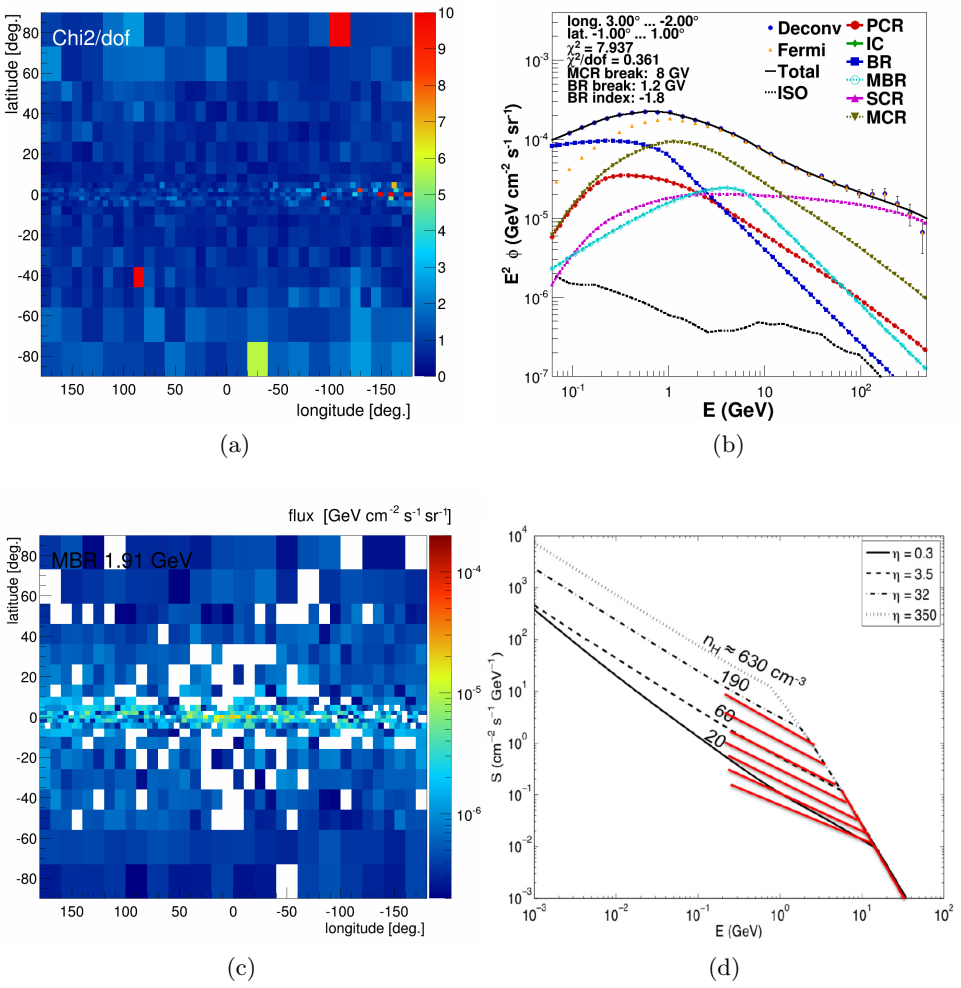

Figure 4.11: Reduced χ^2 skymap (a), CMZ spectrum (b) and MBR flux skymap at E11 (c) for a fit to deconvolved data with 6 templates. d) CR proton spectra in MCs calculated in [44] (black) and MCR spectra derived from the data in this work (red). Figure d) is taken from [19].

4.2.4 Old method

In previous work, non-convolved templates were fitted to convolved data. It was explained in part 3.3.4 that the right way of fitting is by fitting deconvolved data. However, if the fit is performed on both data set and in the same binning, one can notice that the fit provides as good results with convolved data with E0 included (see figure 4.12a) as with deconvolved data with E0 excluded. If E0 was included in fits to deconvolved data, the χ^2 values would drastically increase as this bin is known to be problematic for deconvolution. Nevertheless, not only the quality of the χ^2 skymap is important, but the morphology of the different components also. In binning J2, while fitting convolved data, a strange phenomenon arises: in the PCR skymaps, the pixels centered at 0° in latitude are less bright than the ones just above and just below. This smoothness problem does not show up with deconvolved data, neither in binning J2 nor in binning A. Figure 4.12b shows the PCR flux for the fit to data in binning J2. This result is not physical and demonstrates that unconvolved templates cannot fit correctly convolved data. The worse χ^2 hypothetically obtained with deconvolved data with E0 included is due to an underestimation of the errors on the corresponding data. In previous work, the error σ_i was always calculated as

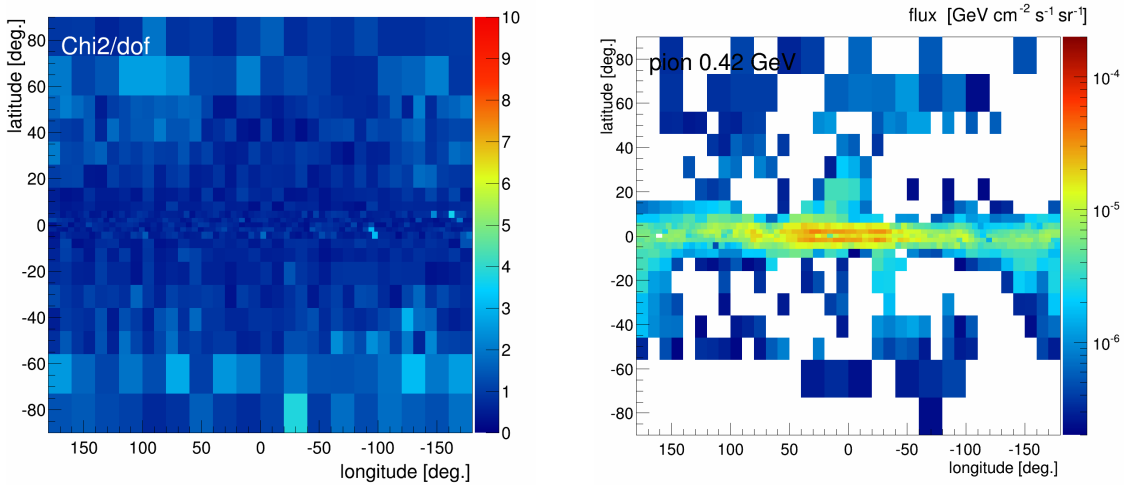

(a) (b)

Figure 4.12: Reduced χ^2 skymap and PCR flux skymap at E6 for a fit to convolved data in binning J2.

the quadratic sum of systematic and statistic errors (see part 3.2) and although the data are now deconvolved, no additional term was added because it is unknown. Removing E0 from the fit is the way of dealing with this lack of information. With larger error bars on deconvolved data, one could expect good χ^2 results with E0 included.

5 Conclusion

The Fermi GeV excess was given this name because the three standard gamma ray production processes, pion decay, inverse Compton scattering and Bremsstrahlung, including cosmic ray interactions, are not sufficient to reproduce the data at few GeV. After this announcement, some physicist looked for a sign of new physics in this excess, namely through dark matter. However, astrophysical explanations are able to reproduce the Fermi data, for example unresolved point sources like millisecond pulsars, not listed in the Fermi catalog, or molecular clouds. Millisecond pulsars as well as dark matter is expected to yield a spherical signal. In fact, analyses using spatial templates derived from astronomical information on the gas distribution and the interstellar radiation field, predict a spherical morphology for the excess. This morphology is only derived if spatial information is given to the fit. Alternatively, one can use a spectral template fit, using information derived from the measurements of cosmic ray spectra. If the signal is indeed spherical and not a residual of the used gas maps, both methods should yield the same result. This has not been found in previous studies. The signal morphology derived from spectral fits resembles the distribution of the molecular gas in our Galaxy, which suggests that the excess signal originates from molecular cloud complexes. Two additional templates were added in the spectral fits. First, the source template, which accounts for pion decay in the vicinity of point sources, leading to a harder spectrum. Then, the molecular clouds template, which also accounts for pion decay but inside molecular clouds, leading to a depletion of low energy gamma ray in the spectrum. With these now five templates, the spectral fit can reproduce the Fermi data with no need of new physics. However, the spectral fit has always neglected the telescope point spread function. In spatial fits, the templates can be convolved before the fit whereas spectral templates can not. Convolution is a process that involves the entire sky so it can not be applied in sky pixels separately. Spectral fits were therefore performed on data without getting rid of the point spread function effect. It was the goal of this thesis to study the impact of detector effects on the GeV excess in spectral fits.

In this work, the first deconvolution method of the Fermi data was implemented. With help from the Fermi software and matrix calculus, the point spread function effect can be removed from the data. The choice of the deconvolution binning, which is also the fit binning, is crucial and different binning were tested for robustness. The optimal binning found in this study was used to deconvolve the Fermi data and study the excess. It was found that the excess is still present after deconvolution and that its spatial morphology, as well as spectral shape are consistent with what was found before on convolved data. The five

templates were once again able to model the gamma ray emission and the correlation factor between the molecular clouds template and the molecular clouds distribution was found to be 0.89. Furthermore, an independent theoretical work studied the gamma ray emission inside molecular clouds from a theoretical point of view and found the same spectral shape as the one used in this work. The results of this work support the interpretation of the Fermi GeV excess as interactions between protons and molecular gas. An additional correlation, already present in previous work, was also found between the source template and the cosmic ray sources distribution.

Bibliography

[1] D. Pacini, "La radiazione penetrante alla superficie ed in seno alle acque," *Il Nuovo Cimento*, vol. 3, no. 1, pp. 93–100, Dec 1912.

[2] L. Goodenough and D. Hooper, "Possible Evidence For Dark Matter Annihilation In The Inner Milky Way From The Fermi Gamma Ray Space Telescope," *arXiv e-prints*, p. arXiv:0910.2998, Oct 2009.

[3] ESA, "Anatomy of the milky way," https://sci.esa.int/web/gaia/-/58206-anatomy-of-the-milky-way.

[4] J. F. Navarro *et al.*, "The Structure of Cold Dark Matter Halos," *The Astrophysical Journal*, vol. 462, p. 563, May 1996.

[5] F. Nesti and P. Salucci, "The Dark Matter halo of the Milky Way, AD 2013," *Journal of Cosmology and Astro-Particle Physics*, vol. 2013, no. 7, p. 016, Jul 2013.

[6] D. J. Bird *et al.*, "Detection of a Cosmic Ray with Measured Energy Well beyond the Expected Spectral Cutoff due to Cosmic Microwave Radiation," *The Astrophysical Journal*, vol. 441, p. 144, Mar 1995.

[7] R. Diehl *et al.*, "Radioactive ^{26}Al from massive stars in the Galaxy," *Nature*, vol. 439, no. 7072, pp. 45–47, Jan 2006.

[8] ESA, "Radioactive decay of aluminium-26," https://sci.esa.int/web/integral/-/48046-radioactive-decay-of-aluminium-26.

[9] A. W. S. *et al*, "Galprop version 54: Explanatory supplement," https://galprop.stanford.edu/download/manuals/galprop_v54.pdf.

[10] C. Evoli *et al.*, "Cosmic ray nuclei, antiprotons and gamma rays in the galaxy: a new diffusion model," *Journal of Cosmology and Astro-Particle Physics*, vol. 2008, no. 10, p. 018, Oct 2008.

[11] J. W. Cronin *et al.*, "Cosmic Rays at the Energy Frontier," *Scientific American*, vol. 276, no. 1, pp. 44–49, Jan 1997.

[12] P. Picozza *et al.*, "PAMELA A payload for antimatter matter exploration and light-nuclei astrophysics," *Astroparticle Physics*, vol. 27, no. 4, pp. 296–315, Apr 2007.

[13] R. J. Protheroe, "On the nature of the cosmic ray positron spectrum," *The Astrophysical Journal*, vol. 254, pp. 391–397, Mar 1982.

[14] M. Aguilar *et al.*, "First Result from the Alpha Magnetic Spectrometer on the International Space Station: Precision Measurement of the Positron Fraction in Primary Cosmic Rays of 0.5-350 GeV," *Physical Review Letter*, vol. 110, no. 14, p. 141102, Apr 2013.

[15] The Fermi-LAT collaboration, "Fermi Large Area Telescope Fourth Source Catalog," *arXiv e-prints*, p. arXiv:1902.10045, Feb 2019.

[16] K. Nakamura, "Review of Particle Physics," *Journal of Physics G Nuclear Physics*, vol. 37, no. 7A, p. 075021, Jul 2010.

[17] W. de Boer *et al.*, "Molecular clouds as origin of the fermi gamma-ray gev excess," *Physical Review D*, vol. 96, no. 4, Aug 2017. [Online]. Available: http://dx.doi.org/10.1103/PhysRevD.96.043012

[18] M. Aguilar *et al.*, "Electron and positron fluxes in primary cosmic rays measured with the alpha magnetic spectrometer on the international space station," *Phys. Rev. Lett.*, vol. 113, p. 121102, Sep 2014. [Online]. Available: https://link.aps.org/doi/10.1103/PhysRevLett.113.121102

[19] N. Petry, "The fermi gev-excess and its correlation with molecular clouds," 2017-2018.

[20] I. Gebauer, "An anisotropic model for galactic cosmic ray transport and its implications for indirect dark matter searches," Ph.D. dissertation, Karlsruher Institut für Technologie (KIT), 2010.

[21] W. B. Atwood *et al.*, "The Large Area Telescope on the Fermi Gamma-Ray Space Telescope Mission," *The Astrophysical Journal*, vol. 697, no. 2, pp. 1071–1102, Jun 2009.

[22] "Stanford's fermi lat site," http://www-glast.stanford.edu/instrument.html.

[23] M. Ackermann *et al.*, "Determination of the point-spread function for thefermilarge area telescope from on-orbit data and limits on pair halos of active galactic nuclei," *The Astrophysical Journal*, vol. 765, no. 1, p. 54, Feb 2013. [Online]. Available: http://dx.doi.org/10.1088/0004-637X/765/1/54

[24] F. Calore *et al.*, "RADIO DETECTION PROSPECTS FOR a BULGE POPULATION OF MILLISECOND PULSARS AS SUGGESTED BY FERMI-LAT OBSERVATIONS OF THE INNER GALAXY," *The Astrophysical Journal*, vol. 827, no. 2, p. 143, aug 2016. [Online]. Available: https://doi.org/10.3847%2F0004-637x%2F827%2F2%2F143

[25] M. Ajello *et al.*, "Fermi-LAT Observations of High-Energy Gamma-Ray Emission toward the Galactic Center," *The Astrophysical Journal*, vol. 819, no. 1, p. 44, Mar 2016.

[26] X. Huang *et al.*, "Galactic dark matter search via phenomenological astrophysics modeling," *Journal of Cosmology and Astro-Particle Physics*, vol. 2016, no. 4, p. 030, Apr 2016.

[27] R. Bartels *et al.*, "Strong support for the millisecond pulsar origin of the galactic center gev excess," *Phys. Rev. Lett.*, vol. 116, p. 051102, Feb 2016. [Online]. Available: https://link.aps.org/doi/10.1103/PhysRevLett.116.051102

[28] The Fermi-LAT collaboration, "Fermi lat data," https://heasarc.gsfc.nasa.gov/FTP/fermi/data/lat/.

[29] The Fermi-LAT collaboration, "Fermi tools," https://github.com/fermi-lat/Fermitools-conda/wiki/Installation-Instructions.

[30] M. Ackermann *et al.*, "Search for gamma-ray spectral lines with the Fermi Large Area Telescope and dark matter implications," *Physical Review D*, vol. 88, no. 8, p. 082002, Oct 2013.

[31] S. A. OBSERVATORY, "Saoimageds9," http://ds9.si.edu/.

[32] The Fermi-LAT collaboration, "Lat background models," https://fermi.gsfc.nasa.gov/ssc/data/access/lat/BackgroundModels.html.

[33] F. James, "Minuit package," https://root.cern.ch/doc/master/classTMinuit.html.

[34] P. L. Biermann *et al.*, "The origin of cosmic rays: Explosions of massive stars with magnetic winds and their supernova mechanism," *The Astrophysical Journal*, vol. 725, no. 1, p. 184–187, Nov 2010. [Online]. Available: http://dx.doi.org/10.1088/0004-637X/725/1/184

[35] D. Gaggero *et al.*, "Gamma-ray sky points to radial gradients in cosmic-ray transport," *Physical Review D*, vol. 91, no. 8, Apr 2015. [Online]. Available: http://dx.doi.org/10.1103/PhysRevD.91.083012

[36] F. Acero *et al.*, "Development of the model of galactic interstellar emission for standard point-source analysis of fermi large area telescope data," *The Astrophysical Journal Supplement Series*, vol. 223, no. 2, p. 26, Apr 2016. [Online]. Available: http://dx.doi.org/10.3847/0067-0049/223/2/26

[37] R. Carlberg and R. Pudritz, "Magnetic support and fragmentation of molecular clouds," *Monthly Notices of the Royal Astronomical Society*, vol. 247, p. 353, 11 1990.

[38] J. Alcaraz *et al.*, "Protons in near earth orbit," *Physics Letters B*, vol. 472, no. 1, pp. 215 – 226, 2000. [Online]. Available: http://www.sciencedirect.com/science/article/pii/S0370269399014276

[39] W. de Boer *et al.*, "An alternative Explanation for the Fermi GeV Gamma-Ray Excess," *arXiv e-prints*, p. arXiv:1610.08926, Oct 2016.

[40] "Numpy," https://numpy.org/.

[41] The Fermi-LAT collaboration, "Galactic interstellar emission model for the 4fgl catalog analysis," https://fermi.gsfc.nasa.gov/ssc/data/analysis/software/aux/4fgl/Galactic_Diffuse_Emission_Model_for_the_4FGL_Catalog_Analysis.pdf.

[42] P. Collaboration, "2015 cmb and astrophysical component maps," https://wiki.cosmos.esa.int/planckpla2015/index.php/CMB_and_astrophysical_component_maps#CO_line_emission.

[43] L. Bouchet *et al.*, "The galactic26al emission map as revealed byintegralspi," *The Astrophysical Journal*, vol. 801, no. 2, p. 142, Mar 2015. [Online]. Available: http://dx.doi.org/10.1088/0004-637X/801/2/142

[44] V. A. Dogiel *et al.*, "Gamma-ray emission from molecular clouds generated by penetrating cosmic rays," *The Astrophysical Journal*, vol. 868, no. 2, p. 114, Nov 2018. [Online]. Available: http://dx.doi.org/10.3847/1538-4357/aae827

Appendix

A Abbreviations

AMS	Alpha Magnetic Spectrometer
AGN	Active Galactic Nucleus
BR	Bremsstrahlung
CMB	Cosmic Microwave Background
CMZ	Central Molecular Zone
CR	Cosmic Ray
DM	Dark Matter
EAS	Extensive Air Shower
GCE	Galactic Center Excess
GRB	Gamma Ray Burst
IC	Inverse Compton
ISM	Interstellar Medium
ISRF	Insterstellar radiation field
LAT	Large Area Telescope
MC	Molecular Cloud
MCR	Molecular clouds Cosmic Ray proton
MBR	Molecular Clouds Bremsstrahlung
MSP	Millisecond Pulsars
NFW	Navarro-Frenk-White
PCR	Proton Cosmic Ray
PSF	Point Spread Function
SCR	Source cosmic ray
SNR	Supernova Remnant
WIMP	Weakly Interractive Massive Particle

B Method

B.1 Data energy

Name	E_{min} (GeV)	E_{max} (GeV)	E_{mean} (GeV)	counts (10^6)
E0	0.0590	0.0798	0.0686	15.9
E1	0.0798	0.1080	0.0929	18.0
E2	0.1080	0.1461	0.1256	21.0
E3	0.1461	0.1977	0.1700	22.4
E4	0.1977	0.2675	0.2300	21.5
E5	0.2675	0.3620	0.3112	19.3
E6	0.3620	0.4898	0.4211	16.6
E7	0.4898	0.6627	0.5697	13.6
E8	0.6627	0.8967	0.7708	10.6
E9	0.8967	1.2132	1.0430	8.01
E10	1.2132	1.6415	1.4112	5.69
E11	1.6415	2.2210	1.9094	3.84
E12	2.2210	3.0051	2.5835	2.55
E13	3.0051	4.0661	3.4956	1.64
E14	4.0661	5.5015	4.7297	1.02
E15	5.5015	7.4438	6.3994	0.630
E16	7.4438	10.071	8.6586	0.390
E17	10.071	13.627	11.715	0.241
E18	13.627	18.438	15.851	0.151
E19	18.438	24.948	21.447	0.0957
E20	24.948	33.755	29.019	0.0631
E21	33.755	45.672	39.264	0.0411
E22	45.672	61.795	53.125	0.0256
E23	61.795	83.611	71.880	0.0159
E24	83.611	113.129	97.257	0.00985
E25	113.129	153.067	131.591	0.00625
E26	153.067	207.105	178.048	0.00380
E27	207.105	280.220	240.905	0.0240
E28	280.220	379.148	325.952	0.0148
E29	379.148	513.000	441.025	0.000926

Table B.1: Characteristics of the energy bins. Counts are diffuse counts and $E_{mean} = \sqrt{E_{min} \cdot E_{max}}$.

B.2 Binning A

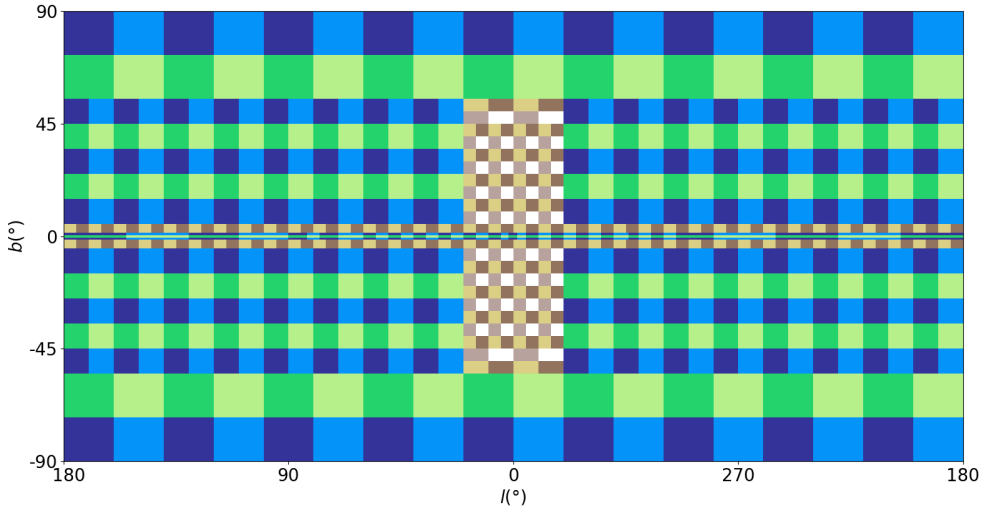

Figure B.1: Overview of binning A and its 797 pixels.

B.3 Convolution and deconvolution matrices

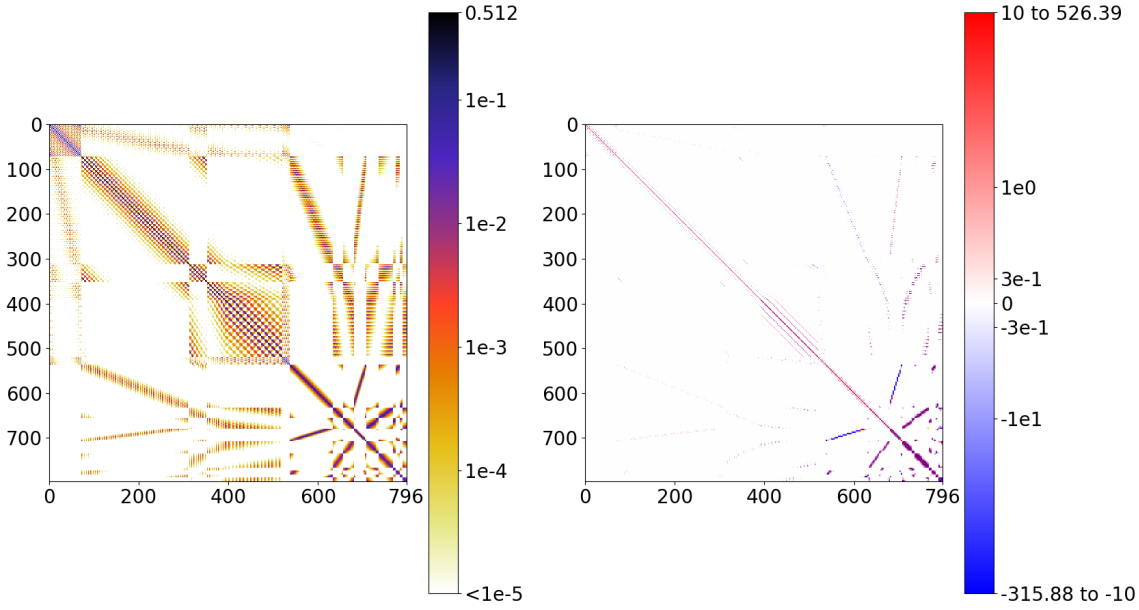

Figure B.2: Convolution (left) and deconvolution (right) matrices for binning A at E0. The x and y axises are pixel numbers. The z scale is logarithmic for both matrices except between the two numbers around zero where the scale is linear for the deconvolution matrix.

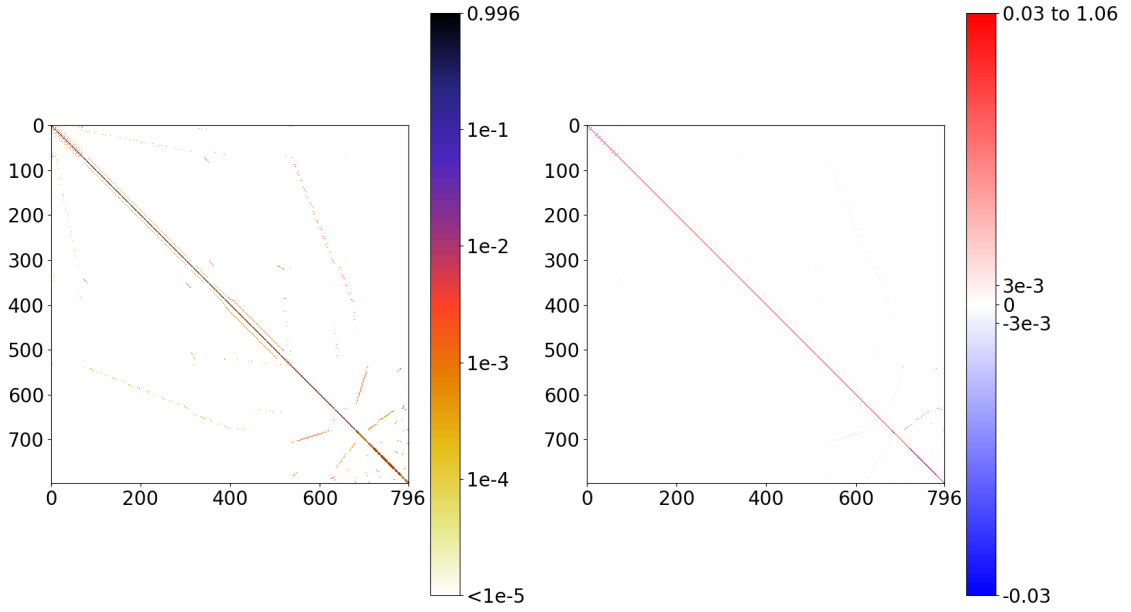

Figure B.3: Convolution (left) and deconvolution (right) matrices for binning A at E29. The x and y axises are pixel numbers. The z scale is logarithmic for both matrices except between the two numbers around zero where the scale is linear for the deconvolution matrix.

B.4 Binning J2

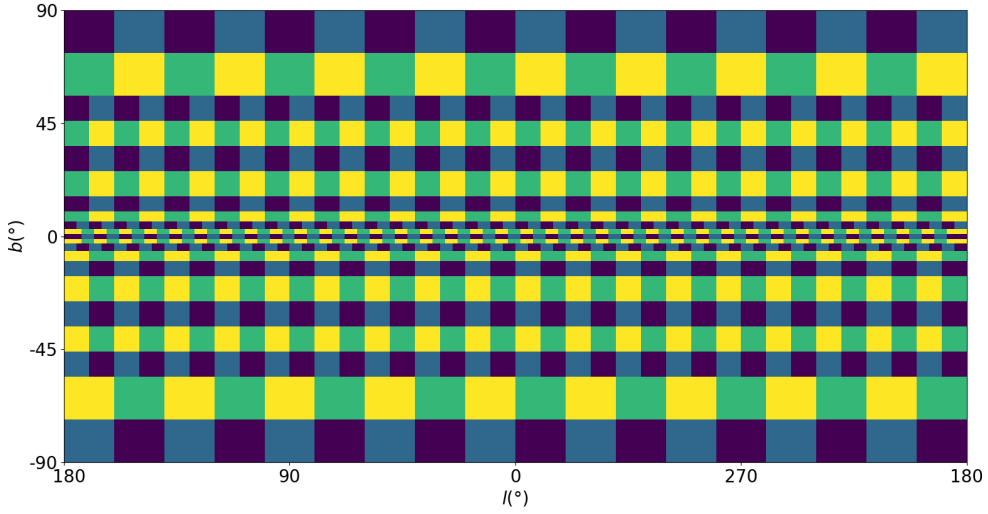

Figure B.4: Overview of binning J2 and its 861 pixels.

B.5 Fermi software convolution vs matrix convolution

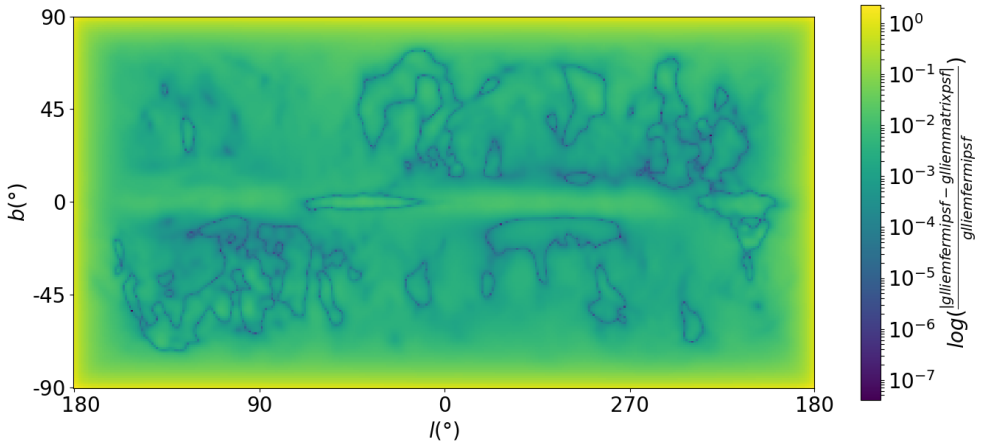

Figure B.5: Relative error between the Fermi software convolution and the $1° \times 1°$ matrix convolution for E1.

B.6 Fermi software convolution border effect

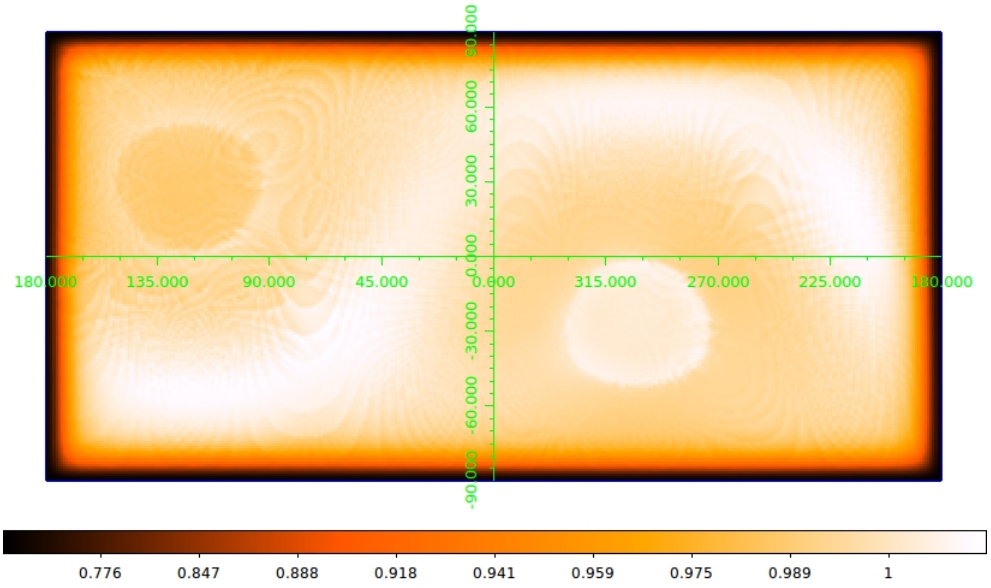

Figure B.6: Ratio between the isotropic background with PSF applied (with the Fermi software) and with no PSF applied at E11. The x axis is longitude and the y axis is latitude. The faint per-mille-level structures visible in the plane and in the halo are residuals of the Fermi detector's exposure: The convolution was applied to an isotropic flux which does not look like an isotropic count map to the detector. In order to provide the Fermi-software with the counts corresponding to an isotropic flux, this isotropic flux had to be multiplied by the detector's exposure. The comparison of the map convolved with the Fermi software and the original map then yields a "faint shadow" of the exposure map on the per-mille-level.

B.7 Flux and deconvolved flux

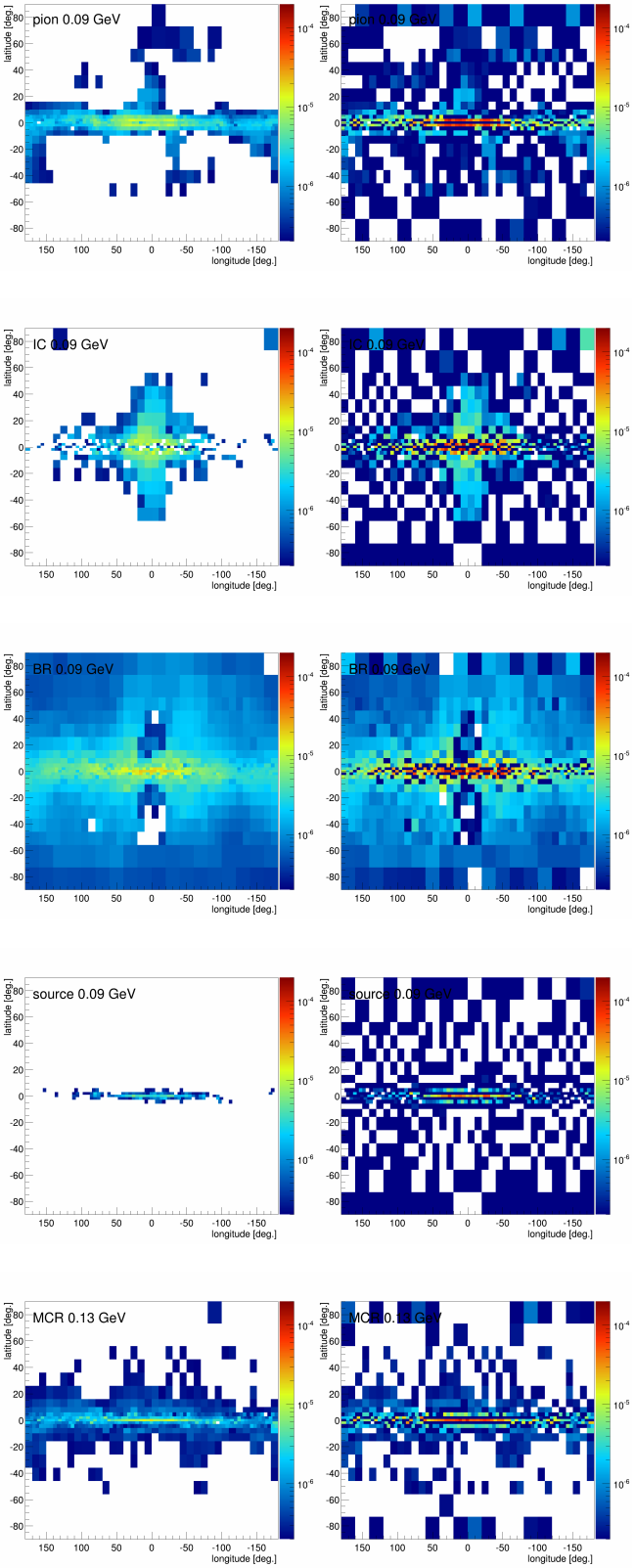

Figure B.7: Flux skymaps for a fit to convolved Fermi data (left) and corresponding forward deconvolved skymaps (right) in binning J2.

B.8 Total forward deconvolved spectrum

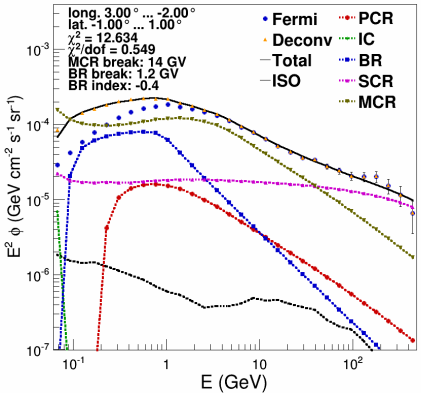

Figure B.8: Forward deconvolved CMZ spectrum for a fit to data in binning J2. In the fit, E0 is included, but in the χ^2 calculation that compares the deconvolved data and the deconvolved model, it is not.

B.9 χ^2 skymaps of models A' and B'

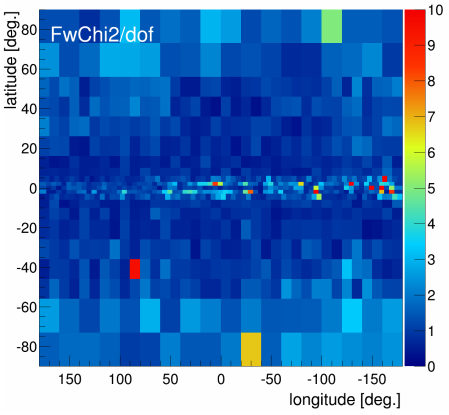

Figure B.9: Reduced χ^2 skymap for model A' which is the forward deconvolution of model A that describes the data. For more details on the models, see figure 3.22

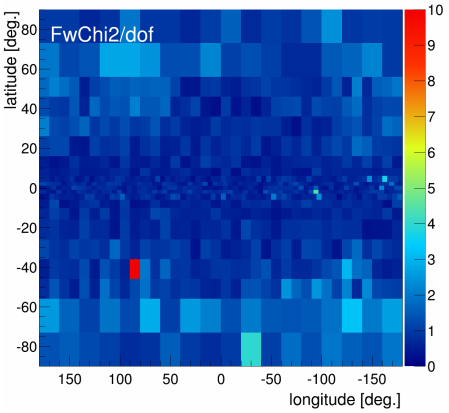

Figure B.10: Reduced χ^2 skymap for model B' which is the forward convolution of model B that describes the deconvolved data. For more details on the models, see figure 3.22

C Results

C.1 Scatterplots

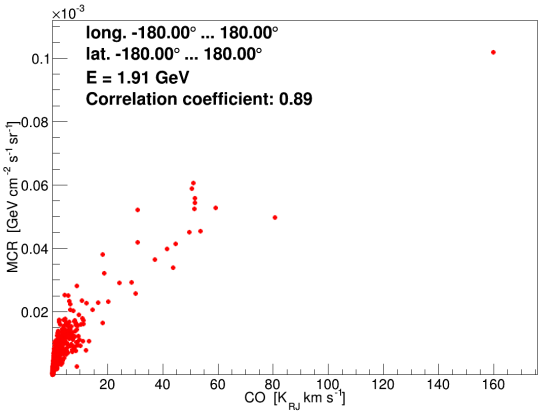

Figure C.1: Scatterplot of CO flux versus MCR flux. Templates were fitted to deconvolved data in binning J2.

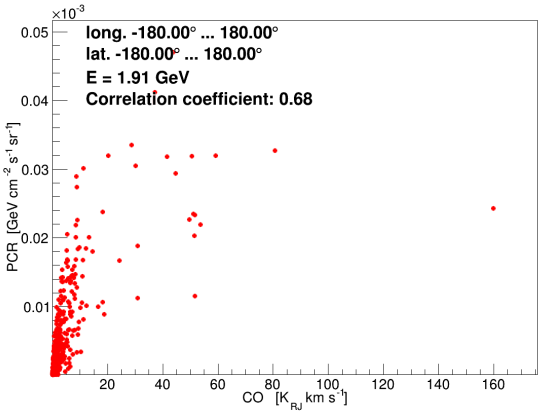

Figure C.2: Scatterplot of CO flux versus PCR flux. Templates were fitted to deconvolved data in binning J2.

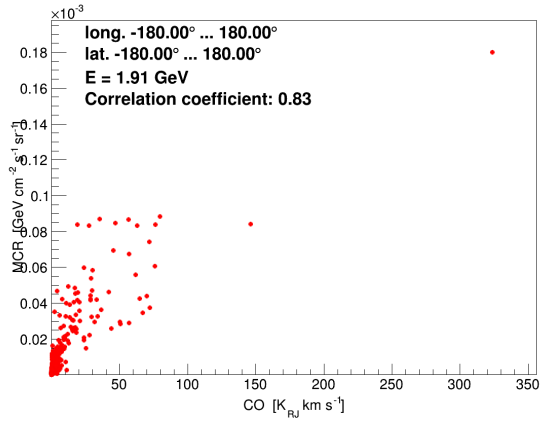

Figure C.3: Scatterplot of CO flux versus MCR flux. Templates were fitted to Fermi data in binning A.

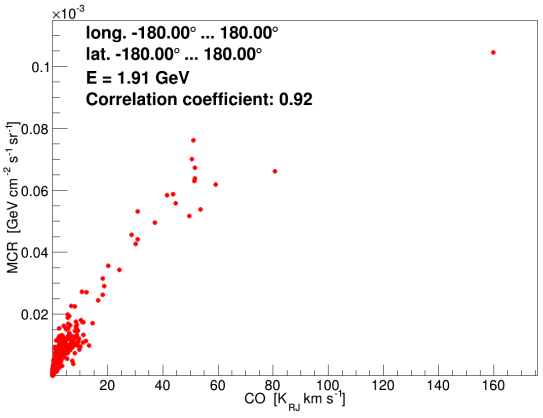

Figure C.4: Scatterplot of CO flux versus MCR flux. Templates were fitted to Fermi data in binning J2.

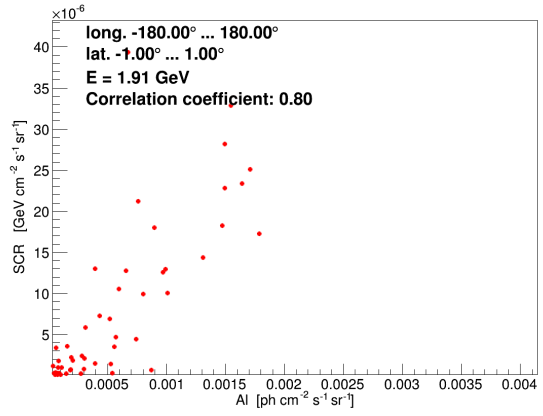

Figure C.5: Scatterplot of ^{26}Al flux versus SCR flux in the galactic plane. Templates were fitted to deconvolved data in binning J2.

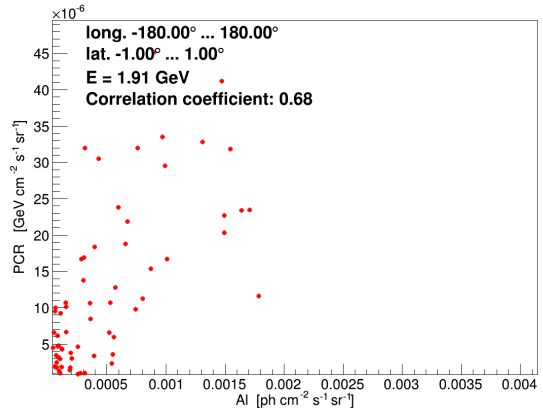

Figure C.6: Scatterplot of ^{26}Al flux versus PCR flux in the galactic plane. Templates were fitted to deconvolved data in binning J2.

C.2 Spectra with error bars

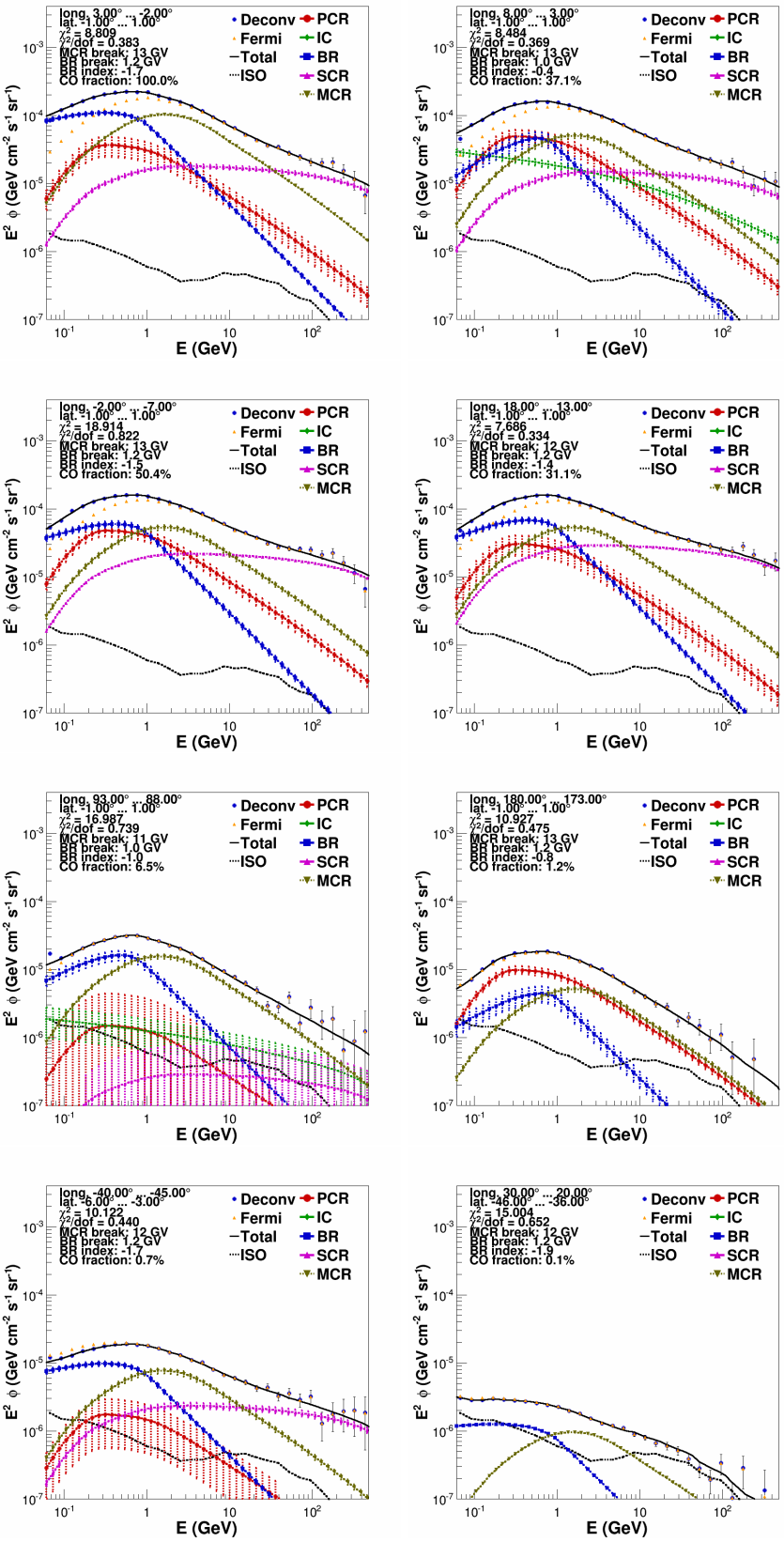

Figure C.7: Spectra including error bars calculated in the Minuit minimization.

C.3 MCR break skymap

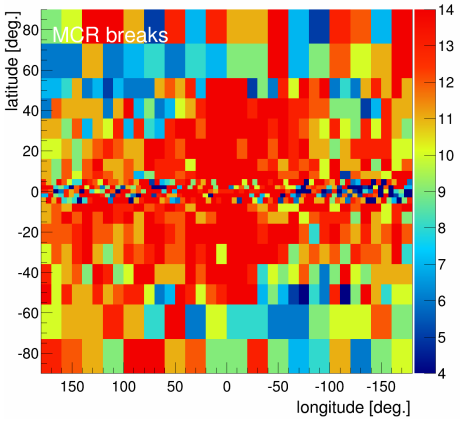

Figure C.8: MCR break skymap for a fit to deconvolved data.